Chapter 3: X-ray Radiography and Computer Tomography

X-ray Physics

X-ray Physics

How does an X-ray tube produce X-ray?

X-ray Generation – X-ray Tube

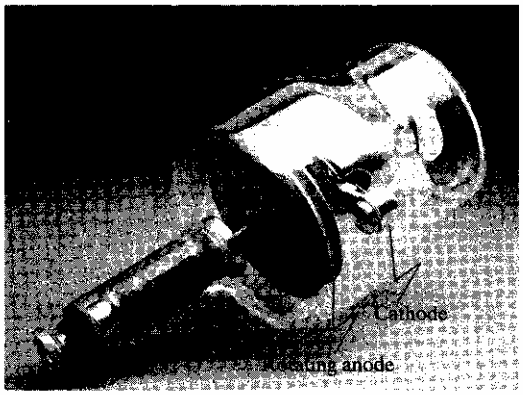

Figure 5.3
An x-ray tube.

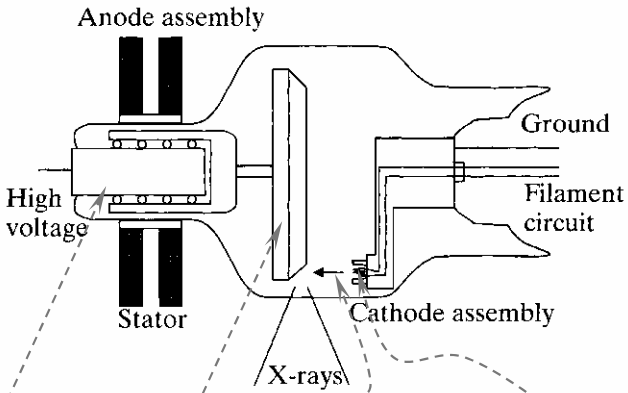

Figure 5.4
Schematic diagram of an x-ray tube.

Motor, Why?

Rotating target

Filament

Electron beam? How are electrons generated?

X-ray Generation – Bremmstrahlung

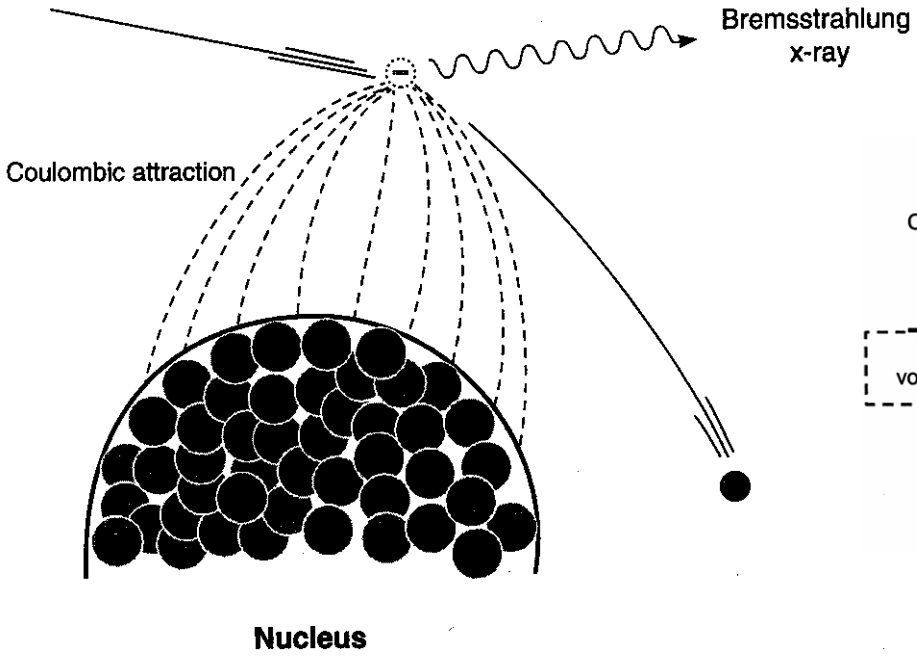

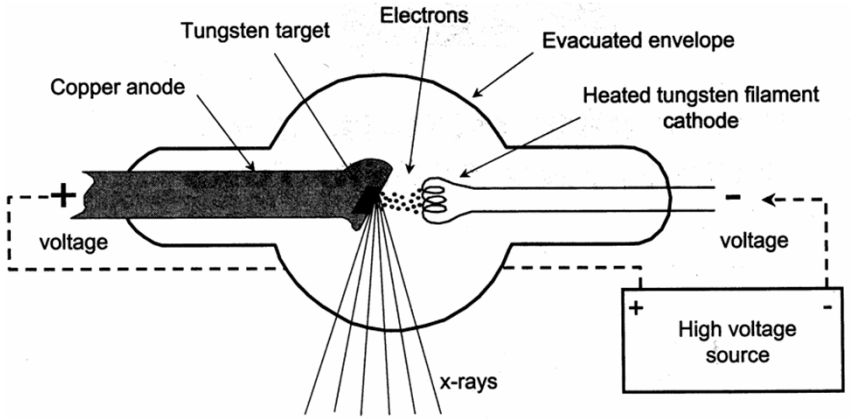

- X-rays are produced by the conversion of e^- KE into EM radiation - **Bremsstrahlung** (G: "braking radiation").
- A large potential difference is applied across the two electrodes in an evacuated envelope
- Neg. charged electrode (***cathode***): source of e^-
- Pos. charged electrode (***anode***): target of e^-

X-ray Generation – Characteristic X-rays

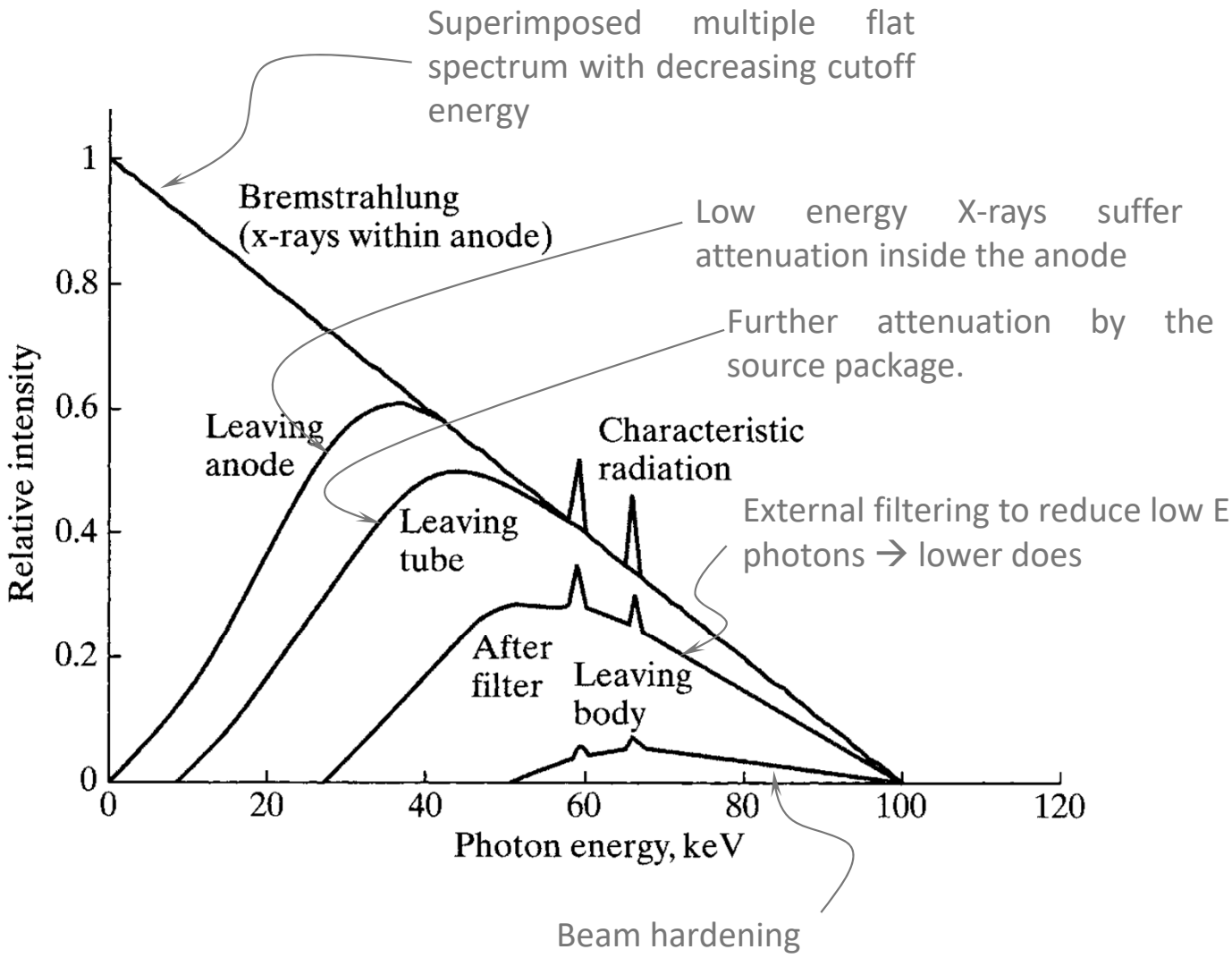

Figure 5.5
Relative intensity of x-ray photons. (Adapted from Webster, 1998. This material is used by permission of John Wiley & Sons, Inc.)

Compton Scattering

- ***Dominant interaction*** of x-rays with ***low-Z materials*** in the diagnostic range and beyond (approx. 30 keV - 30MeV)
- Occurs ***between the photon and a outer shell e^-***, which is considered free when E_g >> binding energy, E_b of the e^-.
- Encounter results in ***ionization of the atom*** and probabilistic distribution of the incident photon E to that of the scattered photon and the ejected e^-
- A probabilistic distribution determines the scattering angle.

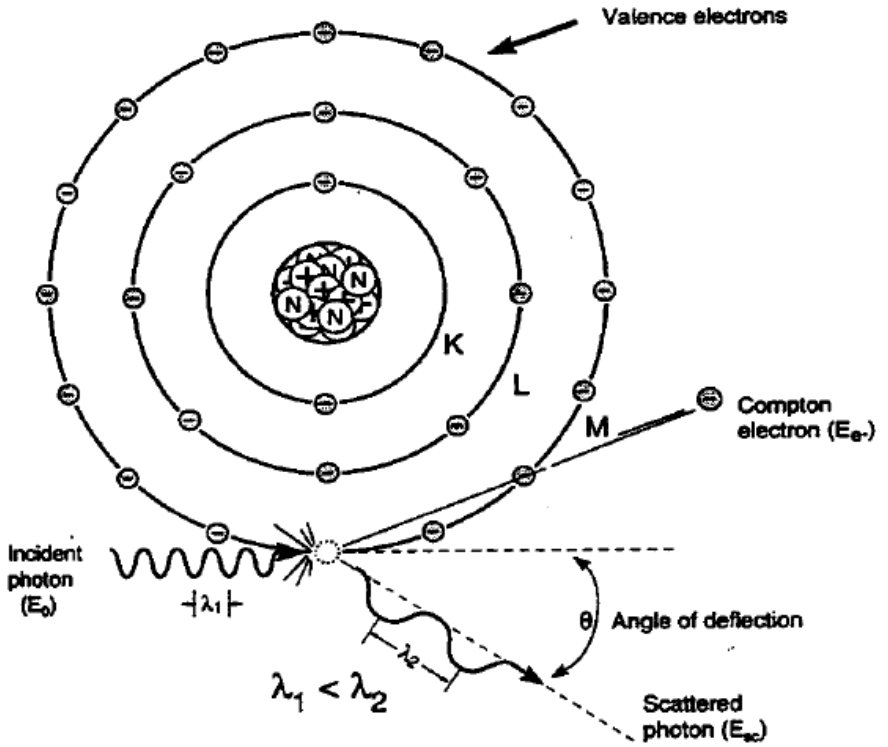

Compton Scattering

- Compton interaction probability is dependent on ***the total no. of e^- in the absorber vol.*** ($e^-/cm^3 = e^-/gm \cdot$ density) or ***electron density***
- With the exception of ^1H, e^-/gm is fairly constant for organic materials ($Z/A \cong 0.5$), thus the probability of ***Compton interaction proportional to material density (ρ)***
- ***Conservation of energy and momentum*** yield the following equations:

$$E_{hv'} = \frac{E_{hv}}{1 + \frac{E_{hv}}{m_e c^2}(1 - \cos\theta)},$$

where

$m_e c^2 = 511\text{keV}$

E_{hv} : energy of the incident photon

$E_{hv'}$: energy of the scattered photon

Photoelectric Effect

- Interaction of incident photon with ***inner shell e***$^-$, why?
- All E transferred to e^- (ejected ***photoelectron***) as kinetic energy (E_e) less the binding energy: $E_e = E_0 - E_b$
- ***Empty shell immediately filled with e***$^-$ ***from outer orbits*** resulting in the emission of characteristic x-rays (E_γ = differences in E_b of orbitals), for example, Iodine: E_K = 34 keV, E_L = 5 keV, E_M = 0.6 keV

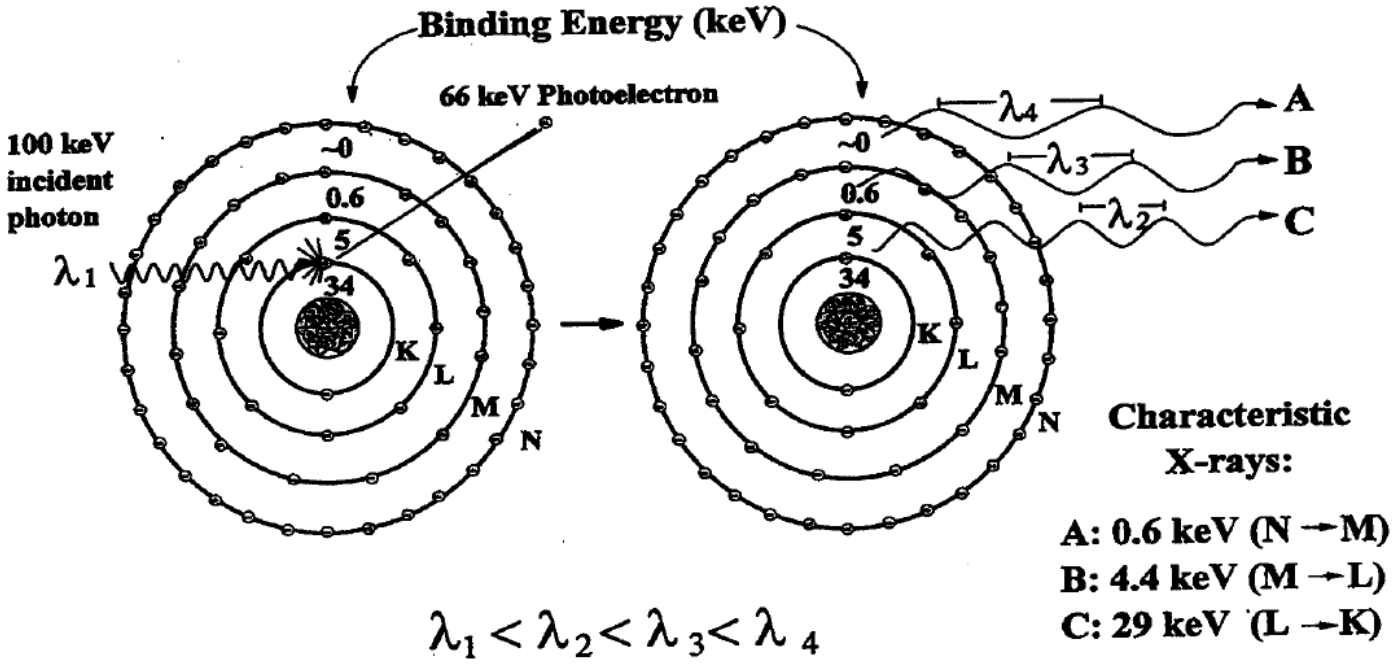

X-ray Interactions and Associated Phenomena

- Beam hardening,
- contrast agents and
- filtration of X-ray tubes

Photoelectric Effect

- Photoe$^-$ absorption is the preferred interaction for X-ray imging.
- Rem.: $E_b \propto Z^2$; characteristic x-rays and/or Auger e$^-$ → ***preferred in high Z material***.
- Probability of photoe$^-$ absorption $\propto Z^3/E^3$ (Z = atomic no.) → ***provide contrast according to different Z***.
- Due to the absorption of the incident x-ray without scatter, maximum subject contrast arises with a photoe$^-$ effect interaction → ***No scattering contamination*** → better contrast
- Explains why contrast ↓ as higher energy x-rays are used in the imaging process
- Increased probability of photoe$^-$ absorption just above the E_b of the inner shells cause discontinuities in the ***attenuation profiles*** (e.g., K-edge)

Photoelectric Effect

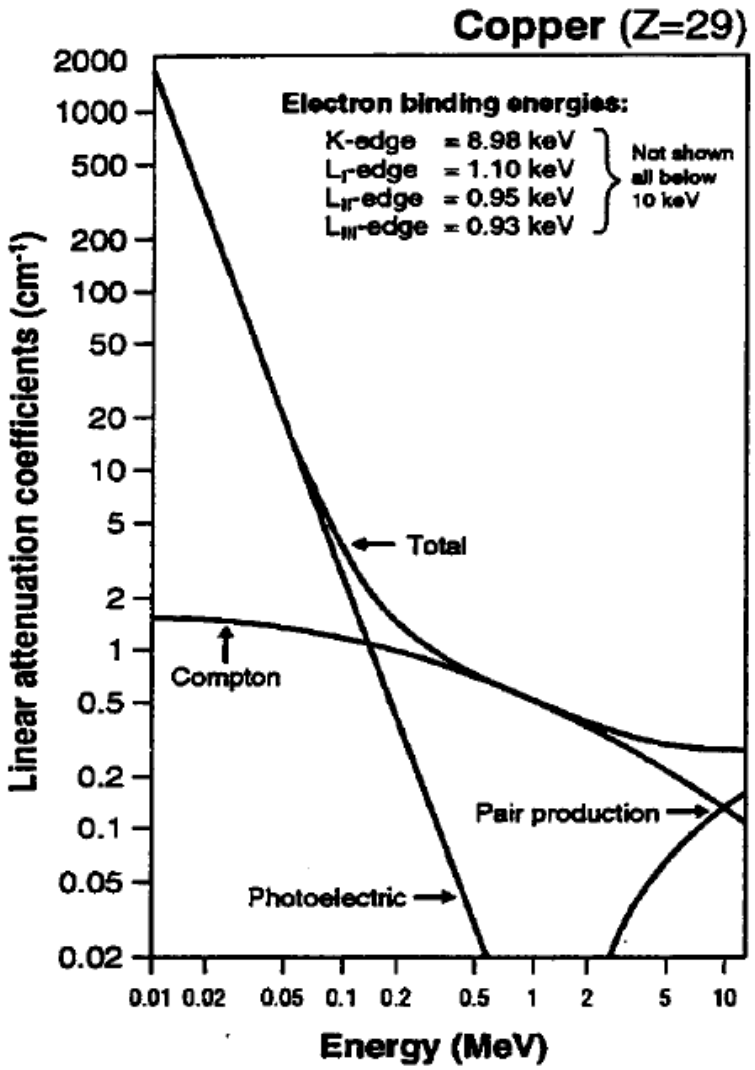

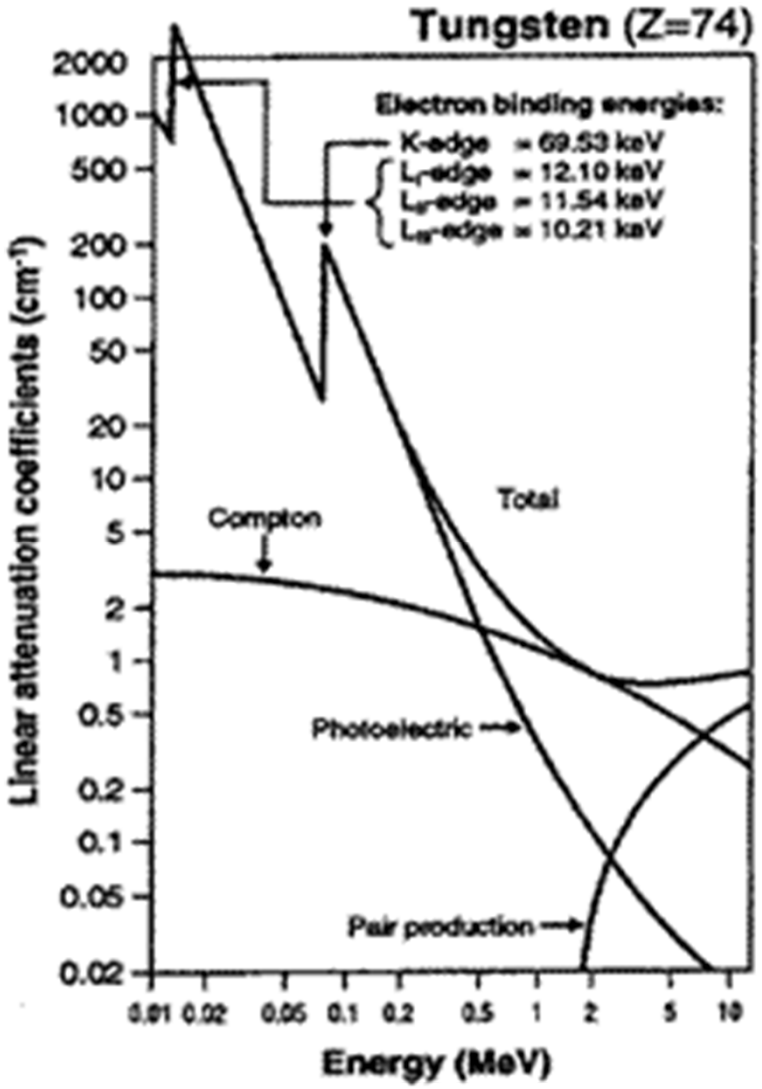

Attenuation Mechanism

- Attenuation mechanisms as a function of energy

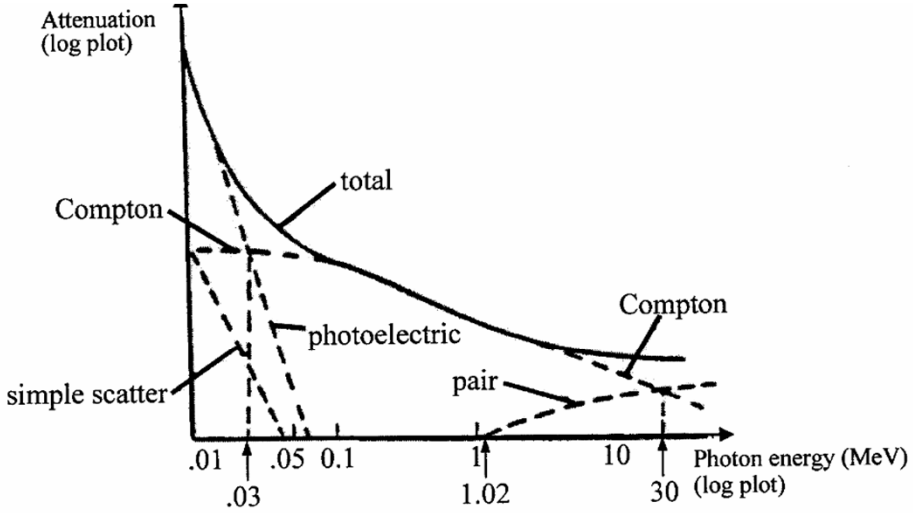

Attenuation mechanisms in water

The optimum photon energy is about 30 keV (tube voltage 80-100 kV) where the photoelectric effect dominates. The Z^3 dependence leads to good contrast:

Z_{fat}	5.9
$Z_{muscles}$	7.4
Z_{bone}	13.9

$\Rightarrow$ Photoelectric attenuation from bone is about 11x that due to soft tissue, which is dominated by Compton scattering.

Attenuation Mechanism

- Attenuation mechanisms as a function of energy

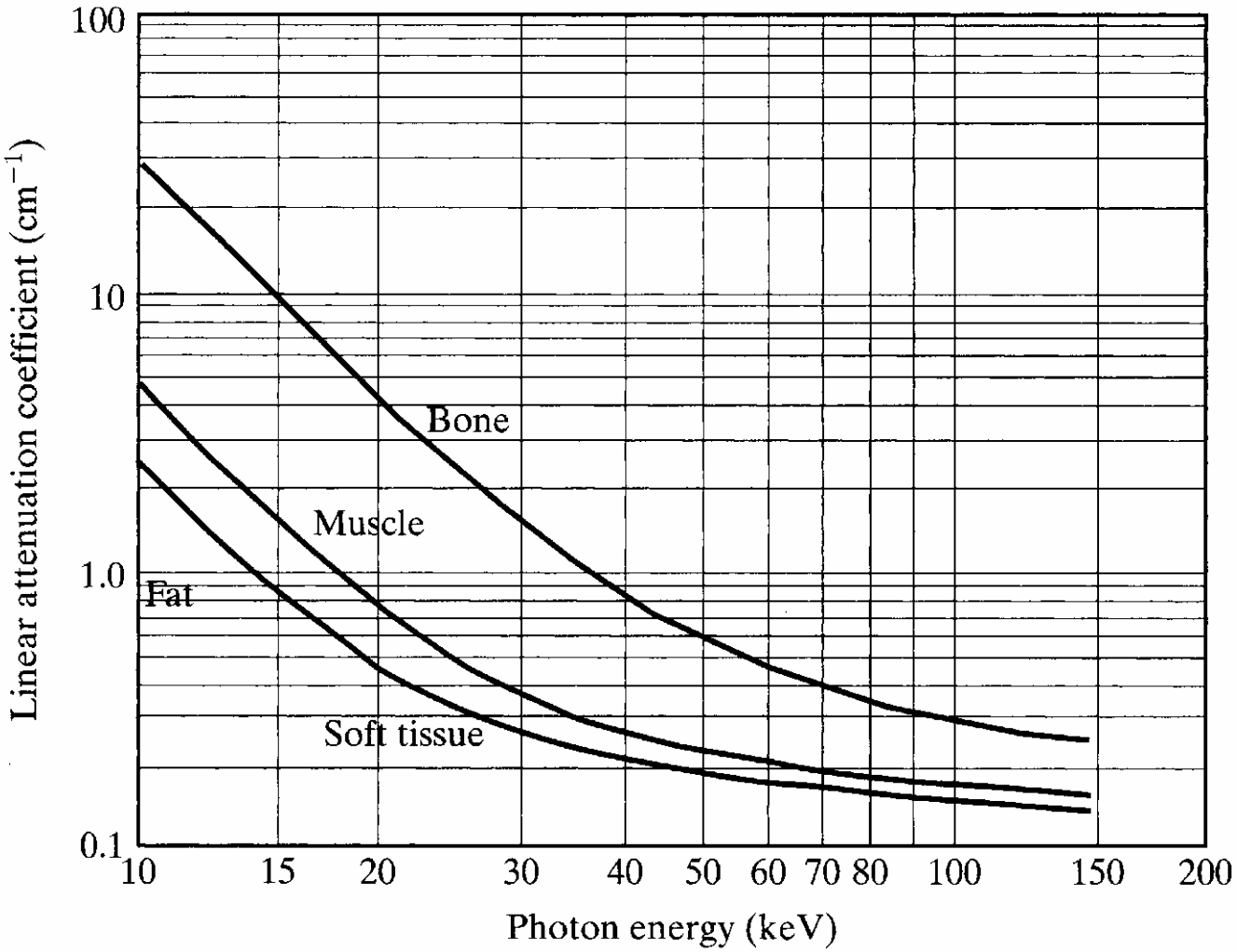

Figure 4.8
Linear attenuation coefficient for bone, muscle, and fat as a function of incident x-ray photon energy.

Photoelectric Effect

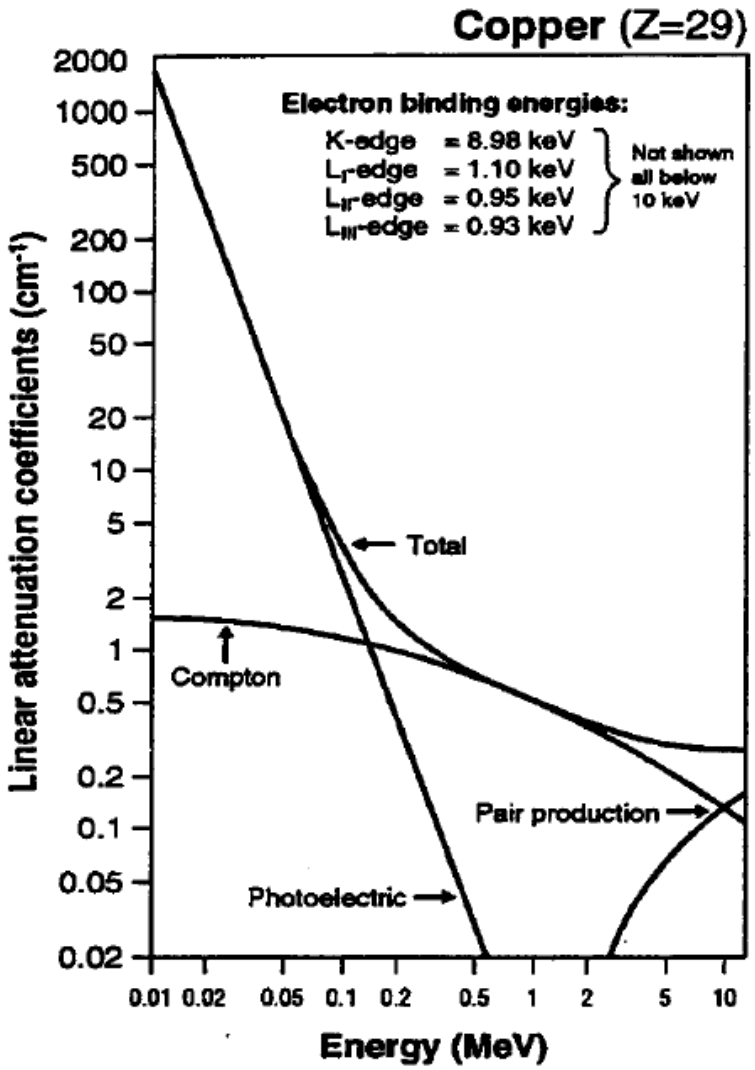

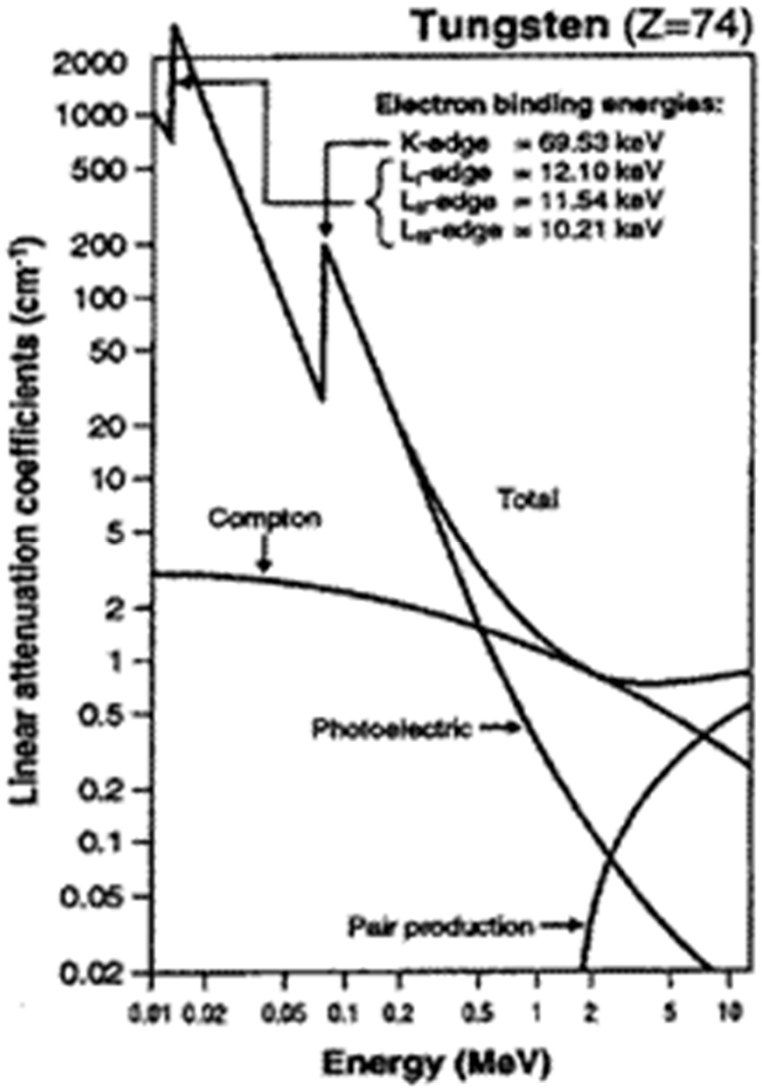

Beam Hardening Effect, Contrast Agents, and X-ray Filtration

X-ray Generation – Filtration

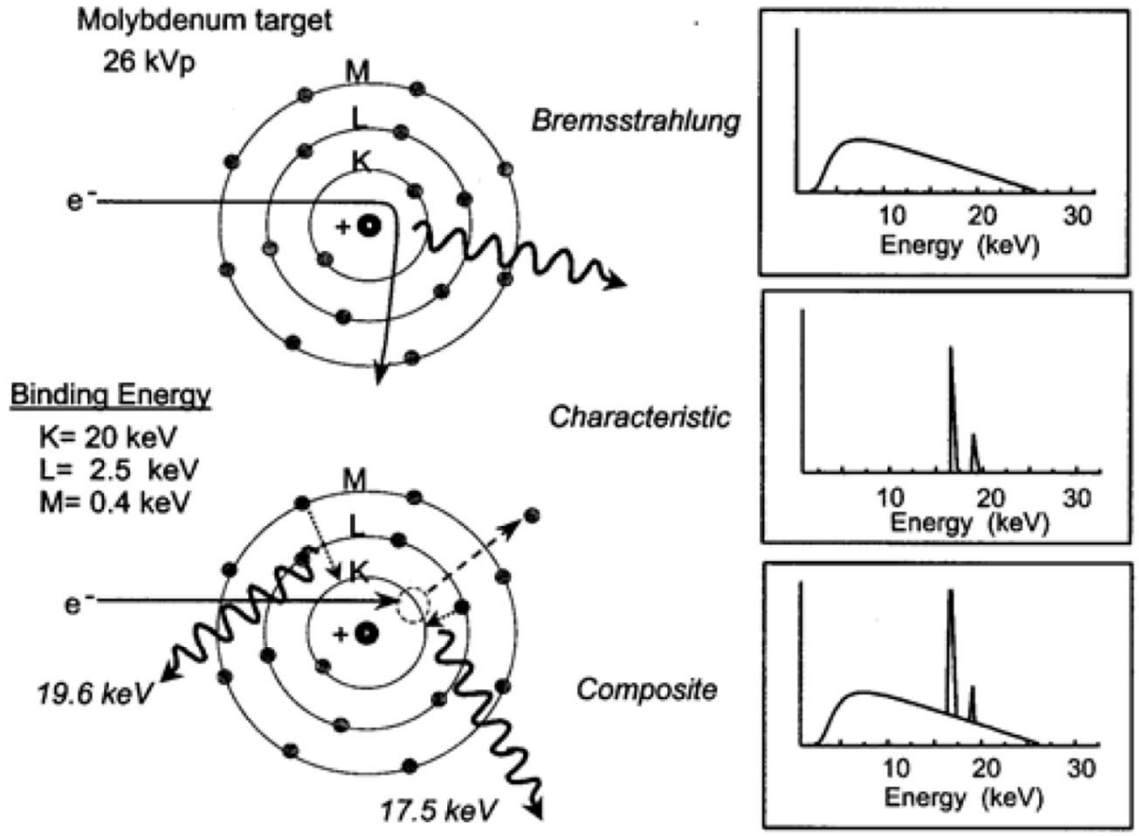

FIGURE 8-7. The output of a mammography x-ray system is composed of bremsstrahlung and characteristic radiation. The characteristic radiation energies of molybdenum (17.5 and 19.6 keV) are nearly optimal for detection of low-contrast lesions in breasts of 3- to 6-cm thickness.

Options:

Molybdenum (Mo)

Ruthenium (Ru)

Rhodium (Rh)

Palladium (Pd)

Silver (Ag)

Cadmium (Cd)

X-ray Generation – Filtration

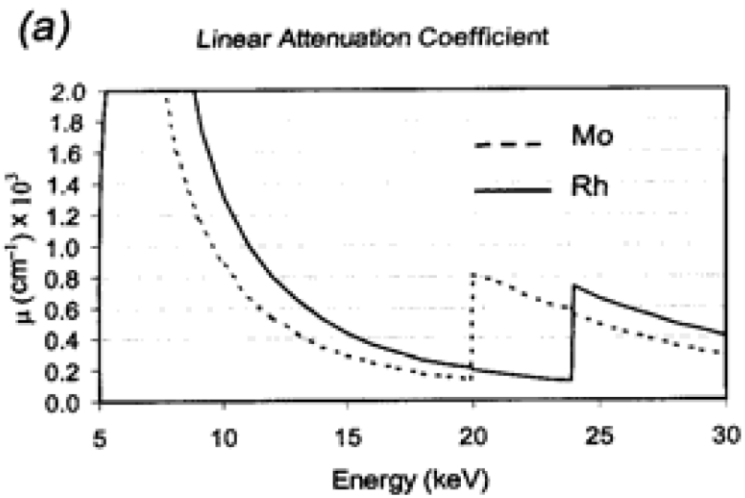

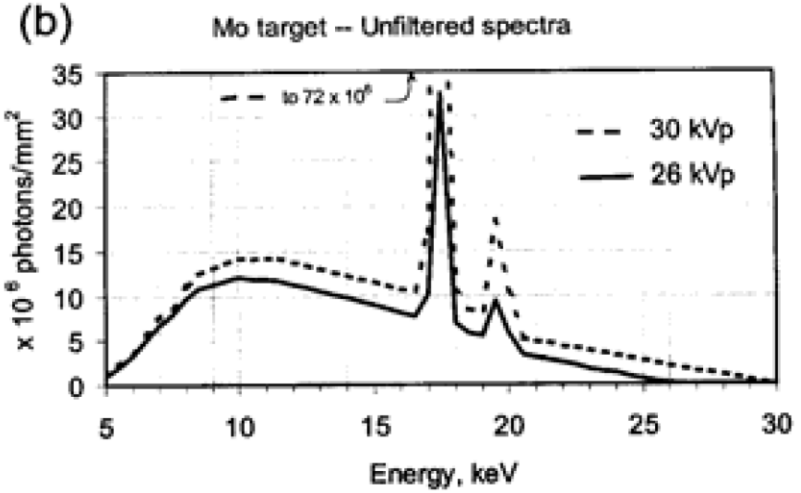

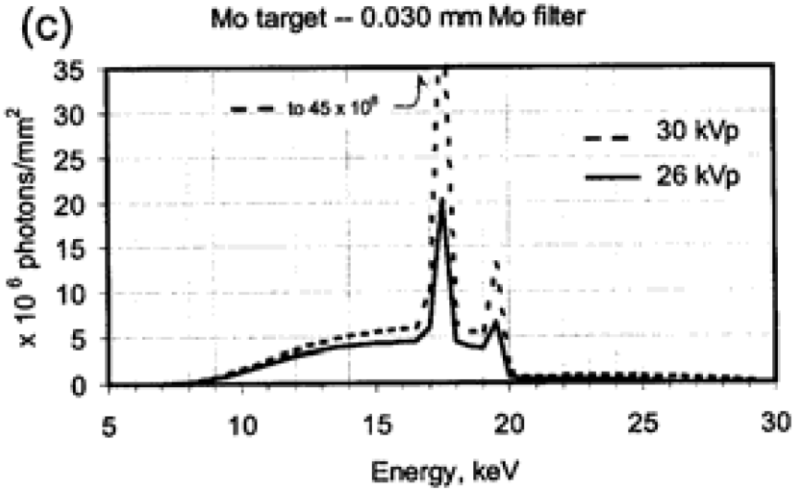

FIGURE 8-8. (a) The attenuation coefficients of Mo and Rh are plotted as a function of energy. A low-attenuation "window" exists just below the *K*-edge energy. **(b)** *Unfiltered* spectra from a molybdenum target are shown for 26- and 30-kVp tube voltages. These spectra contain a relatively large fraction of low- and high-energy photons. **(c)** The filtered spectra from a molybdenum target at 26 and 30 kVp after transmission through a 30 μm Mo filter. The filter eliminates a majority of the low- and high-energy x-rays.

X-ray Generation – Filtration

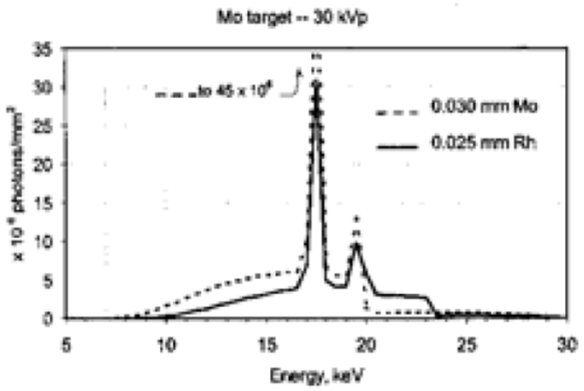

FIGURE 8-9. Output spectra from a Mo target for a 30-kVp tube voltage with a 0.030-mm Mo filter and 0.025-mm Rh filter show the relative bremsstrahlung photon transmission "windows" just below their respective *K*-edges.

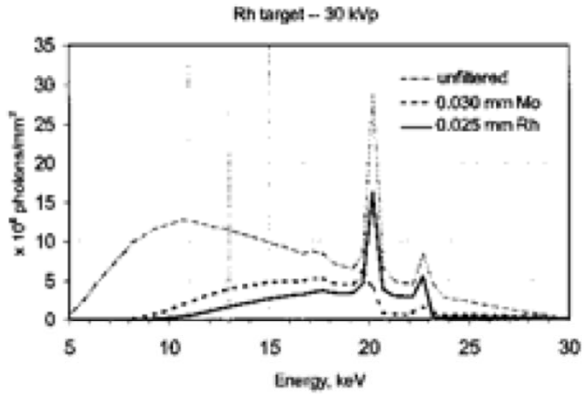

FIGURE 8-10. The rhodium target provides characteristic x-ray energies 2 to 3 keV higher than the corresponding Mo target. The unfiltered spectrum (*light dashed line*) is modified by 0.030-mm Mo (*heavy dashed line*) and 0.025-mm Rh (*solid line*) filters. A Mo filter with an Rh target inappropriately attenuates Rh characteristic x-rays.

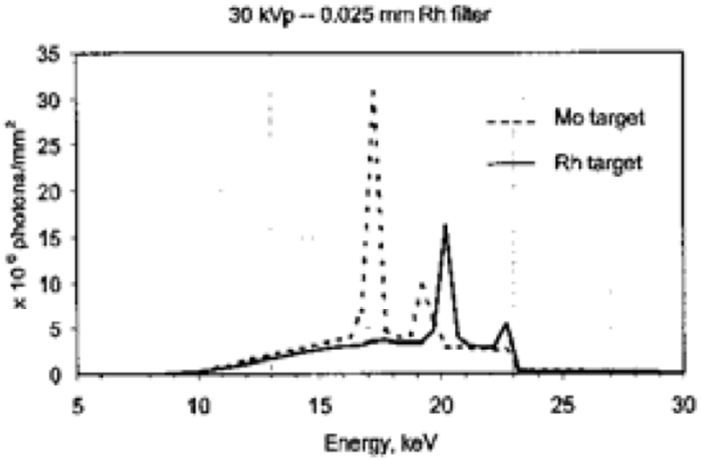

FIGURE 8-11. Spectra from beams filtered by 0.025 mm Rh are depicted for a Mo and an Rh target. The major difference is the higher energies of the characteristic x-rays generated by the Rh target, compared to the Mo target.

- filtering reduces the x-ray energy photons below the K-shell edge providing a transmission window for characteristic x-rays.

typical values – Mo target with 0.03 mm Mo filter (Mo/Mo)
- Rh target with 0.025 mm Rh filter (Rh/Rh)
- Mo target with Rh filter
- note: cannot use Rh target with Mo filter!

Ref: Bushberg

Photoelectric Effect and Absorption Edge

- Edges become significant factors for higher Z materials as the E_b are in the diagnostic energy range:
- **Contrast agents** – barium (Ba, Z=56) and iodine (I, Z=53)
- Rare earth materials used for intensifying screens – lanthanum (La, Z=57) and gadolinium (Gd, Z=64)
- **Computed radiography** (CR) and **digital radiography** (DR) acquisition – europium (Eu, Z=63) and cesium (Cs, Z=55)
- Increased absorption probabilities improve subject contrast and quantum detective efficiency
- At photon **E << 50 keV**, the photoelectric effect plays an important role in **imaging soft tissue**, amplifying small differences in tissues of slightly different Z, thus improving subject contrast (e.g., in mammography)

Example of Contrast Agents

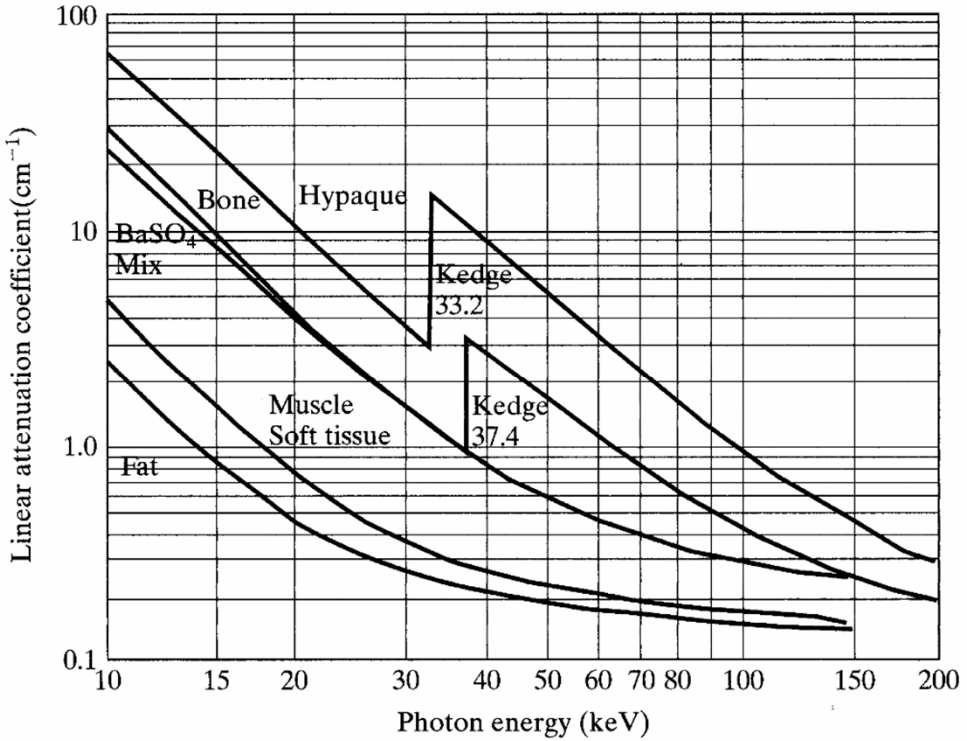

Figure 5.8
Linear attenuation coefficients of bone, muscle, fat, and two contrast agents. (From Johns and Cunningham, 1983.)

Bring out the difference between fat and soft tissues

X-ray Generation – Characteristic X-rays

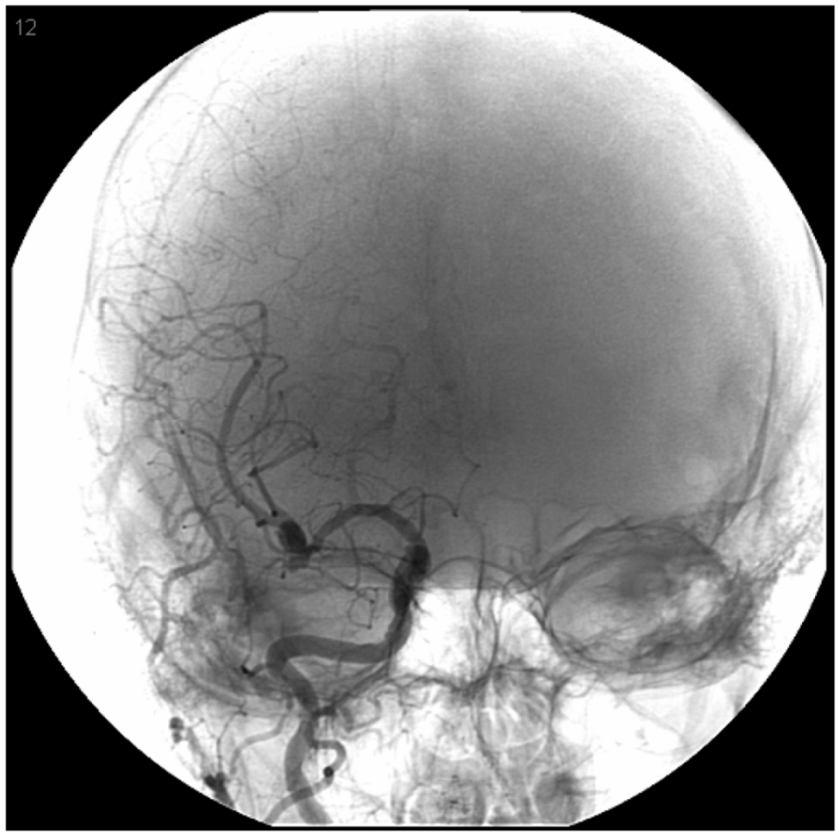

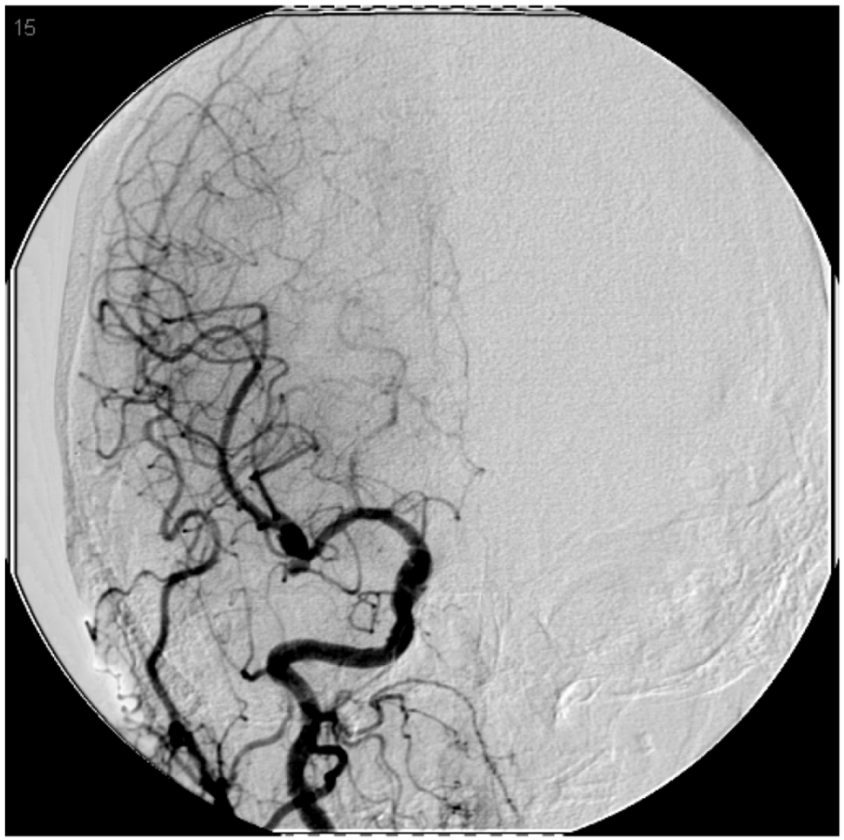

This is a mask image showing the background bone which obscures many of the smaller vessels.

Subtracted image with the background details removed.

Both images from Bushberg et al. 2003

X-ray Imaging Detectors

X-Ray Detectors

- Film: sensitivity is very low, it would require too high a dose to the patient
- Film + screen: conventional radiography
- Image intensifier (I.I.): fluoroscopy
- Photosensitive phosphor (computed radiography)
- **Flat panel detectors**
- **Direct digital radiography (semiconductor)**

X-Ray Film-screen Detectors

Radiographic Cassettes

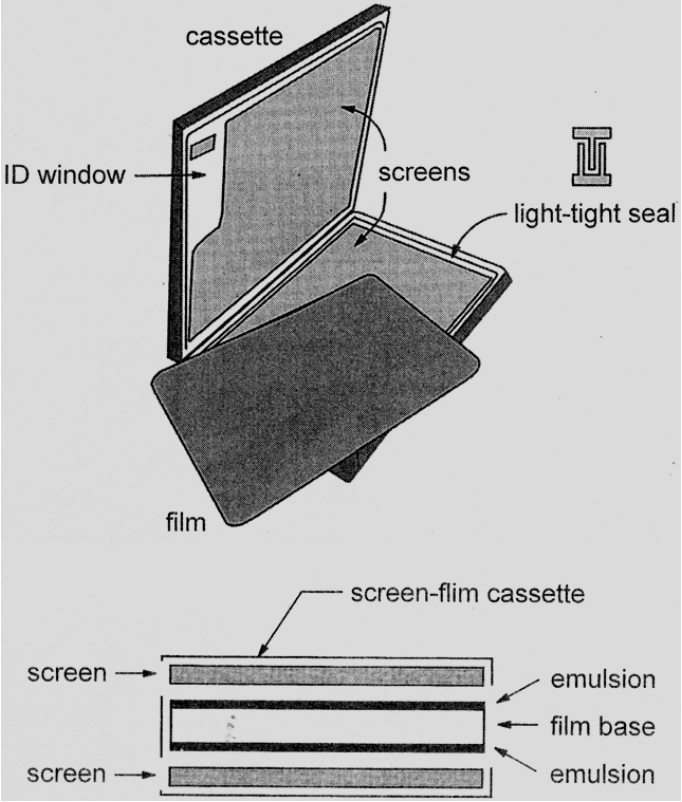

Light-tight and ensures screen contact with film

- Front surface - carbon fiber
- ID flash card area on back
- 1 or 2 Intensifying Screens
- Mounted on layers of compressed foam (produces force)

Sheet of film

- Register the x-ray distribution
- Chemically processed
- Storage and display

Film-screen based X-Ray Radiology

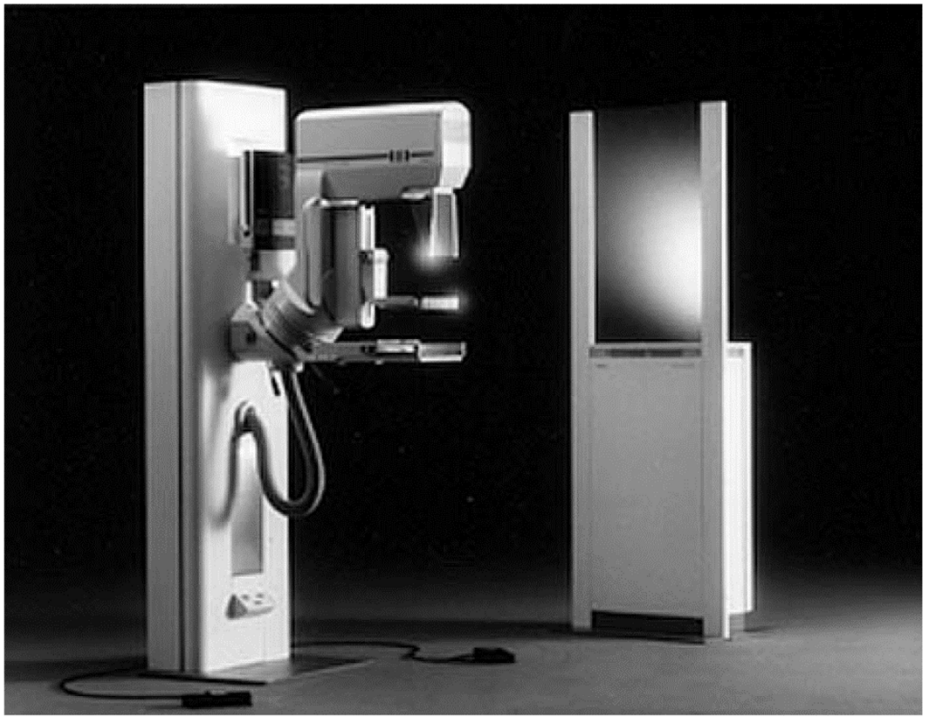

Requirements:

- Low energy x-ray photons for better soft tissue differentiation.
- High resolution (0.1 mm) for diagnosing micro-calcifications.

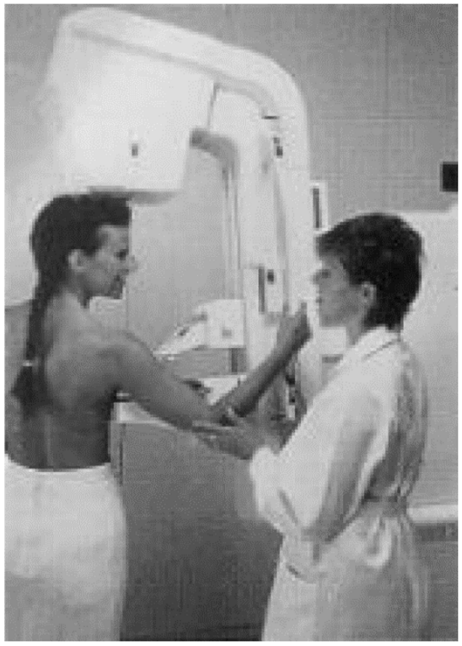

Breast compression
=> short exposure time

Image Plate based X-Ray Radiology

tal X-ray image acquisition systems for projection radiography.

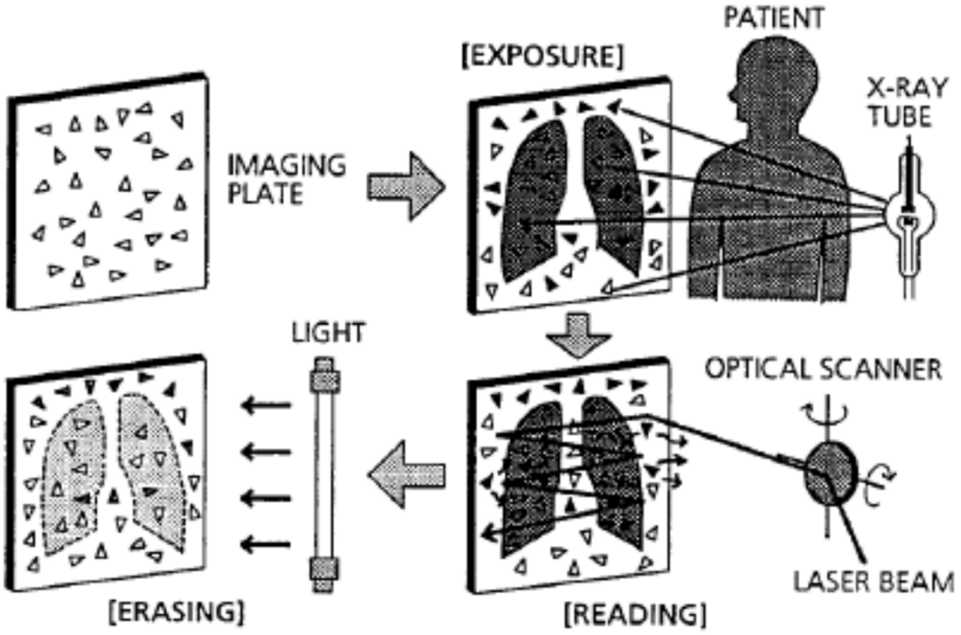

Stimulatable Phosphor System

ing plate (stimulable phosphor) is exposed forming a
ıt image ("traps" in phosphor).
ıt image is read via laser scanning --> stored energy is
ısed in form of "photostimulated luminescence light"
ortional to the local X-ray exposure.
luminescence signal is converted to an electrical signal
is digitized.

X-Ray Image Intensifier (X-ray II)

Principle Operation of XRII

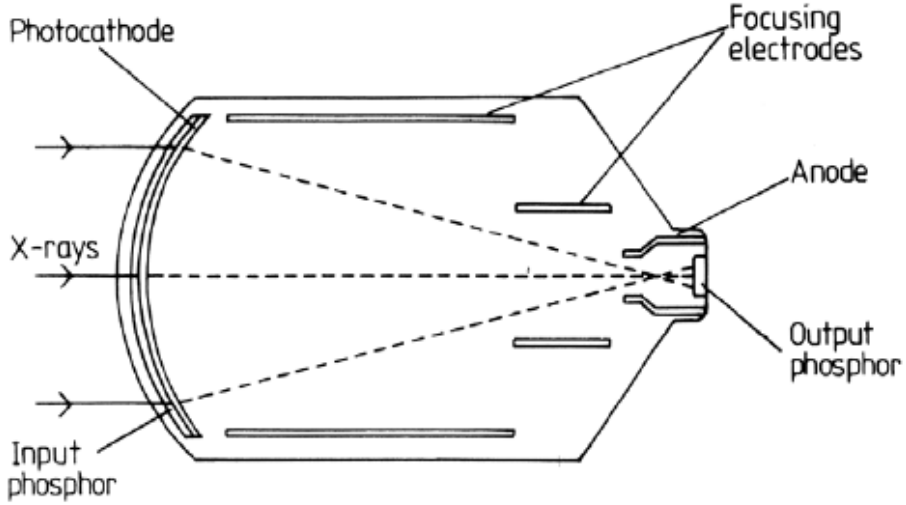

Construction of the image intensifier.

- X-rays are absorbed in CsI input phosphor.
- Emitted light is converted to electrons by photocathode.
- Electrons are focused and accelerated to output phosphor and converted to light..
- Bright light image at output window is imaged by TV-camera.

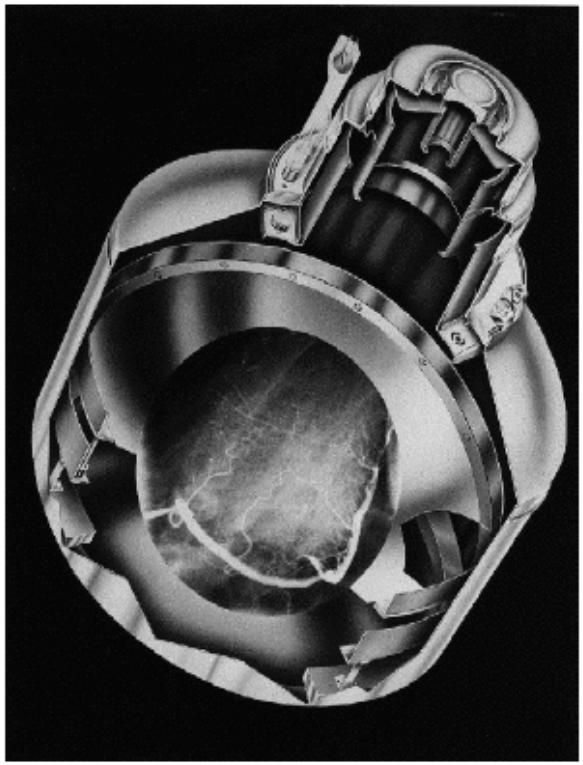

Medical Image Processing (Med Img 1) 39

The Energy Band Structures in Solids

- The energy of any electron within the pure material must be confined to one of these energy bands, which may be separated by gaps or ranges of forbidden energies.
  - Valence band: corresponds to outer shell electrons that are bound to specific lattice sites.
  - Conduction band: represents electrons that are free to migrate through the crystal → conductivity of the material.
  - Band gap: the minimum difference in the energies that can be possessed by electrons in the valence band and the conduction band.

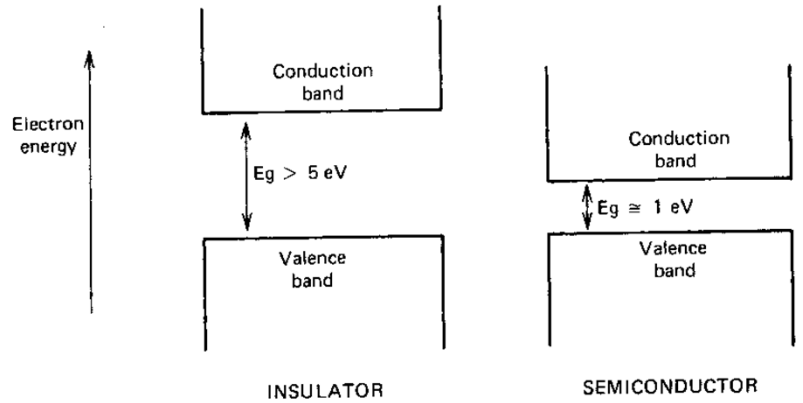

Figure 11.1 Band structure for electron energies in insulators and semiconductors.

The Energy Band Structures in Solids

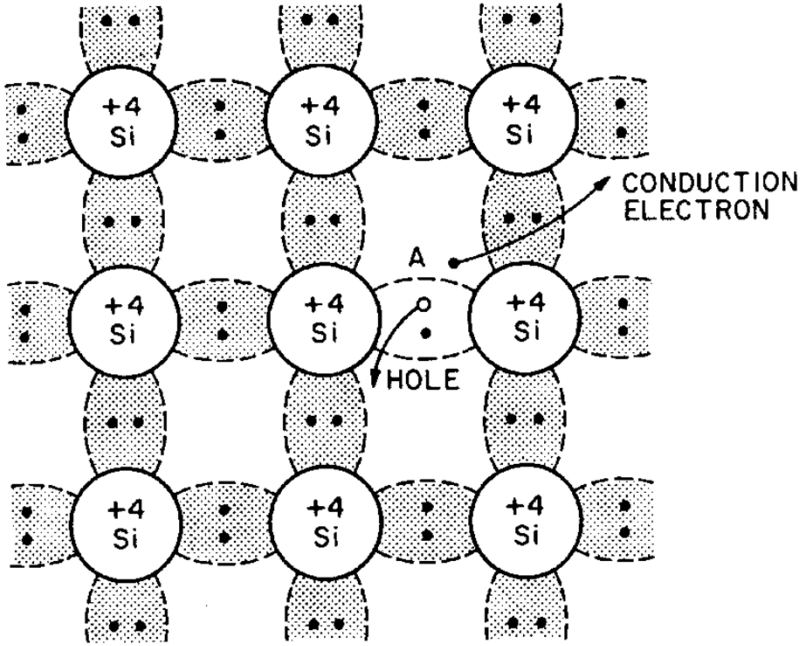

Schematic bond representation of a single crystal with one broken bond in the center. (After Sze 1985, p9, Fig 7)

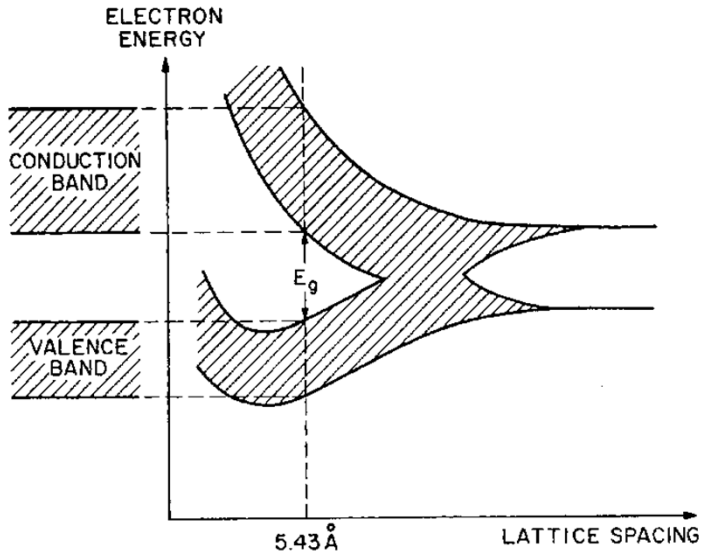

Energy levels of silicon atoms arranged in a diamond structure as a function of lattice spacing. (After Sze 1985, p9, Fig 7)

The Energy Band Structures in Solids

- In semiconductors, the relatively small band gap may permit a small number of electrons to possess energies in the conduction band.
- The number of electrons in the conduction band is equal to the number of holes in the valence band.
- Fermi energy lies midway in the forbidden gap at an energy $E_0 + E_G/2$.

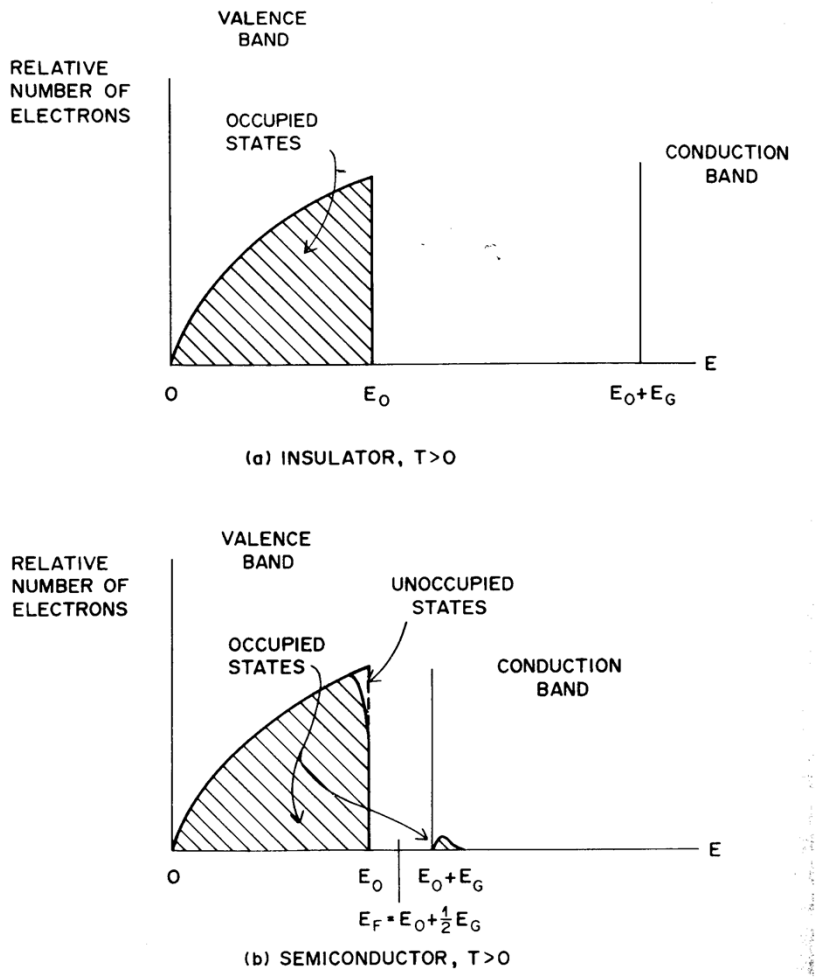

FIGURE 10.13. Relative number of electrons in valence and conduction bands of (a) an insulator and (b) a semiconductor with $T > 0$.

Charge Carriers in Semiconductor Materials

The so-called charge carriers in semiconductors consist of the following two components

- ☞ Electrons elevated to the conduction band.
- ☞ Vacancies in the valence band. The migration of electrons in the valence band results in a net effect of moving positive charges (hole).

The probability per unit time that an electron-hole pair is thermally generated is given by

$$p(T) = CT^{3/2} \exp\left(-\frac{E_g}{2kT}\right)$$

where

T = absolute temperature

E_g = bandgap energy

k = Boltzmann constant

C = proportionality constant characteristic of the material

Effect of Impurities and Dopants – Intrinsic Semiconductors

An example from Knoll, p. 360.

The leakage current (I) through a detector, of area A and thickness t, is related to the resistivity of the material as

$$I = \frac{A \cdot V}{\rho \cdot t} \text{ or } \rho = \frac{A \cdot V}{I \cdot t}$$

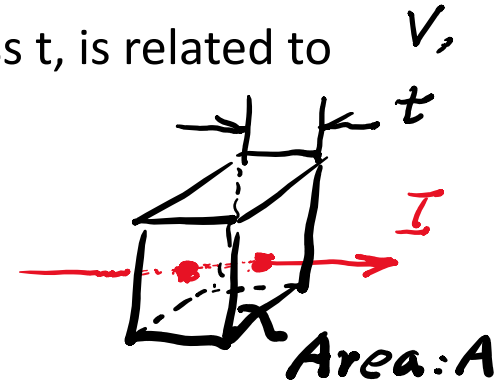

be their sum, with each term given by the product of the area, intrinsic carrier density, electronic charge e, and the drift velocity of the charge carrier. Thus

$$I = I_e + I_h = An_i e(v_e + v_h)$$

From Eqs. 11.2 and 11.3

$$I = An_i e\mathscr{E}(\mu_e + \mu_h) = An_i e\frac{V}{t}(\mu_e + \mu_h)$$

Combining

$$\rho = \frac{1}{en_i(\mu_e + \mu_h)} \qquad (11.8)$$

Effect of Impurities and Dopants – Intrinsic Semiconductors

An example from Knoll, p. 360.

$$I = \frac{A \cdot V}{\rho \cdot t} \text{ or } \rho = \frac{A \cdot V}{I \cdot t}$$

Inserting numerical values for intrinsic silicon at room temperature:

$$\rho = \frac{1}{(1.6 \times 10^{-19} C)(1.5 \times 10^{10}/\text{cm}^3)(1350 + 480)\ \text{cm}^2/V \cdot s}$$

$$\rho = 2.3 \times 10^5 \frac{V \cdot s \cdot \text{cm}}{C} = 230{,}000\ \Omega \cdot \text{cm}$$

Presently available silicon material of the highest purity falls short of achieving this resistivity value because of the effect (discussed in the following sections) of residual impurities.

Consider a device of 1mm × 1 mm area and 1 mm thickness, with 100V applied across the 1 mm thickness, then the leakage current is

$$I = \frac{A \cdot v}{\rho \cdot t} = \frac{(0.1cm)^2 \cdot 100V}{2.3 \times 10^5 \Omega \cdot cm \cdot (0.1cm)} = 4.3 \times 10^{-5} A = 2.7 \times 10^{14} \text{e/s}$$

Effect of Impurities and Dopants – Intrinsic Semiconductors

Consider a device of 1mm × 1 mm area and 1 mm thickness, with 100V applied across the 1 mm thickness, then the leakage current is

$$I = \frac{A \cdot v}{\rho \cdot t} = \frac{(0.1cm)^2 \cdot 100V}{2.3 \times 10^5 \Omega \cdot cm \cdot (0.1cm)} = 4.3 \times 10^{-5} A = 2.7 \times 10^{14} \text{e/s}$$

Consider a pulse induced by an X-ray lasts for 1 μs, then there will be

$$n_L = 2.7 \times 10^{14} \text{e/s} \times 10^{-6} \text{ s} = 2.7 \times 10^{-8} \text{ e/ μs}$$

Electrons flowing through the device during the X-ray induced pulse. Then the statistical fluctuation of the leakage current is

$$\sigma(n_L) = \sqrt{n_L} = \sqrt{2.7 \times 10^8} = 1.6 \times 10^4 \text{ e}$$

However, the signal induced by a 100 keV X-ray in silicon is only

$$100{,}000 \text{ eV} / 5 \text{ eV} = 2 \times 10^4 \text{ e}$$

Comparison of Intrinsic and Extrinsic Semiconductors

N-type ***P-type***

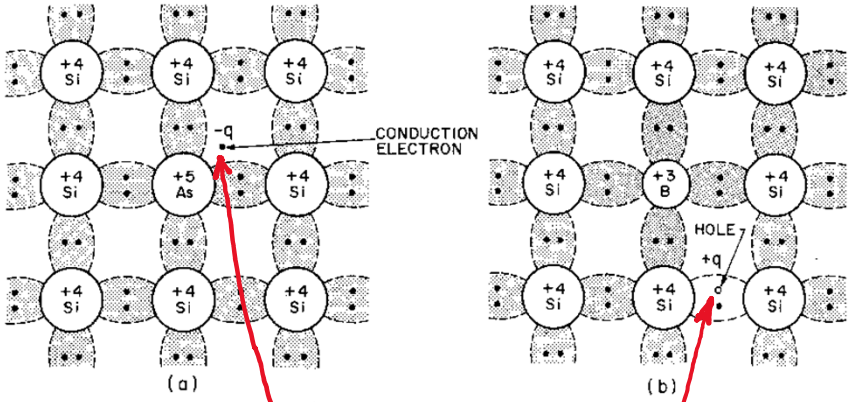

Fig. 2.8a,b. Bond representation of *n*-type (a) and *p*-type (b) semiconductors. (After Sze 1985, p. 21 Fig. 21)

Majority charge carriers

Minority charge carriers

Minority charge carriers

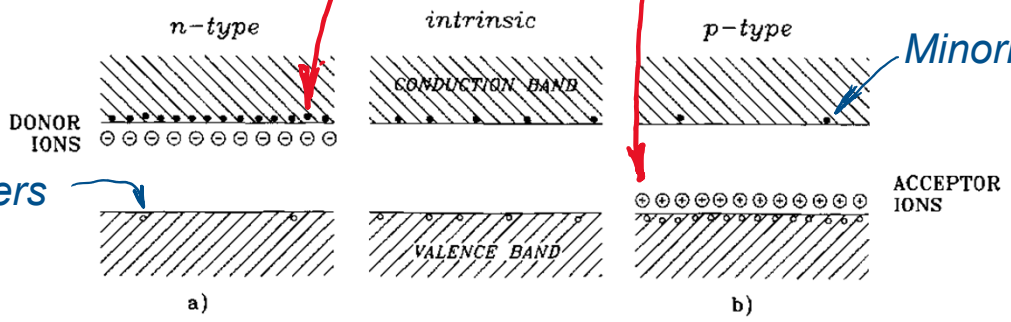

Fig. 2.9a,b. Schematic energy band representation of extrinsic *n*-type (a) and conductors

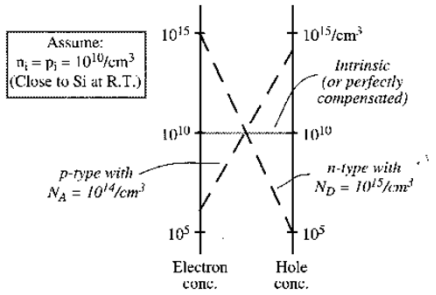

Figure 11.5 Nomogram showing the relationship between electron and hole concentrations in a semiconductor. Lines connecting points on the two logarithmic scales always pass through the center of the diagram for any type or degree of doping.

Comparison of Intrinsic and Extrinsic Semiconductors

- The increase of majority carriers (electrons in the case of n-type material and holes in the case of p-type materials) is accompanied by a decrease of minority carriers according to the following law

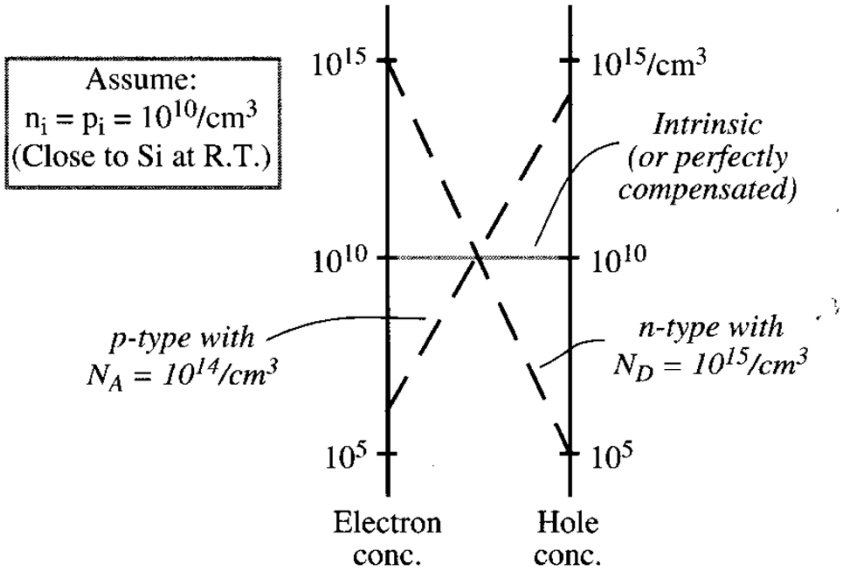

Figure 11.5 Nomogram showing the relationship between electron and hole concentrations in a semiconductor. Lines connecting points on the two logarithmic scales always pass through the center of the diagram for any type or degree of doping.

Effect of Impurities and Dopants

- The concentration of holes greatly exceeds the concentration of electrons in the conduction band.
- The concentration of holes (p) is completely dominated by the contribution from the acceptor impurity, so that

$$p \cong N_A$$

- Similarly, the concentration of electrons and holes is given by

$$np = n_i p_i$$

Semiconductors Junctions

- The usefulness of semiconductors as radiation detectors stems from the special properties created at a junction where n- and p- type semiconductors are brought into good thermodynamic contact.

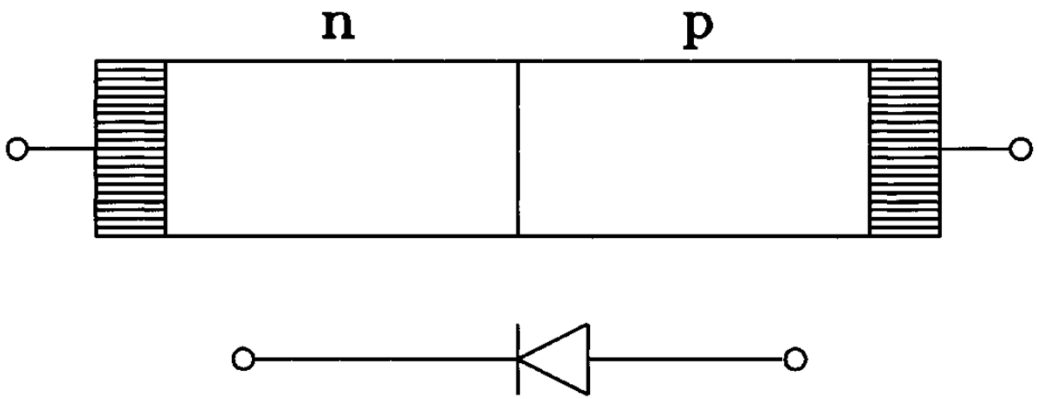

Fig. 3.1. A p–n diode junction: structure and device schematic

N-type

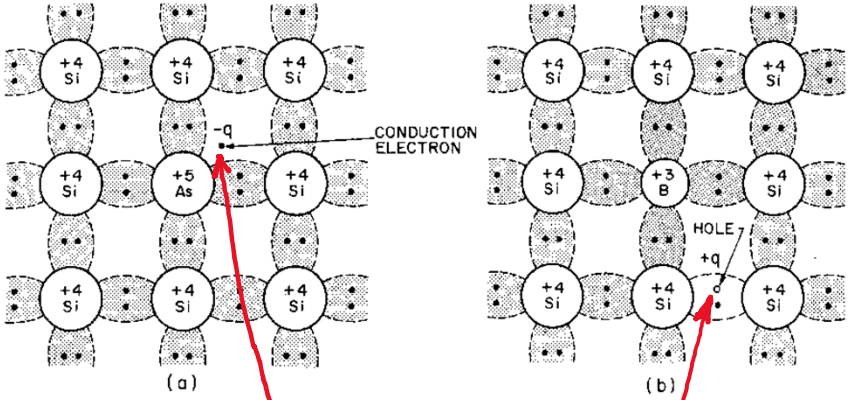

P-type

Fig. 2.8a,b. Bond representation of *n*-type (a) and *p*-type (b) semiconductors. (After Sze 1985, p. 21 Fig. 21)

Majority charge carriers

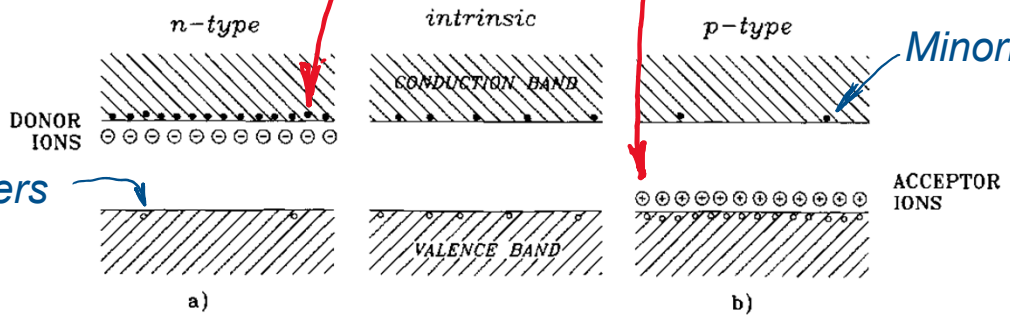

Minority charge carriers

Minority charge carriers

PN-junction

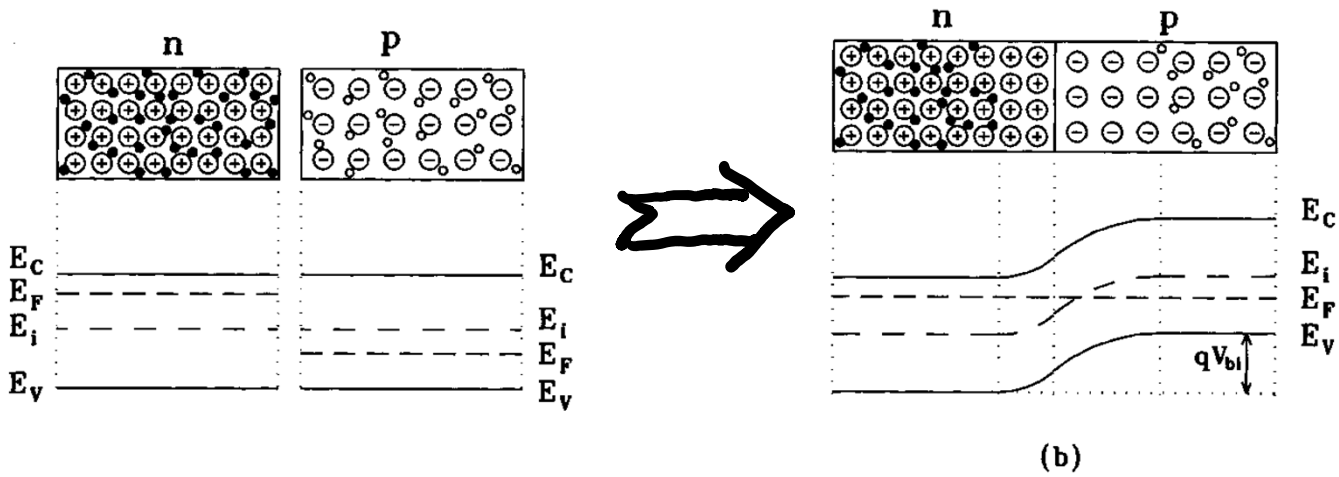

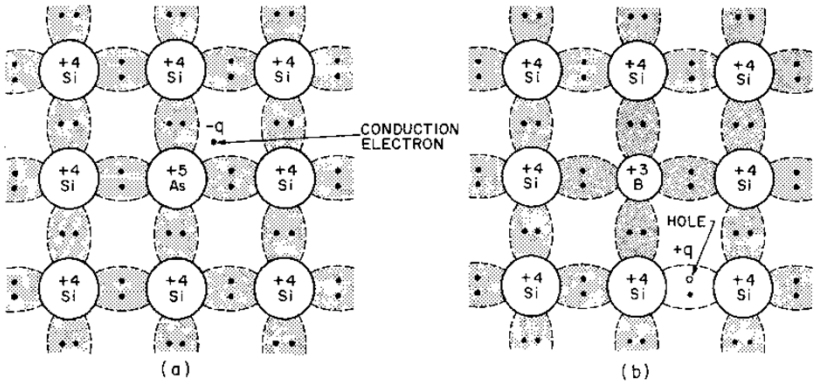

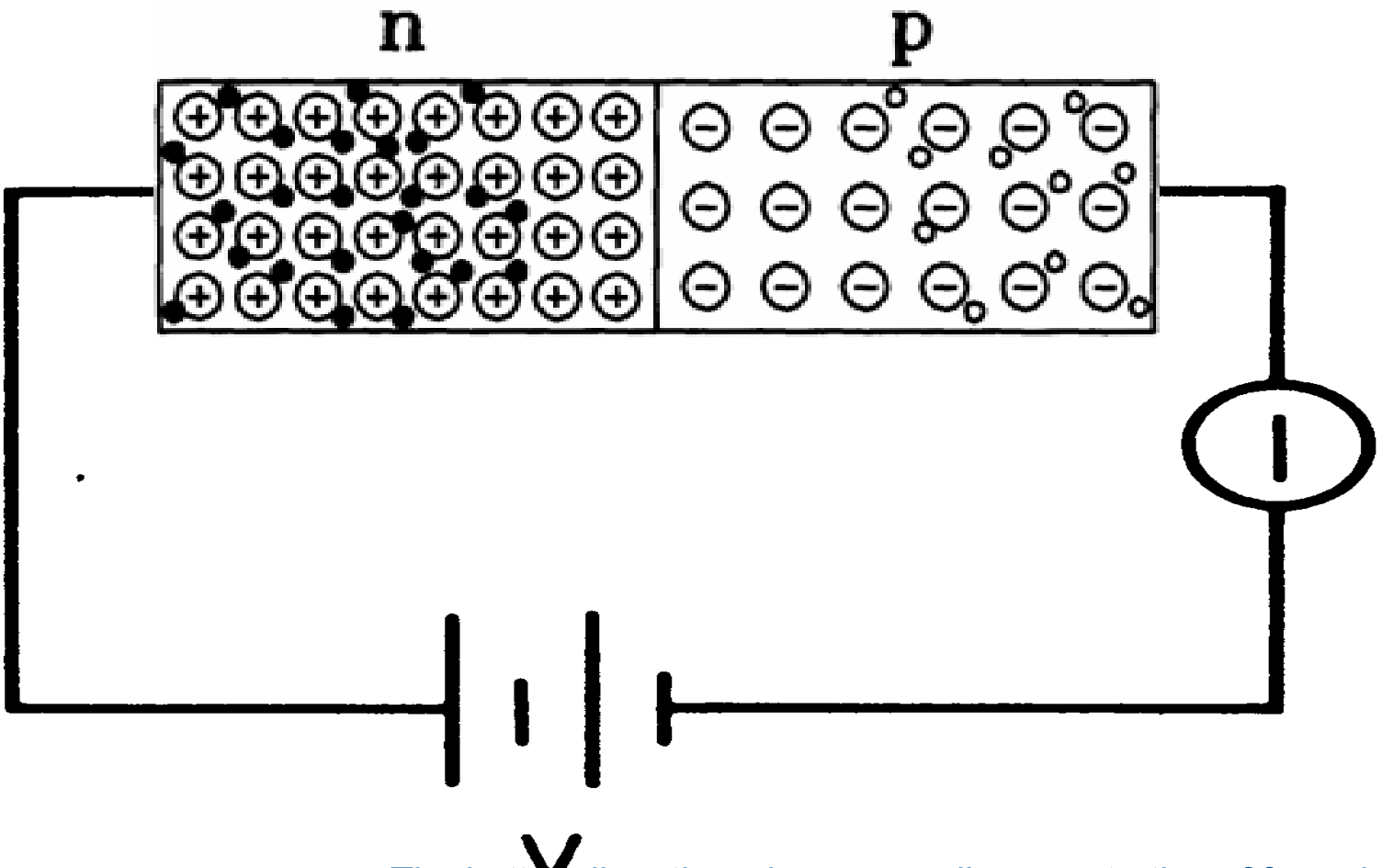

The bottom line: there is very small concentration of free-electrons that can move across the junction to form the leakage current → Leakage currently is greatly suppressed → Noise in detector is greatly reduced…

Biased Semiconductors Junctions

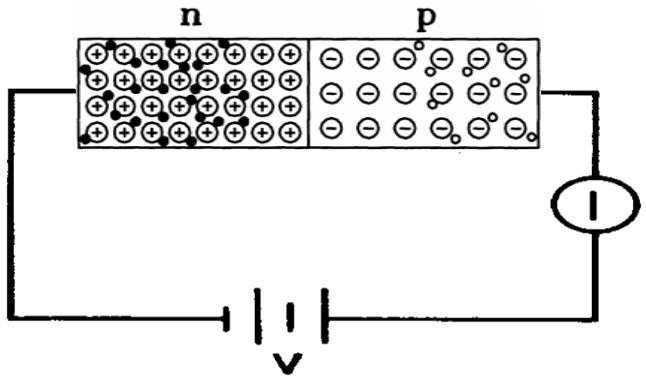

(a) FORWARD BIAS

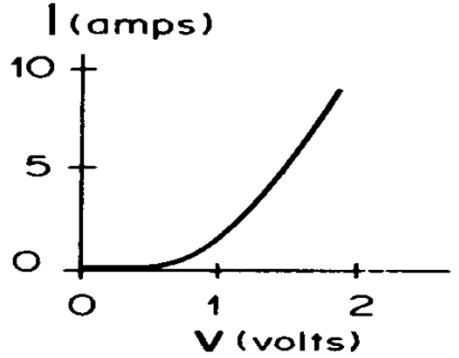

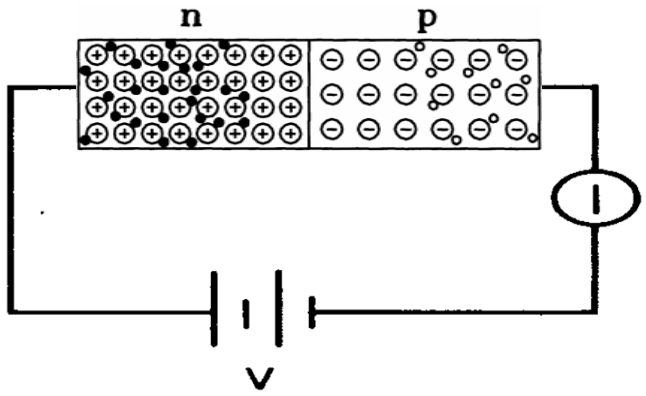

(b) REVERSE BIAS

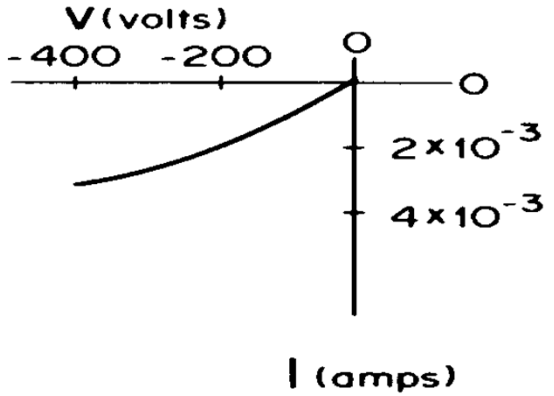

FIGURE 10.19. (a) Forward- and (b) reverse-biased n–p junctions and typical curves of current vs. voltage. Note the very different scales used for the two curves. Such an n–p junction is a good rectifier.

Photodiode Detectors

Figure 1-1 Photodiode cross section

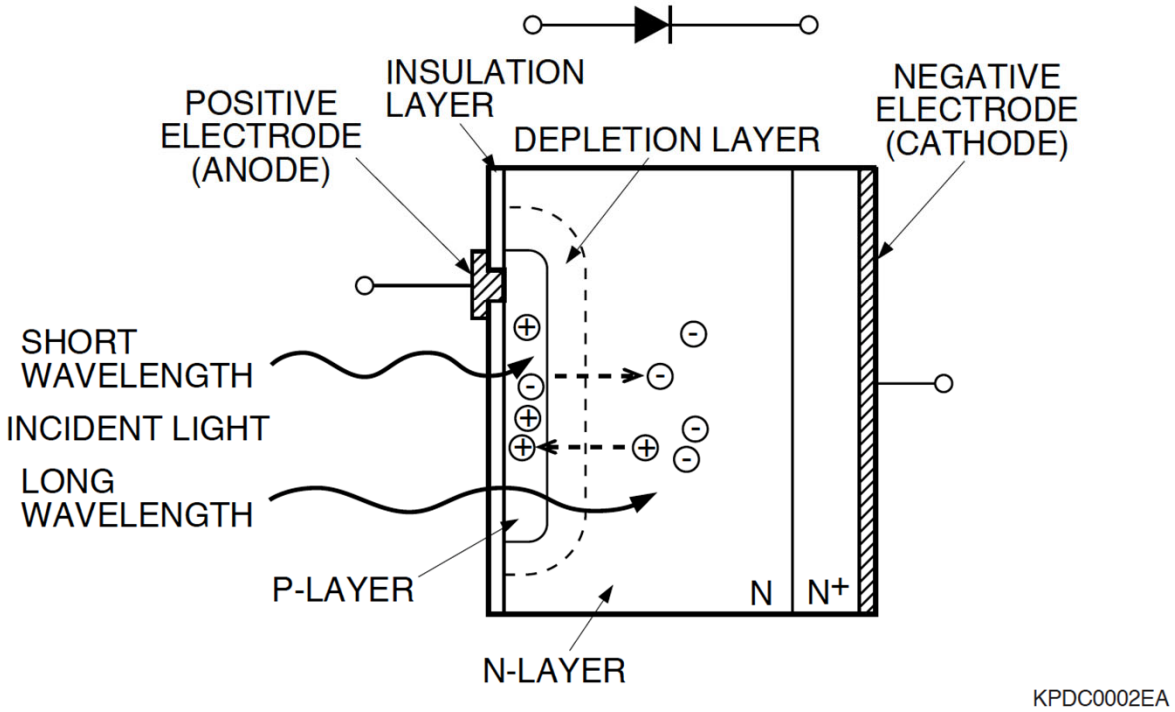

Typical reversed-biased photodiode detectors

- *No internal gain*
- *Very high QE for red light (up to 90%)*
- *Limited timing resolution*

Hamamatsu photodiode technical information

Avalanche Photodiode (APD)

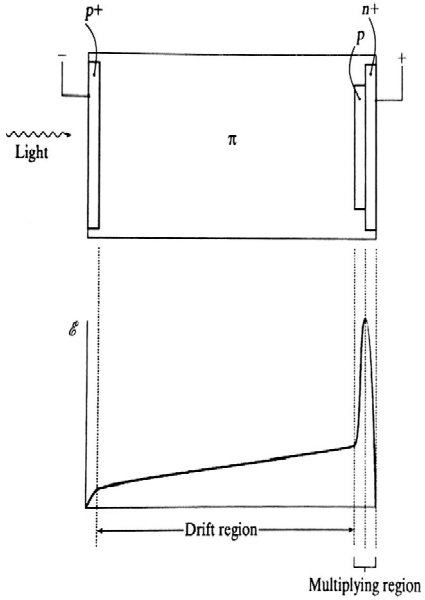

From K F Knoll, Radiation Detection and Measurements, Third Edition, Wiley.

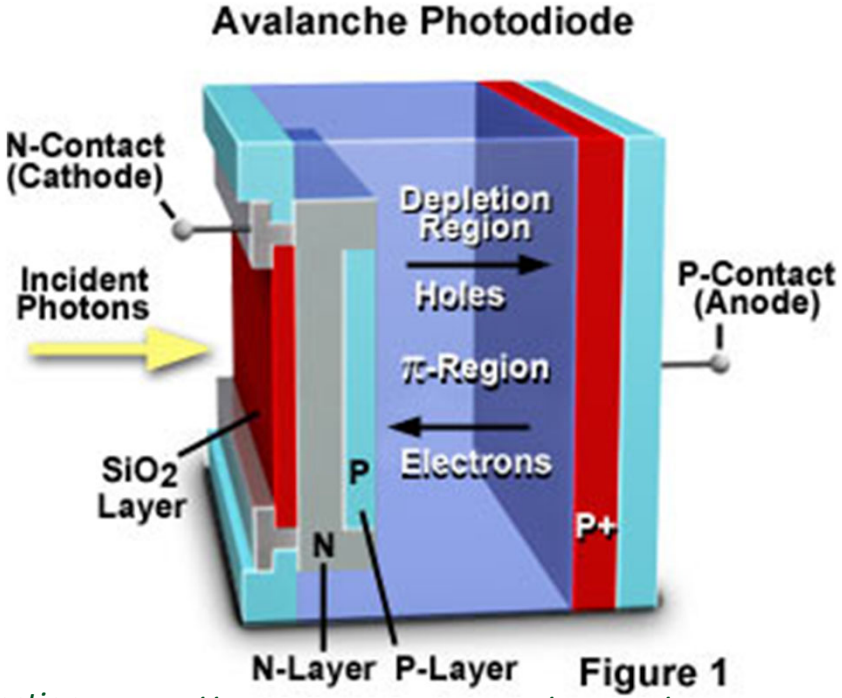

Figure 1

http://learn.hamamatsu.com/articles/avalanche.html

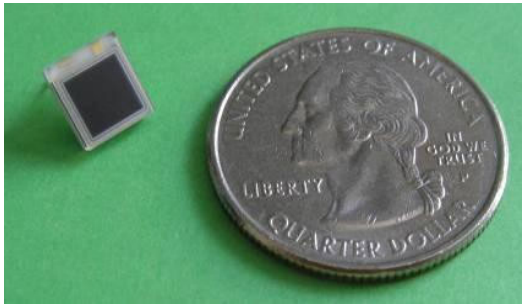

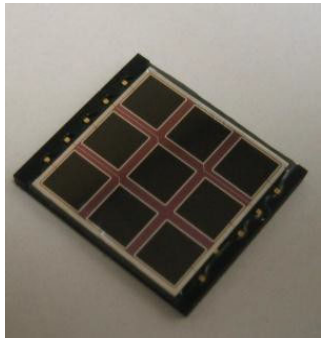

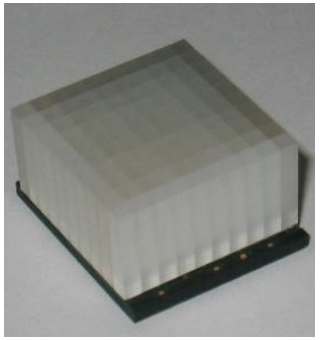

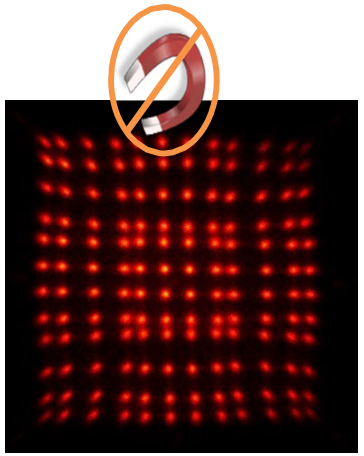

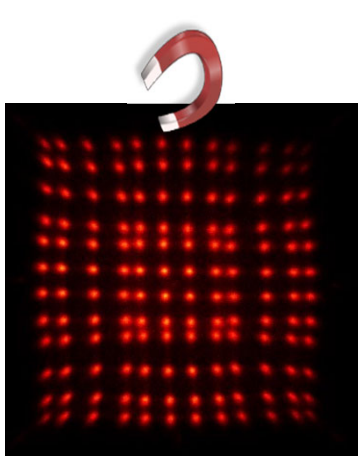

***Avalanche Photo Diodes (APD)**, proof to be suitable detectors for PET/MRI*

- *Could be operated inside strong magnetic field*
- *Added internal gain*
- *Fast timing property*
- *Gain critically depends on bias voltage*
- *Temperature stability could be an issue*

CCD (Charge-Coupled Devices)

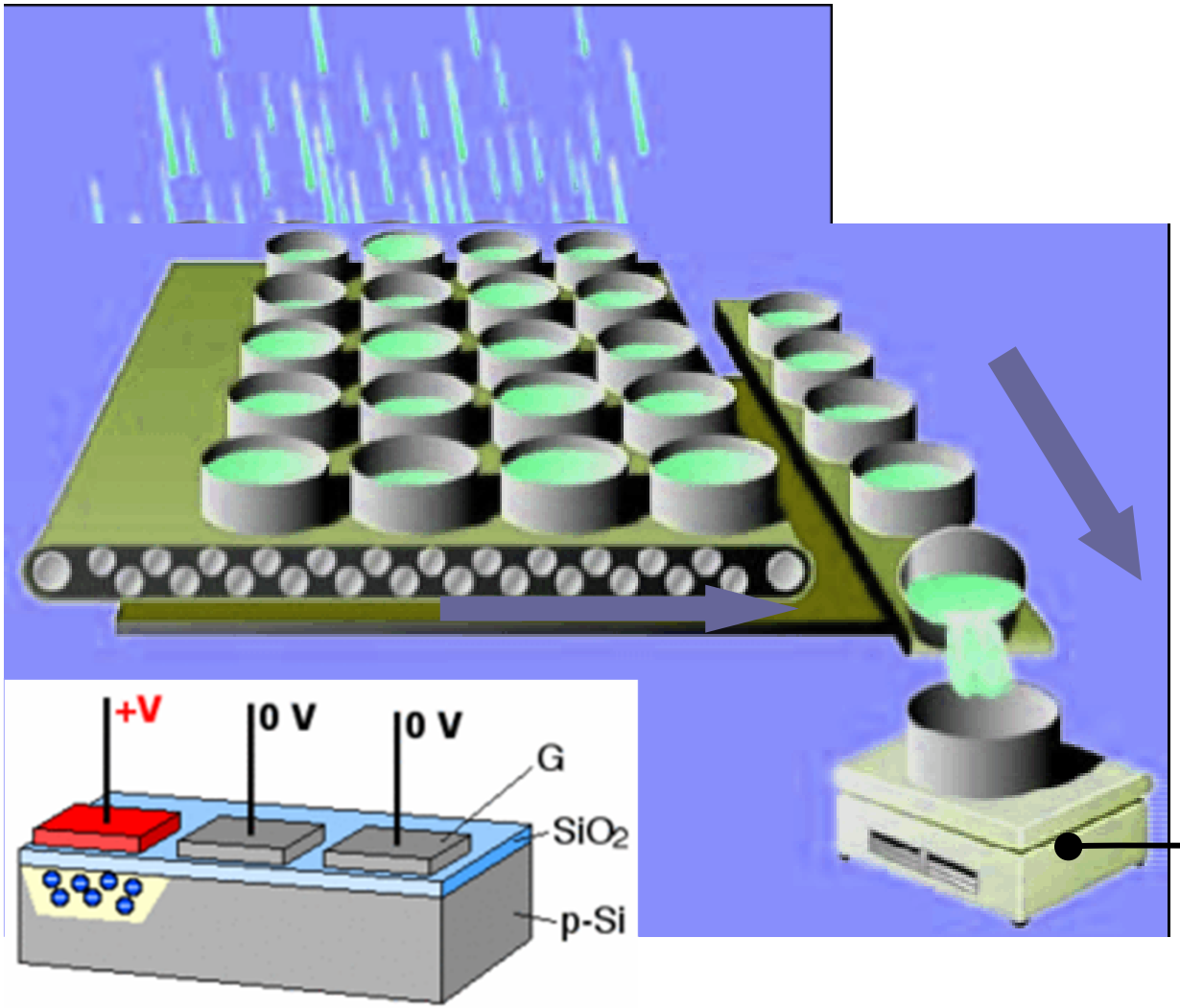

Bucket Brigade

- Integration
- Charge Shift and Read-out

Charge Amplifier

Charge Transfer Efficiency (CCD Features)

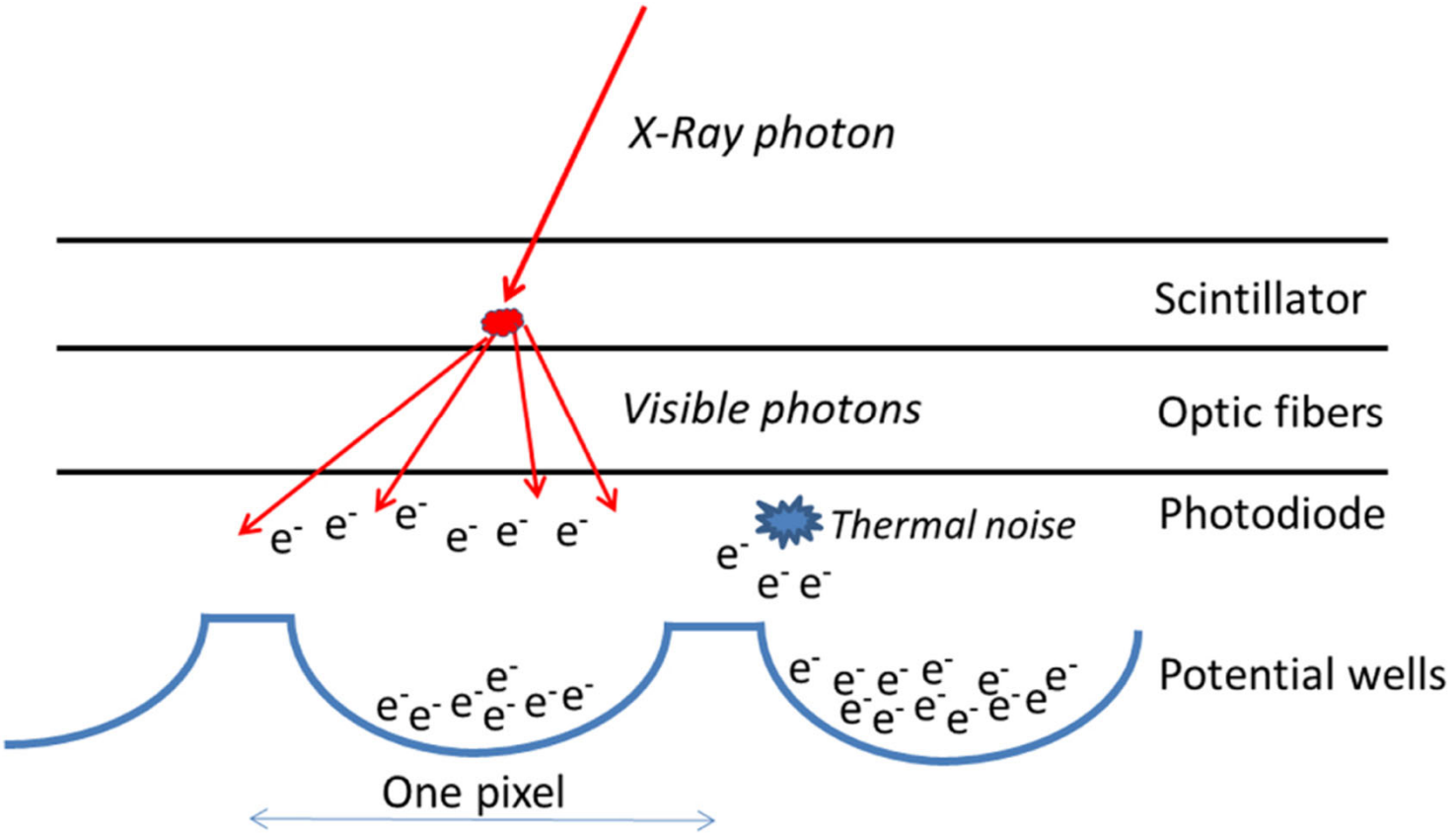

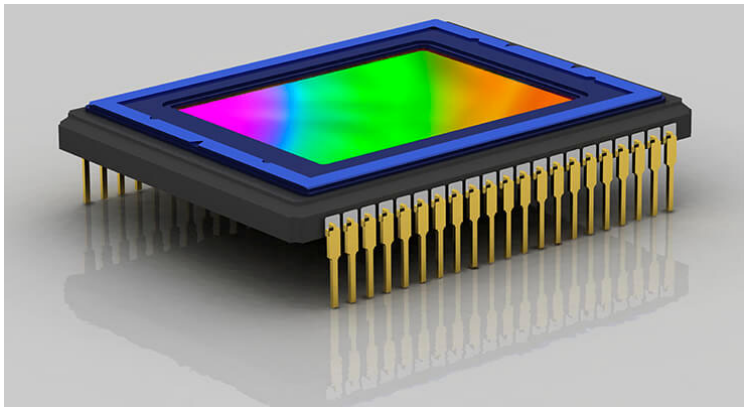

Complementary metal–oxide–semiconductor (CMOS) Sensors

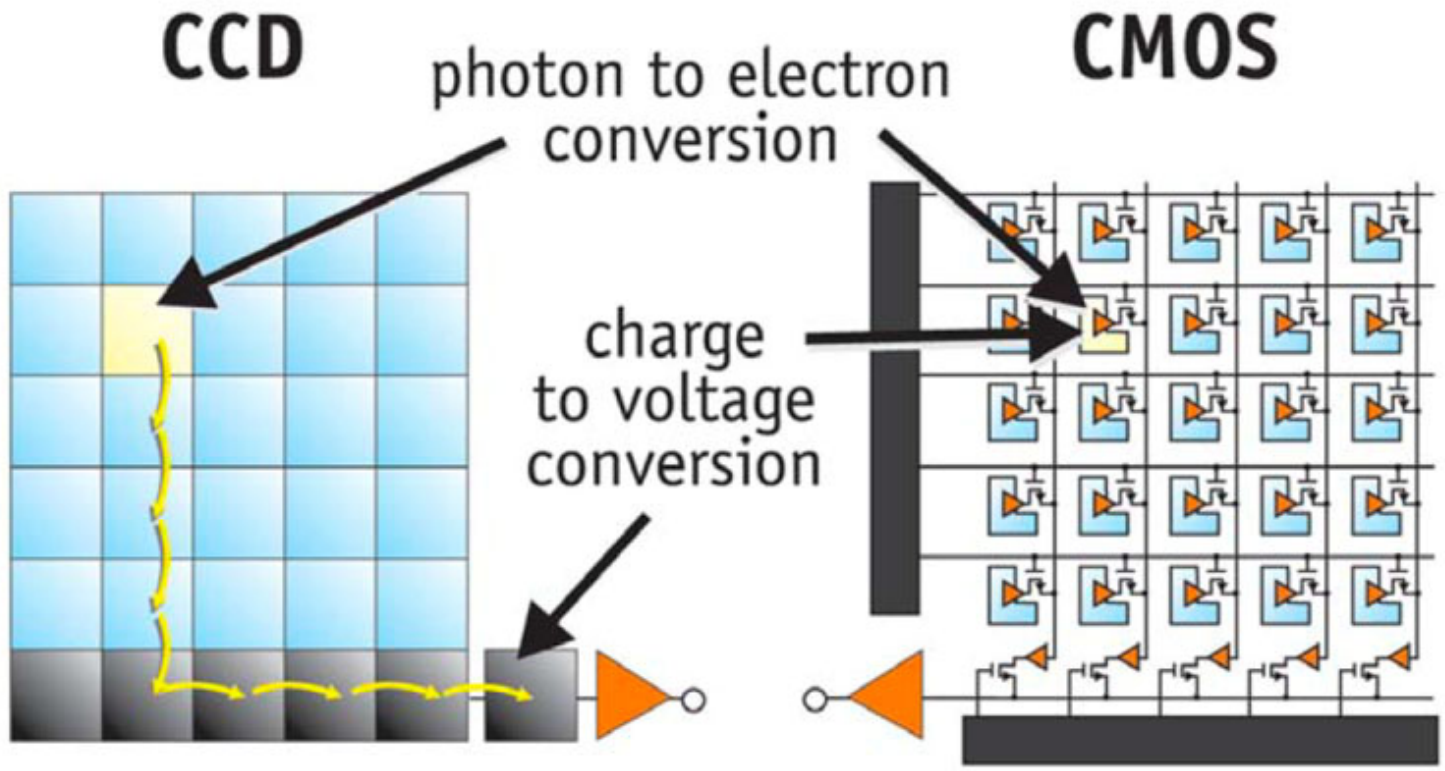

CCDs move photogenerated charge from pixel to pixel and convert it to voltage at an output node. CMOS imagers convert charge to voltage inside each pixel.

Image courtesy of http://meroli.web.cern.ch/meroli/lecture_cmos_vs_ccd_pixel_sensor.html

Flat Panel Detectors

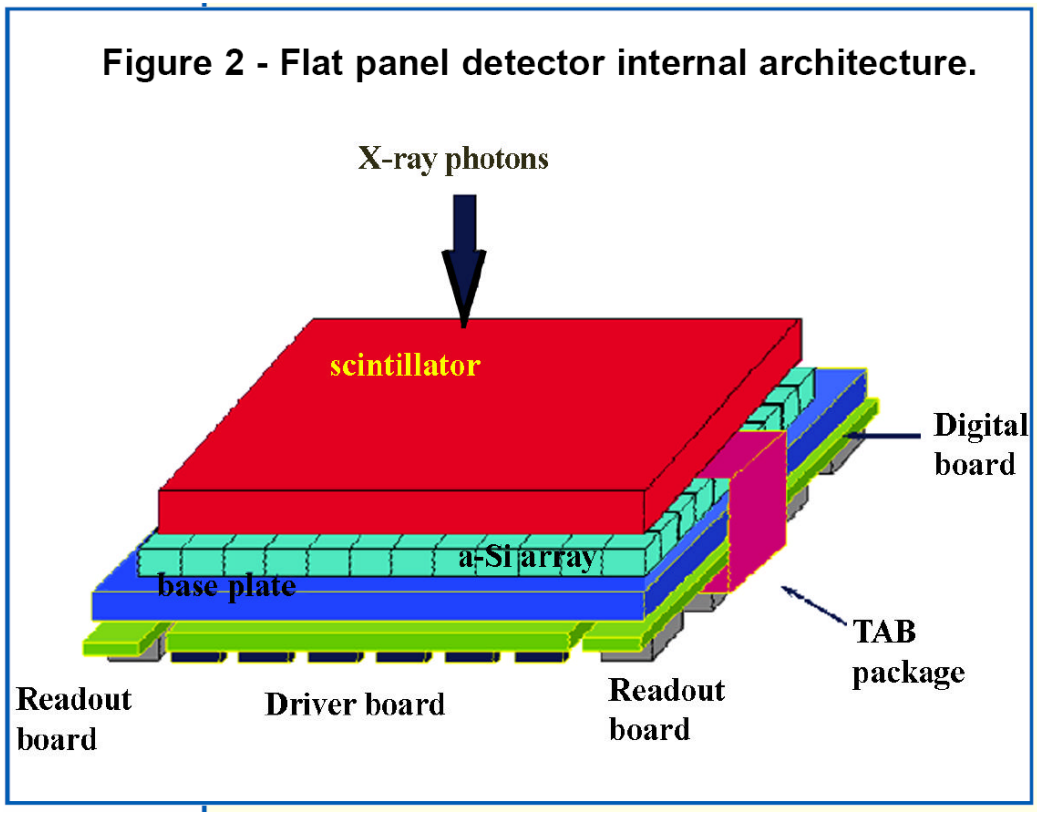

The construction of FPDs is similar in many ways to flat panel displays, and uses many of the same technologies. Figure 2 shows the construction of a typical FPD. At the core is an amorphous-silicon TFT/photodiode array. Closely coupled to the array is the X-ray scintillator.

http://www.varian.com/xray/pdf/Flat%20Panel%20Xray%20Imaging%2021-11-04.pdf

Scintillation Material as Detection Media

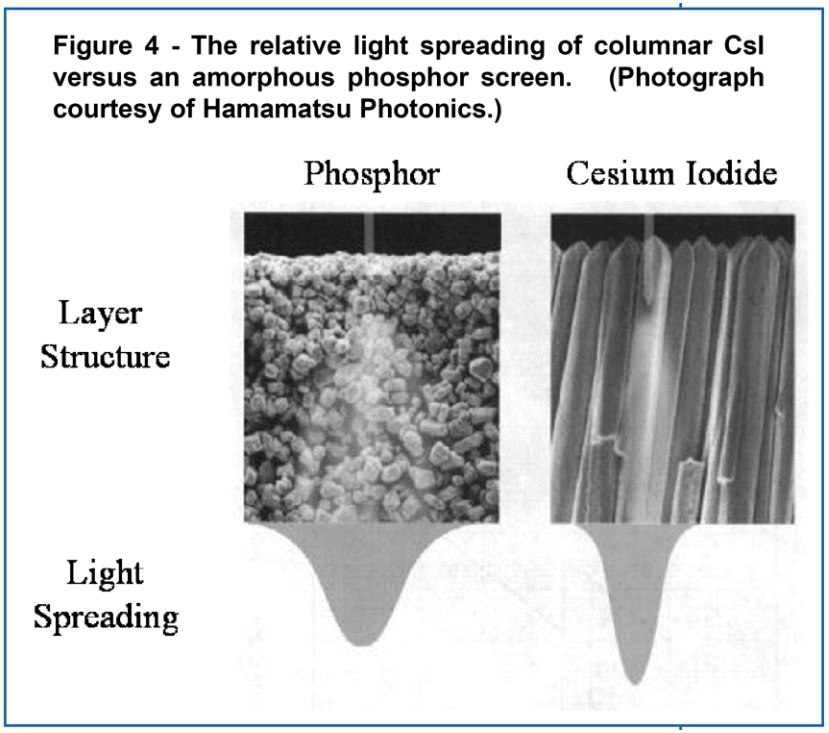

- CsI(Tl) scintillator: density 4.6g/cm^3, emission peak ~550nm.
- Columnar structure of up to 3mm thick to provide an adequate stopping power and a reduced light spread.

http://www.varian.com/xray/pdf/Flat%20Panel%20Xray%20Imaging%2021-11-04.pdf

Hybrid Pixel Detector

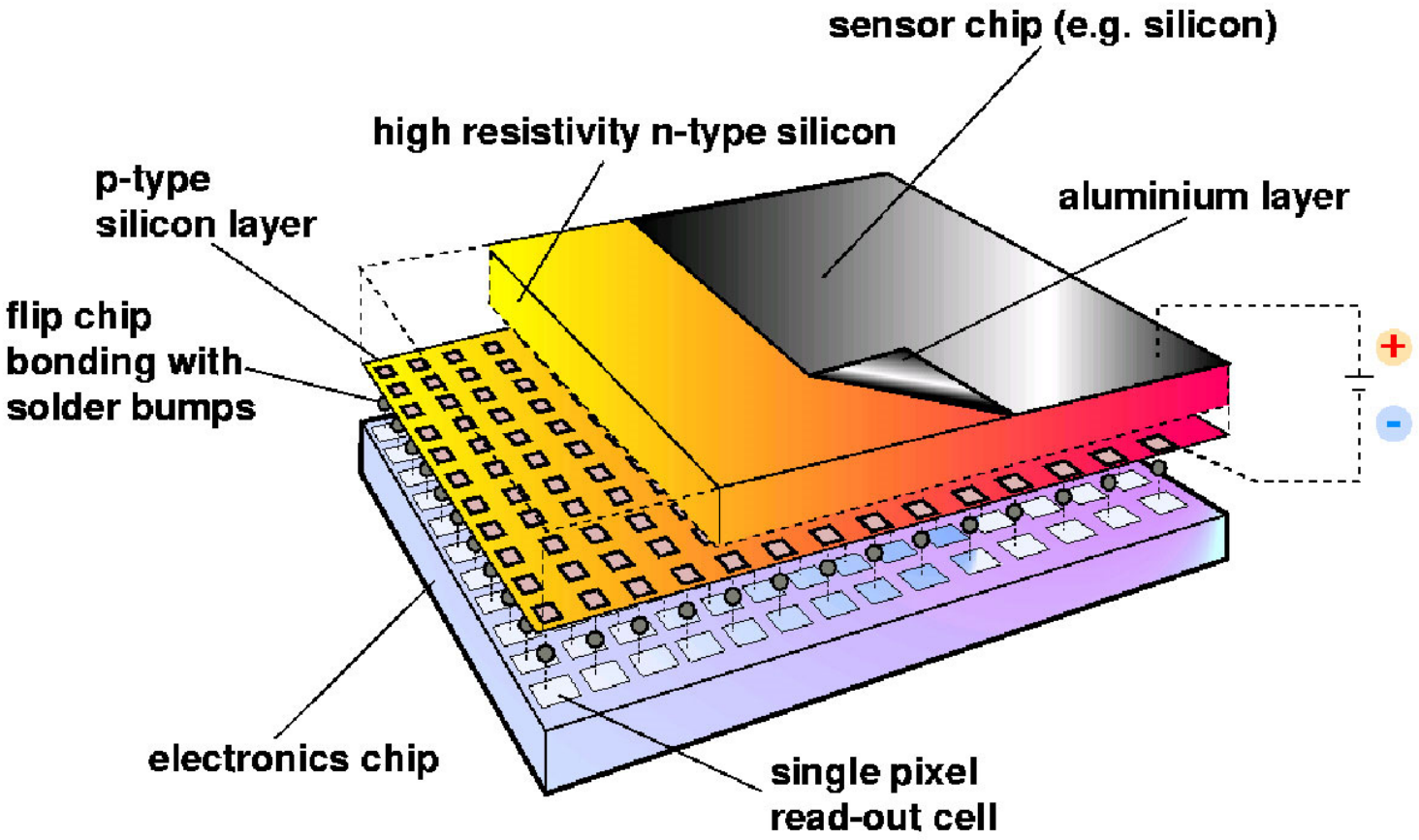

M. Campbell, V. Rosso, Rome IEEE NSS-MIC 2004 conference

Basic Principles for Imaging Formation

Basic Principle of Planar X-ray

2 % attenuation change detectable in film

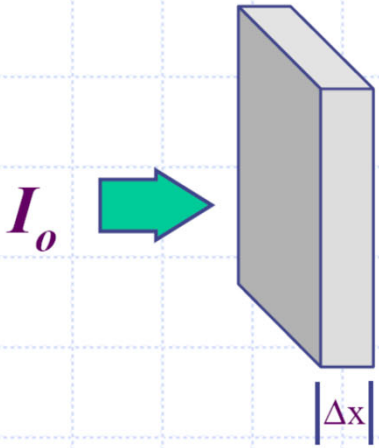

$$I = I_o e^{-\mu \Delta x}$$

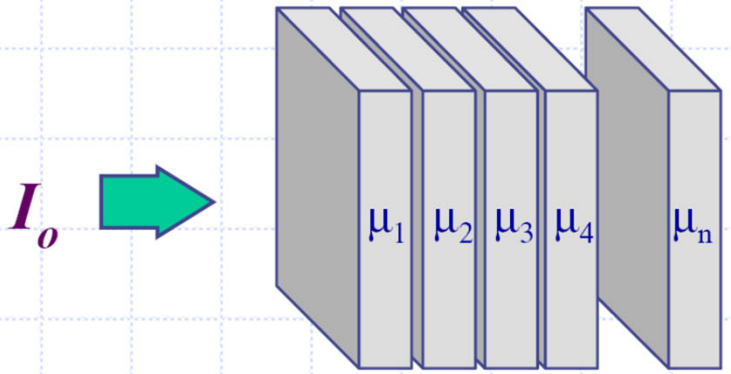

$$I = I_o e^{-\mu_1 \Delta x} e^{-\mu_2 \Delta x} \cdots e^{-\mu}$$

$$= I_o e^{-(\mu_1 + \mu_2 + \cdots + \mu_n)\Delta x}$$

$$\Delta x \to 0, \qquad P = -\ln\left(\frac{I}{I_o}\right) = \int_{-\infty}^{\infty} \mu(x)\, dx$$

Review of the X-ray CT Image Formation

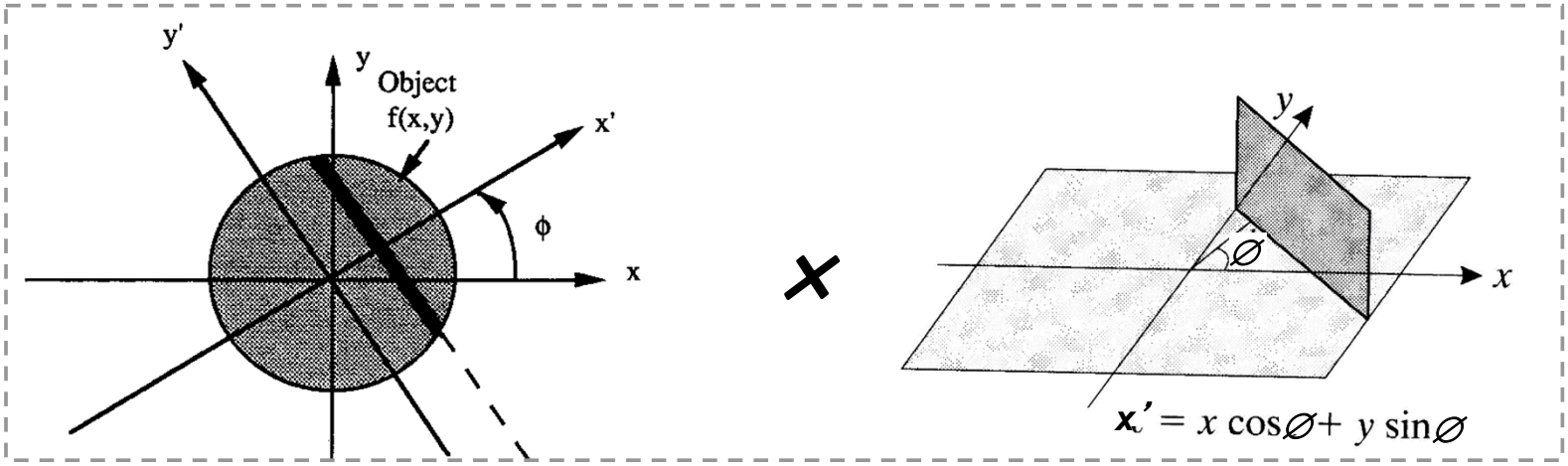

2-D integral

The value of the projection function $p_\phi(x')$ at this point is the integral of the function of f(x,y) along the straight line: $x' = x\cos\phi + y\sin\phi$

The integral of a line impulse function and a given 2-D signal gives the ***projection*** *data from a given view …*

$$p_\phi(x') = \int_{-\infty}^{\infty}\int_{-\infty}^{\infty} f(x,y)\delta(x\cos\phi + y\sin\phi - x')dxdy$$

Central Slice Theorem

$$F\{p(\phi, x')\} = F(r, \phi)$$

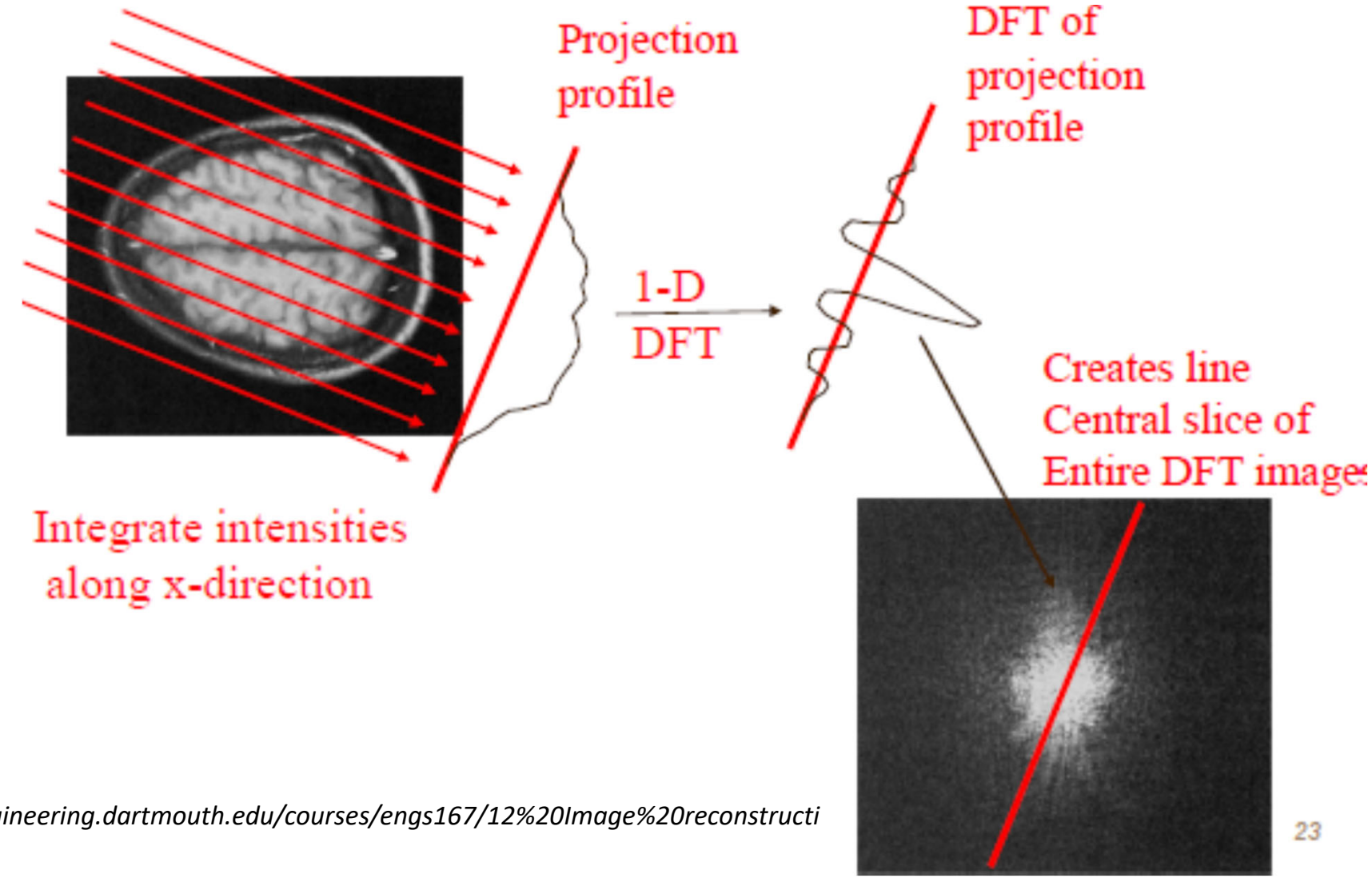

http://engineering.dartmouth.edu/courses/engs167/12%20Image%20reconstruction.pdf

23

Simple Back-projection and the 1/r Blurring

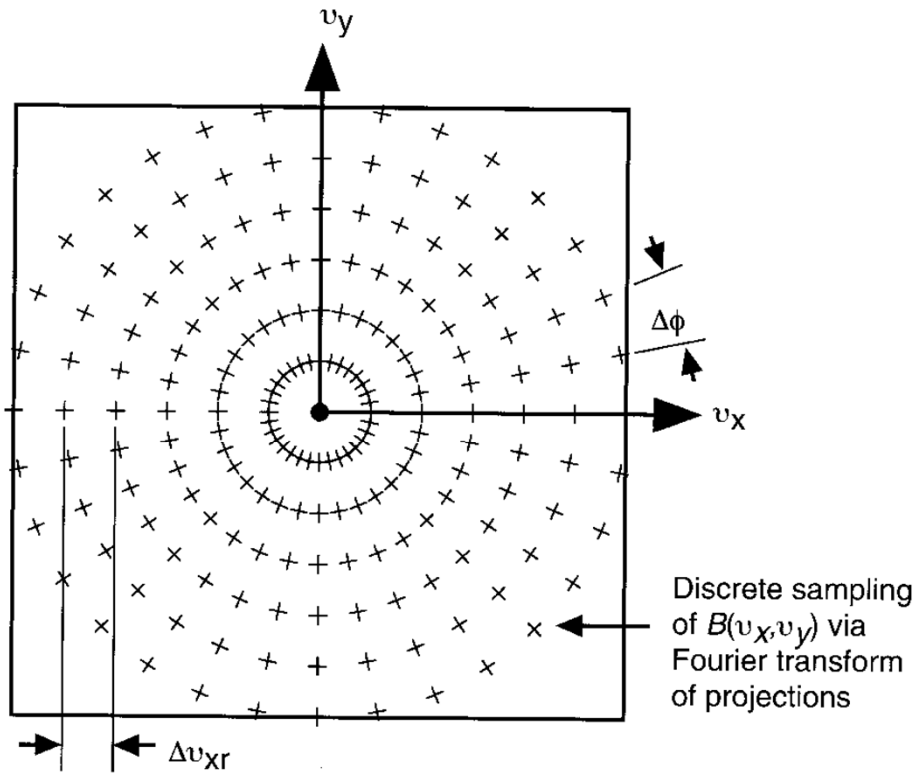

FIGURE 18 The discrete sampling pattern of $F(\upsilon_x,\upsilon_y)$ contained in $B(\upsilon_x,\upsilon_y)$, resulting from the use of discretely sampled projections.

The nature of the 1/r blurring:
Radon transform produced equally spaced radial sampling in Fourier domain.

Simple Backprojection and Inverse Radon Transform

Crude Idea 1: Take each projection and smear it back along the lines of integration it was calculated over.

Result from a back projection from a single view angle:

$$b_\phi(x,y) = \int p_\phi(x') \, \delta(x\cos\phi + y\sin\phi - x') \, dx'$$

Adding up all the back projections from all the angles gives,

$$f_{\text{back-projection}}(x,y) = \int b_\phi(x,y) \, d\phi$$

$$\hat{f}_{\text{simple backprojection}}(x,y) = \int_0^\pi d\phi \int_{-\infty}^{\infty} p_\phi(x') \cdot \delta(x\cos\phi + y\sin\phi - x') dx'$$

$$\hat{f}_{\text{Inverse Radon transform}}(x,y) = \int_0^\pi d\phi \int_{-\infty}^{\infty} F^{-1}\{F[p_\phi(x')] \cdot |w|\} \cdot \delta(x\cos\phi + y\sin\phi - x') dx'$$

Filtered Back-projection

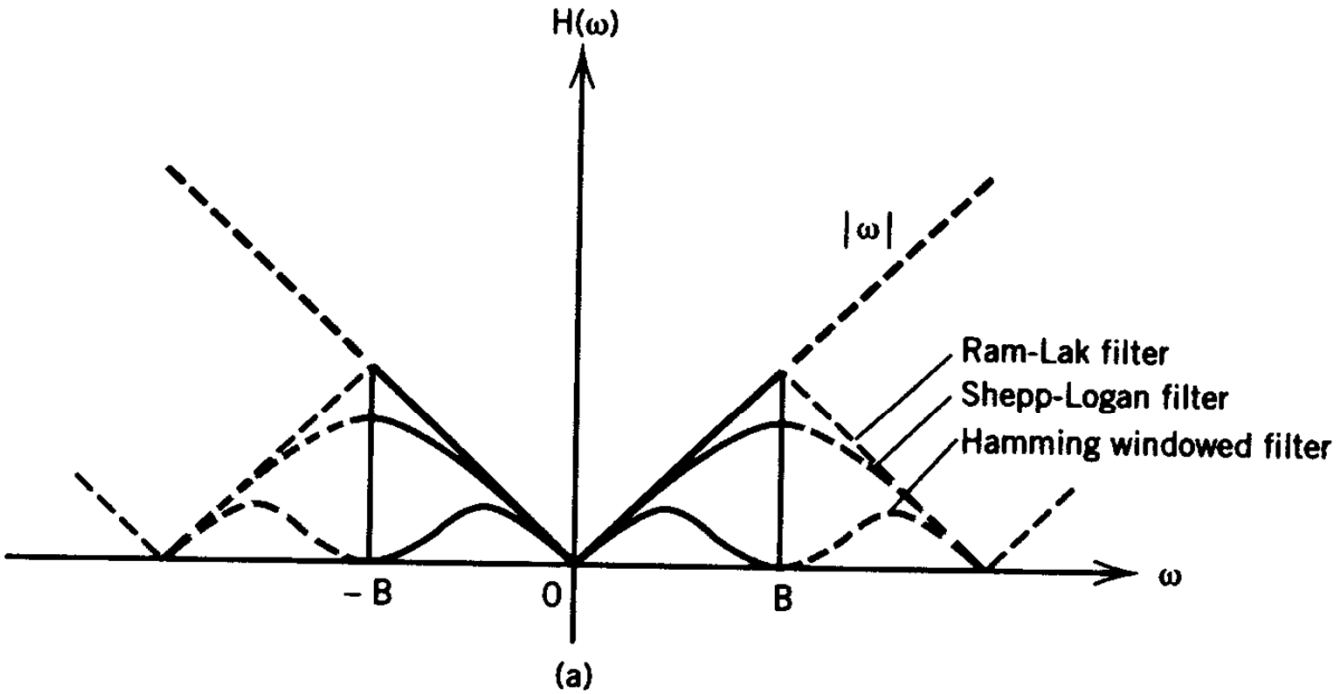

Figure 3-4 (a) Examples of the band-limited filter function of sampled data. Note the cyclic repetitiveness of the digital filter.

Filtered Back-Projection

$$\Delta x = 1/(2B),$$

Sampled version

$$h_{\mathrm{RL}}(0) = B^2 = \frac{1}{4\,\Delta x^2} \qquad (\text{if } k = 0)$$

$$h_{\mathrm{RL}}(k) = 0 \qquad (\text{if } k \text{ even})$$

$$h_{\mathrm{RL}}(k) = \frac{-4B^2}{\pi^2 k^2} = \frac{-1}{\pi^2 k^2 \Delta x^2} \qquad (\text{if } k \text{ odd})$$

$$h_{SL}(k) = \frac{-2}{\pi^2 \Delta x^2 (4k^2 - 1)}$$

$$= \frac{-8B^2}{\pi^2 (4k^2 - 1)}$$

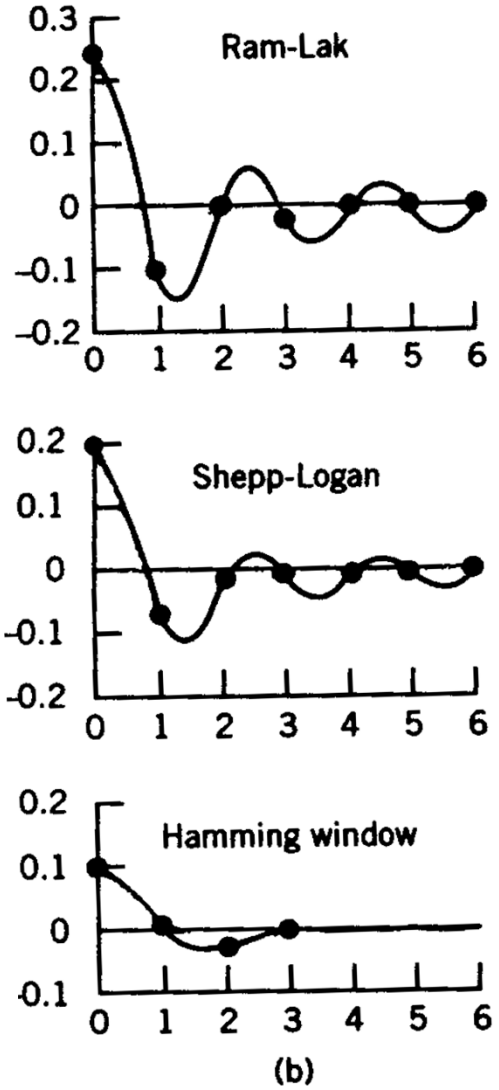

Figure 3-4 (b) Spatial domain filter kernals corresponding to the filter functions shown in the Ram-Lak filter is a high-pass filter with a sharp response but results in some noise enhancement, while the Shepp-Logan and the Hamming window filters are noise-smoothed filters and therefore have better SNR.

Simple Backprojection and Inverse Radon Transform

Result from a back projection from a single view angle:

$$b_\phi(x,y) = \int p_\phi(x') \, \delta(x\cos\phi + y\sin\phi - x') \, dx'$$

Adding up all the back projections from all the angles gives,

$$f_{\text{back-projection}}(x,y) = \int b_\phi(x,y) \, d\phi$$

$$\hat{f}_{\text{simple backprojection}}(x,y) = \int_0^\pi d\phi \int_{-\infty}^{\infty} p_\phi(x') \cdot \delta(x\cos\phi + y\sin\phi - x')dx'$$

$$\hat{f}_{\text{Inverse Radon transform}}(x,y) = \int_0^\pi d\phi \int_{-\infty}^{\infty} F^{-1}\{F[p_\phi(x')] \cdot |w|\} \cdot \delta(x\cos\phi + y\sin\phi - x')dx'$$

$$\hat{f}_{\text{Filtered backprojection}}(x,y) = \int_0^\pi d\phi \int_{-\infty}^{\infty} F^{-1}\{F[p_\phi(x')] \cdot W(w)\} \cdot \delta(x\cos\phi + y\sin\phi - x')dx'$$

Simple and Filtered Back-projection

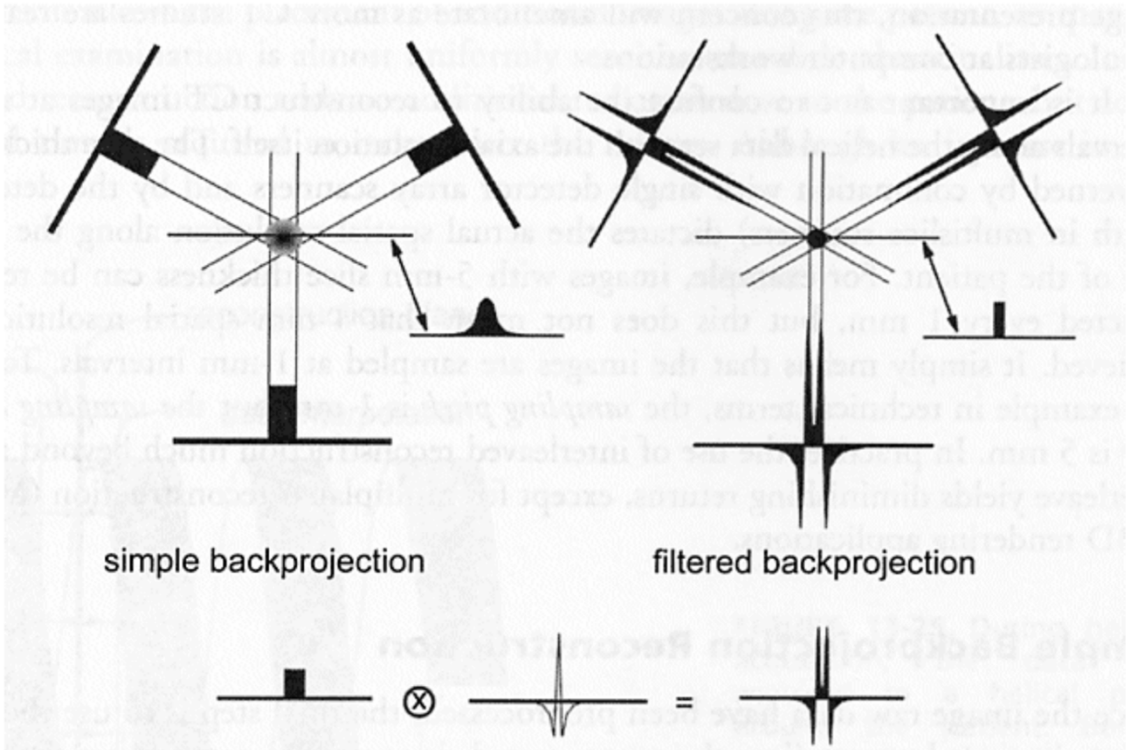

FIGURE 13-28. Simple backprojection is shown on the left; only three views are illustrated, but many views are actually used in computed tomography. A profile through the circular object, derived from simple backprojection, shows a characteristic 1/r blurring. With filtered backprojection, the raw projection data are convolved with a convolution kernel and the resulting projection data are used in the backprojection process. When this approach is used, the profile through the circular object demonstrates the crisp edges of the cylinder, which accurately reflects the object being scanned.

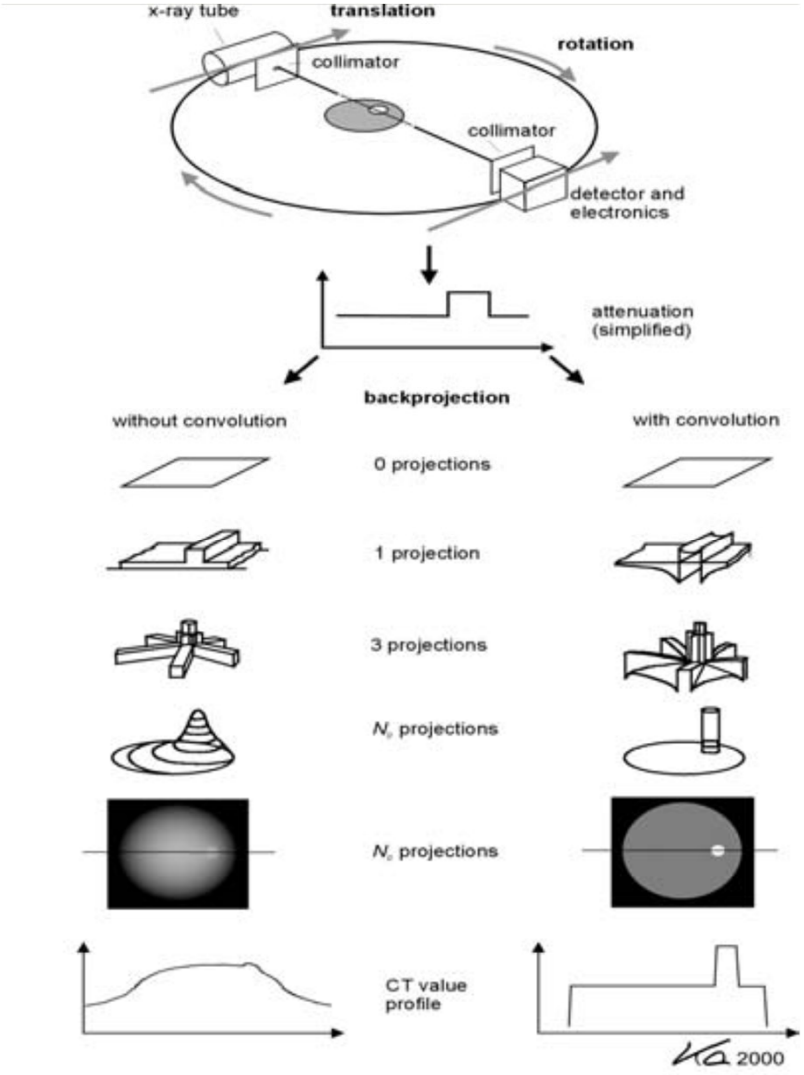

Chapters 12 & 13, The Essential Physics of Medical Imaging, Bushberg

Contrast, Modulation, Modulation Transfer Function and Resolution

Key Performance Measures

There are many important performance parameters for x-ray computed tomography.

The most important parameters are:

- CT number accuracy
- Spatial resolution
- Signal-to-Noise Ratio in CT Images

CT Numbers

CT Number is defined/measured as:

$$h = 1000 \times \frac{\mu - \mu_{water}}{\mu_{water}} (HU), \text{ where the HU is the Houndsfield unit.}$$

CT number → relative attenuation coefficient respect to that of water.

CT number is widely used for quality control purpose, basically,

→ The same object should appear with the same CT number in CT images taken with different scanners.

→ The a uniform object should appear to have homogeneous CT numbers across the entire reconstructed image.

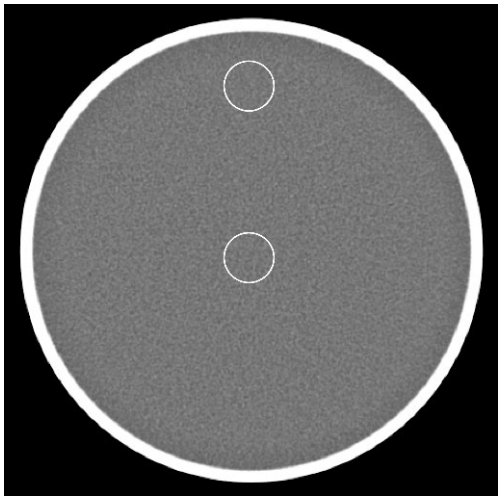

h_{air}=-1000, h_{water}=1 and h_{bone}≅1000.

CT- Resolution – Modulation Transfer Function

- *The modulation m_f is an effective way to quantify the contrast of a periodic signal*

$$m_f = \frac{f_{\max} - f_{\min}}{f_{\max} + f_{\min}}.$$

- *In general, m_f is refer to as the contrast of a periodic signal f(x,y) relative to its average value.*

- *So within two signals, f(x,y) and g(x,y), with the same average value , f(x,y) is said to have more contrast if $m_f > m_g$.*

Modulation

- *Suppose an input signal function*

$$f(x, y) = A + B \sin(2\pi u_0 x) ,$$

where A>B and both are non-negative constants.

$$m_f = \frac{B}{A} .$$

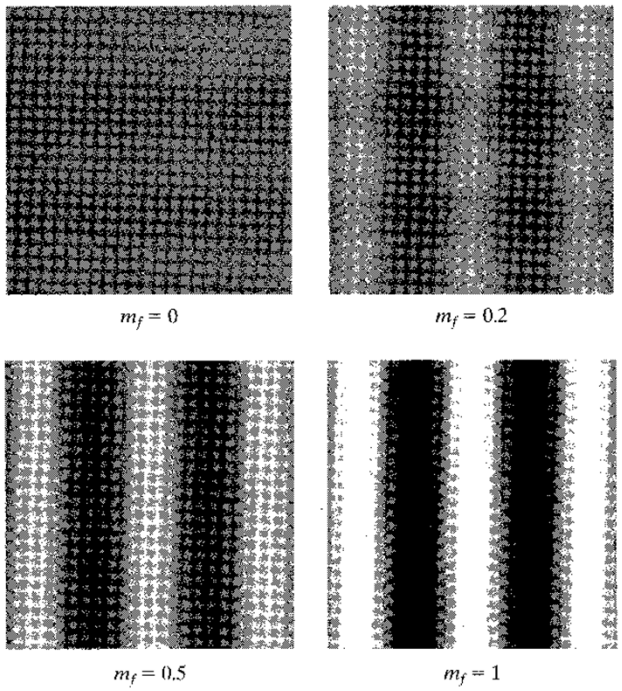

Greater m_f, more contrast

In Plane Spatial Resolution

Resolution of an CT system is measured with the modulation transfer function (MTF):

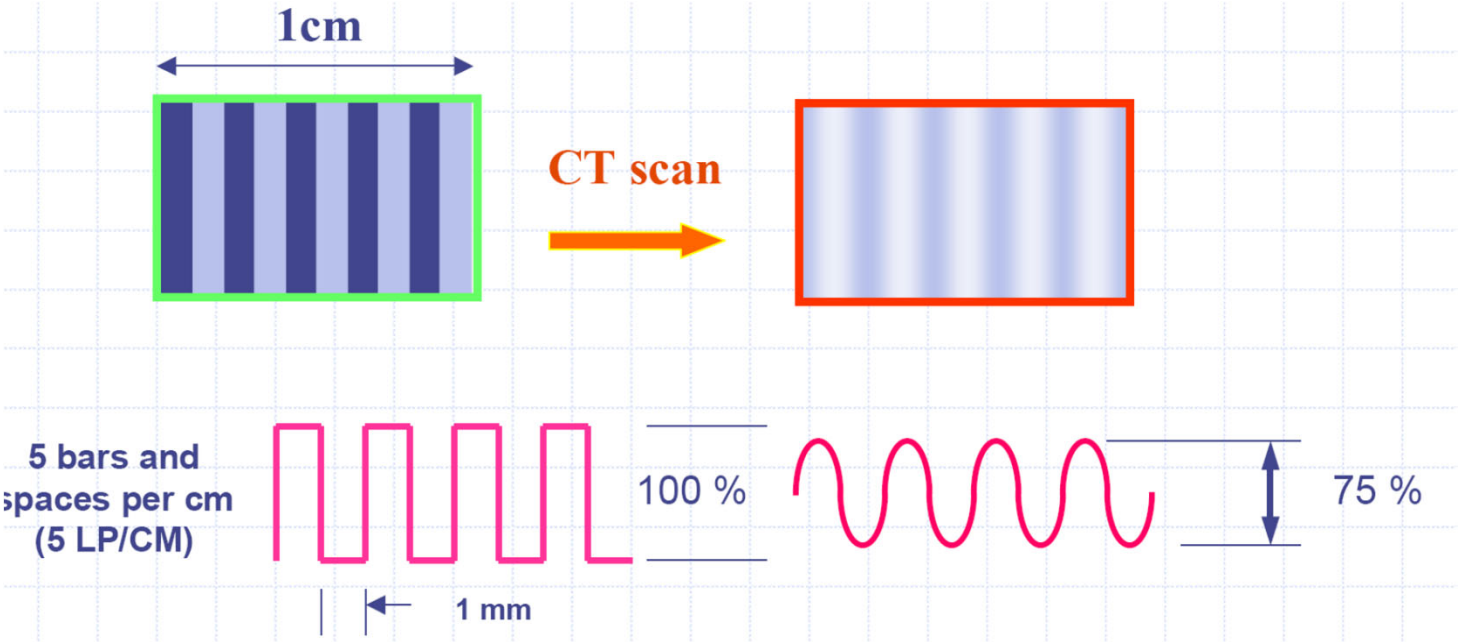

CT number → relative attenuation coefficient respect to that of water.

In Plane Spatial Resolution

Resolution of an CT system is measured with the modulation transfer function (MTF):

$$\mathrm{MTF}(u,v) = \frac{m_g}{m_f} = \frac{|H(u,v)|}{H(0,0)},$$

- *A typical MTF of an imaging system*

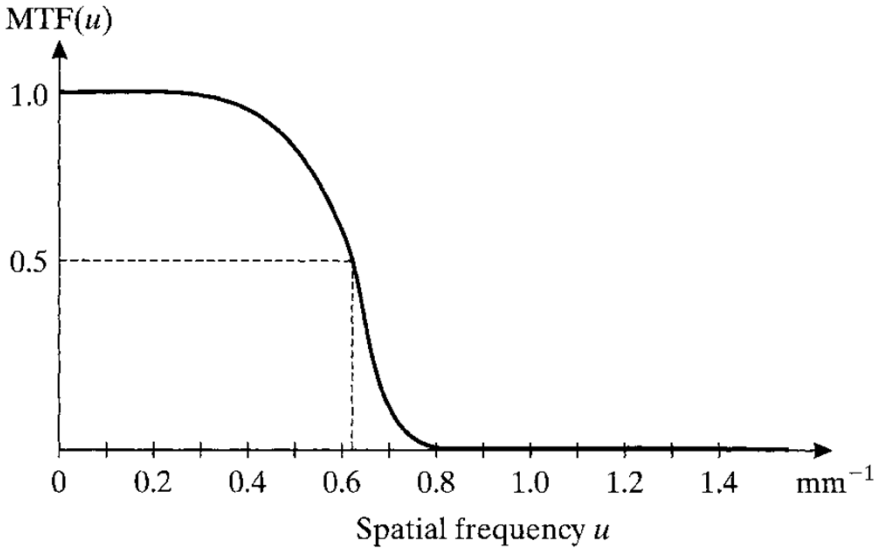

Figure 3.3
A typical MTF of a medical imaging system.

LSF and MTF

- *Modulation Transfer Function (MTF).*

$$\mathrm{MTF}(u) = \frac{m_g}{m_f} = \frac{|H(u,0)|}{H(0,0)} = \frac{|L(u)|}{L(0)}, \qquad \text{for every } u.$$

- *For a "reasonable" imaging system, the L(0)=1, so that*

$$\mathrm{MTF}(u) = L(u)$$

- *MTF is an effective way to compare two imaging systems in terms of spatial resolution and contrast.*

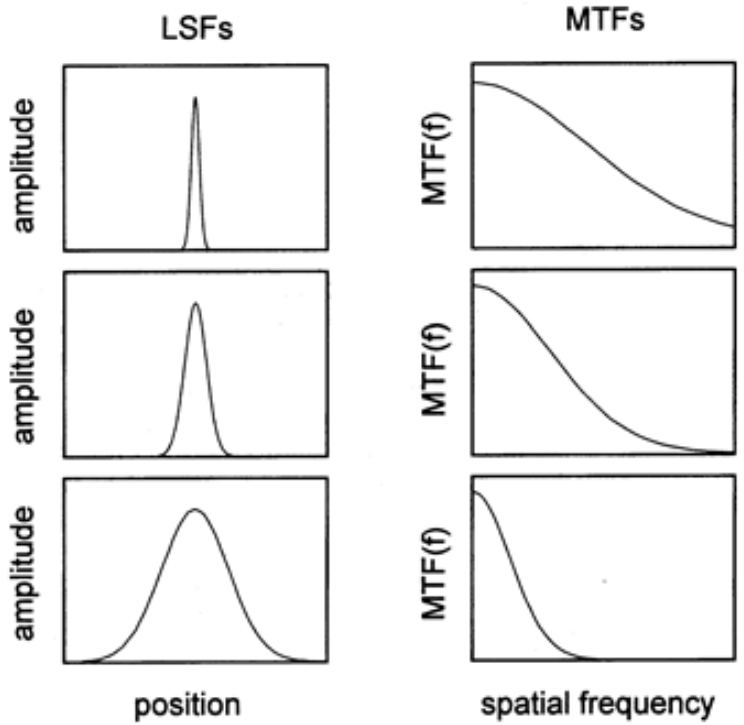

$$\begin{aligned} g(x,y) &= \int_{-\infty}^{\infty}\int_{-\infty}^{\infty} h(\xi,\eta) f(x-\xi, y-\eta)\, d\xi\, d\eta, \\ &= \int_{-\infty}^{\infty}\left[\int_{-\infty}^{\infty} h(\xi,\eta)\delta(x-\xi)\, d\xi\right] d\eta, \\ &= \int_{-\infty}^{\infty} h(x,\eta)\, d\eta, \quad \equiv l(x), \quad L(\omega) = \mathcal{F}_{1D}[l(x)] \end{aligned}$$

SNR in CT Images

SNR in Projection Data

Suppose a first generation CT system that consists N linear scanning steps and M angular scanning steps. Given an X-ray beam intensity N_0 from the source, the average measured intensity is

$$N_i = N_o\, e^{-\int \mu\, dz}$$

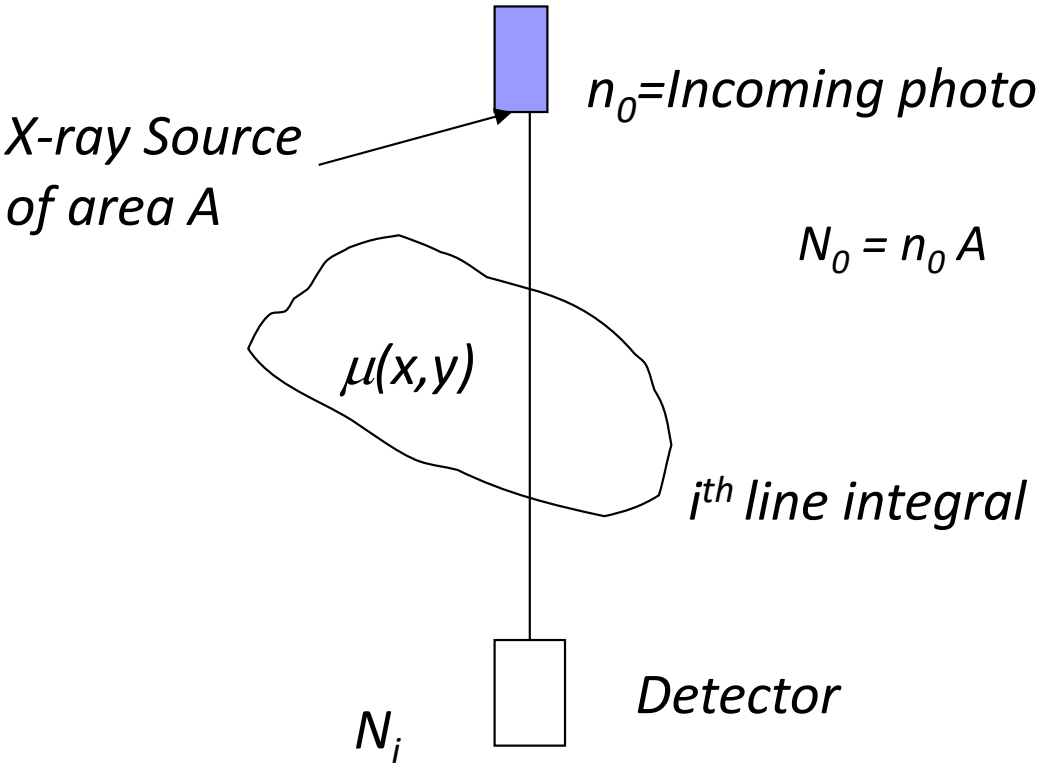

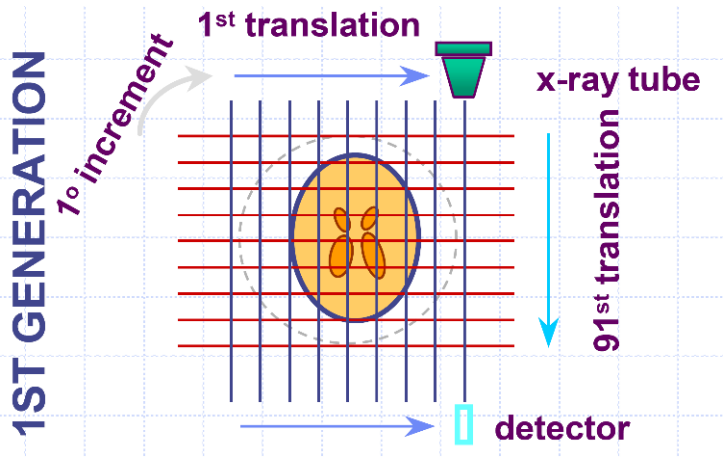

Error Propagation

In some situations, the variable of interest (Q) is not measured directly, but derived as a function of more than one independent random variable whose values are directly measured. The error on the measured values is propagated into the uncertainty on the resultant quantity Q.

Suppose a quantity Q(x,y) that depends on two independent random variables x and y.

The sample mean and variance of variables x and y are derived as σ_x and σ_y, by repeating measurements.

The standard deviation of the indirect quantity Q is approximately given by

$$\sigma_Q^{\,2} \cong \left(\frac{\partial Q}{\partial x}\right)^2 \sigma_x^{\,2} + \left(\frac{\partial Q}{\partial y}\right)^2 \sigma_y^{\,2}$$

$$\sigma_Q^{\,2} \cong \sum_i \left(\frac{\partial Q}{\partial x_i}\right)^2 \sigma_{x_i}^{\,2}$$

SNR in Projection Data

Let $N_i = n_0 A \exp \int_i -\mu\, dl = N_0 \exp \int_i -\mu\, dl$ where A is area of detector and $N_0 = n_0 A$ is the average number of x-ray photons emitting from the source and traveling towards the detector

The basic measured CT measure is

Integral attenuation along a line of response

$$g_{ij} = \int \mu\, dl = -\ln (N_{ij}/N_0)$$

No. of photons collected by detector i and at projection angle j.

Noting that the N_{ij} is a Poisson random number, so

$$Mean(g_{ij}) = \mu \approx -\ln (N_{ij}/N_0)$$

$$Var(g_{ij}) \approx 1/Mean(N_{ij})$$

SNR in Projection Data

Noting that the N_{ij} *is a Poisson random number, so*

$$Mean(g_{ij}) = \mu \approx -\ln (N_{ij}/N_0)$$

$$Var(g_{ij}) \approx 1/Mean(N_{ij})$$

The projection data is used in the Filtered back-projection process for reconstruction, lets see how the noise in the projection data is propagated through this process

$$SNR = C\ \mu / \sigma(\mu) ???$$

Filtered Backprojection

Remember that the inverse Radon transform is defined as

$$f(x,y) = \mathcal{R}^{-1}\left[f(x,y)\right] = \frac{1}{\pi}\int_0^{\pi} d\phi \int_{-\infty}^{\infty} |\omega| P_\phi(\omega) e^{j2\pi w x'} d\omega \quad (1)$$

It (in principle) reproduces the original function f(x,y).

Compare the inverse Radon transform (above) with the Filtered back-projection operation (below)

$$\hat{f}(x,y) = \frac{1}{\pi}\int_0^{\pi} d\phi \int_{-\infty}^{\infty} |\omega| W(\omega) P_\phi(\omega) e^{j2\pi w x'} d\omega \quad (2)$$

$$where \;\; x' = x\cos\phi + y\sin\phi$$

Discrete Filtered Backprojection

$$\hat{f}(x,y) = \frac{1}{\pi}\int_0^{\pi} d\phi \int_{-\infty}^{\infty} |\omega| W(\omega) P_\phi(\omega) e^{j2\pi w x'} d\omega$$

$$\hat{f}(x,y) = \frac{1}{\pi}\int_0^{\pi} d\phi \int_{-\infty}^{\infty} dx'\, p_\phi(x') h(x\cos\phi + y\sin\phi - x')$$

c(·) is the discretized version of the filter function w(x'), whose FT is $|\omega|W(\omega)$

$$\hat{f}(x,y) = \sum_{j=1}^{M}\left[\sum_{i=-N/2}^{N/2} g_{ij} c(x\cos\phi_j + y\sin\phi_j - iT)\cdot T\right]\Delta\phi$$

$$= \frac{\pi T}{M}\sum_{j=1}^{M}\sum_{i=-N/2}^{N/2} g_{ij} c(x\cos\phi_j + y\sin\phi_j - iT)$$

M: # of projections taken from 0→π

T: Physical spacing between detectors

Discrete Filtered Backprojection

Note that this equation is a linear function of the projection data g_{ij}.

Therefore, the mean of the estimated attenuation coefficient at a given location (x,y) is simply

$$mean\left[\hat{\mu}(x,y)\right] = \frac{\pi T}{M}\sum_{j=1}^{M}\sum_{i=-N/2}^{N/2}\bar{g}_{ij}\,c(x\cos\phi_j + y\sin\phi_j - iT)$$

Substituting g_{ij} with its mean

Discrete Filtered Backprojection

Now, let's consider the variance on the estimated attenuation coefficients.

The first thing to notice is that all measured data g_{ij} are assumed to be independent Poisson variables and c(·) terms are deterministic. So the above mentioned estimation process is essentially the sum of multiple independent random variables

$$\hat{\mu}(x,y) = \frac{\pi T}{M} \sum_{j=1}^{M} \sum_{i=-N/2}^{N/2} \overline{g}_{ij} c(x\cos\phi_j + y\sin\phi_j - iT)$$

The variance on the sum of a number of discrete random variables are the sum of individual variables

Discrete Filtered Backprojection

Note that

1. *The variance of the sum of independent random variables is the sum of individual variances for each variables.*

$$Var\left[\sum x_i\right] = \sum Var\left[x_i\right], \quad \text{when } x_i\text{s are independent.}$$

2. *The variance of a random variable multiplied by a constant is the variance of the random variable times the square of the constant*

$$Var\left[ax\right] = a^2 Var\left[x\right]$$

So

$$Var\left[\hat{\mu}(x,y)\right] = Var\left[\frac{\pi T}{M}\sum_{j=1}^{M}\sum_{i=-N/2}^{N/2}\bar{g}_{ij}\,c(x\cos\phi_j + y\sin\phi_j - iT)\right]$$

$$= \left(\frac{\pi T}{M}\right)^2 \sum_{j=1}^{M}\sum_{i=-N/2}^{N/2} Var(g_{ij})\cdot\left[c(x\cos\phi_j + y\sin\phi_j - iT)\right]^2$$

Discrete Filtered Backprojection

Remember that

$$Mean(g_{ij}) = \mu \approx -\ln (N_{ij}/N_0)$$

$$Var(g_{ij}) \approx 1/Mean(N_{ij})$$

So

$$Var\left[\hat{\mu}(x,y)\right] = \left(\frac{\pi T}{M}\right)^2 \sum_{j=1}^{M} \sum_{i=-N/2}^{N/2} \frac{1}{\overline{N}_{ij}} \cdot \left[c(x\cos\phi_j + y\sin\phi_j - iT)\right]^2$$

To proceed, we assume that the object, we make a bad assumption

$$\overline{N}_{ij} = \overline{N}$$

This is clearly wrong mathematically, since most of objects do not satisfy this assumption. But in practice, this is valid since one is interested in local variation of the attenuation of the object …

Discrete Filtered Backprojection

With this assumption, we get

$$Var\left[\hat{\mu}(x,y)\right] = \left(\frac{\pi T}{M}\right)^2 \frac{1}{\overline{N}} \sum_{j=1}^{M} \sum_{i=-N/2}^{N/2} \left[c(x\cos\phi_j + y\sin\phi_j - iT)\right]^2$$

$$= \frac{\pi T}{M} \frac{1}{\overline{N}} \sum_{j=1}^{M} \left\{ \sum_{i=-N/2}^{N/2} \left[c(x\cos\phi_j + y\sin\phi_j - iT)\right]^2 T \right\} \Delta\phi$$

$$= \frac{\pi T}{M} \frac{1}{\overline{N}} \int_0^{\pi} d\phi \int_{-\infty}^{\infty} \left[c(x\cos\phi_j + y\sin\phi_j - x')\right]^2 dx'$$

$$= \frac{\pi T}{M} \frac{1}{\overline{N}} \int_0^{\pi} d\phi \int_{-\infty}^{\infty} \left[c(x')\right]^2 dx' = \frac{\pi^2 T}{M} \frac{1}{\overline{N}} \int_{-\infty}^{\infty} \left[c(x')\right]^2 dx'$$

Using the Parseval's theorem

$$\int_{-\infty}^{\infty} \int_{-\infty}^{\infty} |f(x,y)|^2 \, dxdy = \int_{-\infty}^{\infty} \int_{-\infty}^{\infty} |F(u,v)|^2 \, dudv$$

Image Variance with Filtered Backprojection

We have

$$Var\left[\hat{\mu}(x,y)\right] = \frac{\pi T}{M}\frac{1}{\overline{N}}\int_0^{\pi} d\phi \int_{-\infty}^{\infty}\left[c(x\cos\phi_j + y\sin\phi_j - x')\right]^2 dx'$$

$$= \frac{\pi T}{M}\frac{1}{\overline{N}}\pi\int_{-\infty}^{\infty}\left[c(x\cos\phi_j + y\sin\phi_j - x')\right]^2 dx'$$

$$= \frac{\pi T}{M}\frac{1}{\overline{N}}\pi\int_{-\infty}^{\infty}\left[C(\omega)\right]^2 d\omega$$

Remember that

$$\hat{f}(x,y) = \frac{1}{\pi}\int_0^{\pi} d\phi \int_{-\infty}^{\infty} |\omega| W(\omega) P_{\phi}(\omega) e^{j2\pi w x'} d\omega$$

and

$$C(\omega) = |\omega| W(\omega)$$

We can now derive the variance in image (attenuation function) for given filter functions …

Image Variance with Filtered Backprojection

For a Ram-Lak filter function

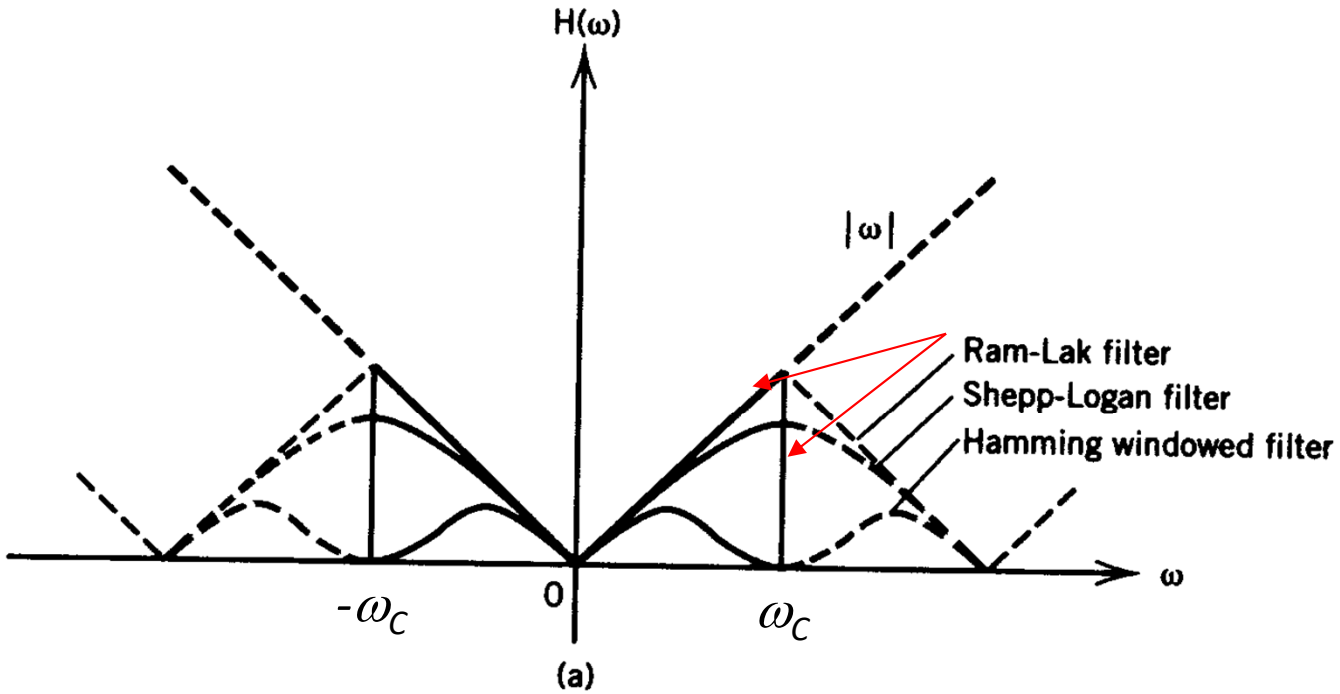

Figure 3-4 (a) Examples of the band-limited filter function of sampled data. Note the cyclic repetitiveness of the digital filter.

$$W_{RL} = \begin{cases} |\omega|, & |\omega| < \omega_C \\ 0, & \text{otherwise} \end{cases}$$

Image Variance with Filtered Backprojection

We have

$$Var\left[\hat{\mu}(x,y)\right] = \frac{\pi T}{M}\frac{1}{\overline{N}}\pi\int_{-\infty}^{\infty}\left[C(\omega)\right]^2 d\omega$$

$$= \frac{\pi T}{M}\frac{1}{\overline{N}}\pi\int_{-\omega_C}^{\omega_C}|\omega|^2\, d\omega$$

$$= \frac{1}{M}\frac{1}{\overline{N}/T}\frac{2\pi^2}{3}\omega_C^3$$

Cutoff frequency

Number of angular samplings

Detector width

No. of counts per detector of width T

Let's see how things folded together …

Image Variance with Filtered Backprojection

$$Var\left[\hat{\mu}(x,y)\right] = \frac{1}{M}\frac{1}{\overline{N}/T}\frac{2\pi^2}{3}\omega_c^3$$

Number of angular samplings

No. of counts per detector of width T

Detector width

Cutoff frequency

1. $\overline{1}/M$: increasing the number of angular sampling always reduce noise.
2. N/T term: Proportional to the X-ray flux reaching the detector or the dose delivered.
3. ω^3 term: accepting higher frequencies imaging features always increase noise.

SNR with Filtered Backprojection

$$Mean\left[\hat{\mu}(x,y)\right] = \frac{\pi T}{M}\sum_{j=1}^{M}\sum_{i=-N/2}^{N/2}\bar{g}_{ij}c(x\cos\phi_j + y\sin\phi_j - iT)$$

$$Var\left[\hat{\mu}(x,y)\right] = \left(\frac{\pi T}{M}\right)^2\sum_{j=1}^{M}\sum_{i=-N/2}^{N/2}\frac{1}{\bar{N}_{ij}}\cdot\left[c(x\cos\phi_j + y\sin\phi_j - iT)\right]^2$$

$$\approx \frac{\pi^2 T}{M}\frac{1}{\bar{N}}\int_{-\infty}^{\infty}\left[C(\omega)\right]^2 d\omega$$

So the SNR for CT image reconstructed using Ram-Lak filter is

$$SNR\left[\hat{\mu}(x,y)\right] = C\frac{\bar{\mu}}{\sigma(\mu)} = \frac{C\bar{\mu}}{\pi}\omega_C^{-3/2}\sqrt{\frac{3}{2}(\bar{N}/T)M}$$

SNR with Filtered Backprojection

In reality, there is no point of setting the cutoff frequency higher than the highest frequency contained in the data.

Suppose, the detector width is d, the cutoff frequency is normally $\omega_c \cong k/d$, and $k \cong 1$. In this case the SNR is

$$SNR[\hat{\mu}(x,y)] \approx \frac{C\bar{\mu}}{\pi}\omega_c^{-3/2}\sqrt{\frac{3}{2}(\bar{N}/T)M} \approx 0.4C\bar{\mu}d\sqrt{\bar{N}M}$$

$$\text{where } \bar{\mu}(x,y) = \frac{\pi T}{M}\sum_{j=1}^{M}\sum_{i=-N/2}^{N/2}\bar{g}_{ij}c(x\cos\phi_j + y\sin\phi_j - iT)$$

So, want a better image,

- *Higher dose (if possible)*
- *More angular sampling*
- *Largest detector pixel size (as long as sufficiently fine in respect to the feature to be resolved)*

SNR and Radiation Dose

$$SNR\left[\hat{\mu}(x,y)\right] \approx \frac{C\bar{\mu}}{\pi}\omega_c^{-3/2}\sqrt{\frac{3}{2}(\bar{N}/T)M} \approx 0.4C\bar{\mu}d\sqrt{\bar{N}M}$$

This terms here is proportional to the total radiation dose delivered to the center of the object. Consider the finite thickness (ΔZ) of the slice,

$$Dose(0,0) \propto \left(\frac{SNR\left[\hat{\mu}(x,y)\right]}{\bar{\mu}}\right)^2 \frac{1}{\Delta Z}\omega_c^3$$

SNR and Radiation Dose

$$Dose(0,0) \propto \left(\frac{SNR\left[\hat{\mu}(x,y)\right]}{\bar{\mu}} \right)^2 \frac{1}{\Delta Z} \omega_c^3$$

Normally, the cutoff frequency (ω_C) is

$$\omega_c \approx \frac{1}{2r}$$

The "spatial resolution" required in the image

To maintain a isotropic resolution, one would also reconstructed the image with a thickness comparable to the resolution achieved in-plane, therefore,

$$Dose(0,0) \propto \left(\frac{SNR\left[\hat{\mu}(x,y)\right]}{\bar{\mu}} \right)^2 \frac{1}{r^4}$$

To improve the spatial resolution by a factor of 2, one would need to increase the dose by a factor of 16!!

Chapter 4: Single Photon Emission Computed Tomography (SPECT)

The Tracer Principle

The Tracer Principle

What is the tracer principle?

- Appropriately chosen radioactive compounds participate in an organism's physiological processes in the same way as non-radioactive materials.
- These compounds can be detected through the detecting of their radiation signatures, such as gamma rays.

Two major attributes

- Because one can detect even minute quantities of radioactive material, the tracer principle can be used to measure molecular concentrations with a **tremendous sensitivity**.
- Tracer measurements are **noninvasive** – the concentration of tracer is deduced from the number of gamma rays detected.

Emission Tomography

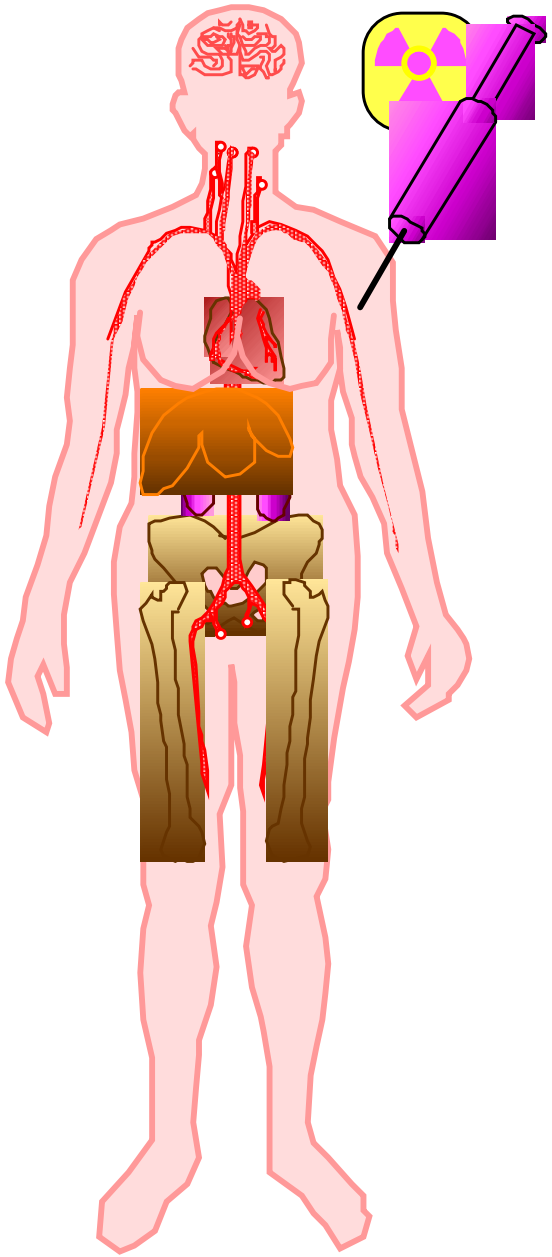

- ***Drug is labeled with radioisotopes that emit gamma rays.***
- ***Drug localizes in patient according to metabolic properties of that drug.***
- ***Trace (pico-molar) quantities of drug are sufficient.***
- ***Radiation dose fairly small (<1 rem).***

Drug Distributes in Body

Tc-99m for Nuclear Medicine

The Basic Aspects:

- *99mTc (IT,γ) 99Tc - 6 hr half life (from 99Mo)*
- *Reactor produced ($^{235}U+^{1}n \rightarrow ^{137}Cs+^{99}Mo$)*
- *γ emission at 140 keV - ideal*
- *6 hr half life - ideal*
- *Readily available from a Generator*
- *90% of all nuclear medicine studies use 99mTc*

Anger Camera

Conventional Anger Camera

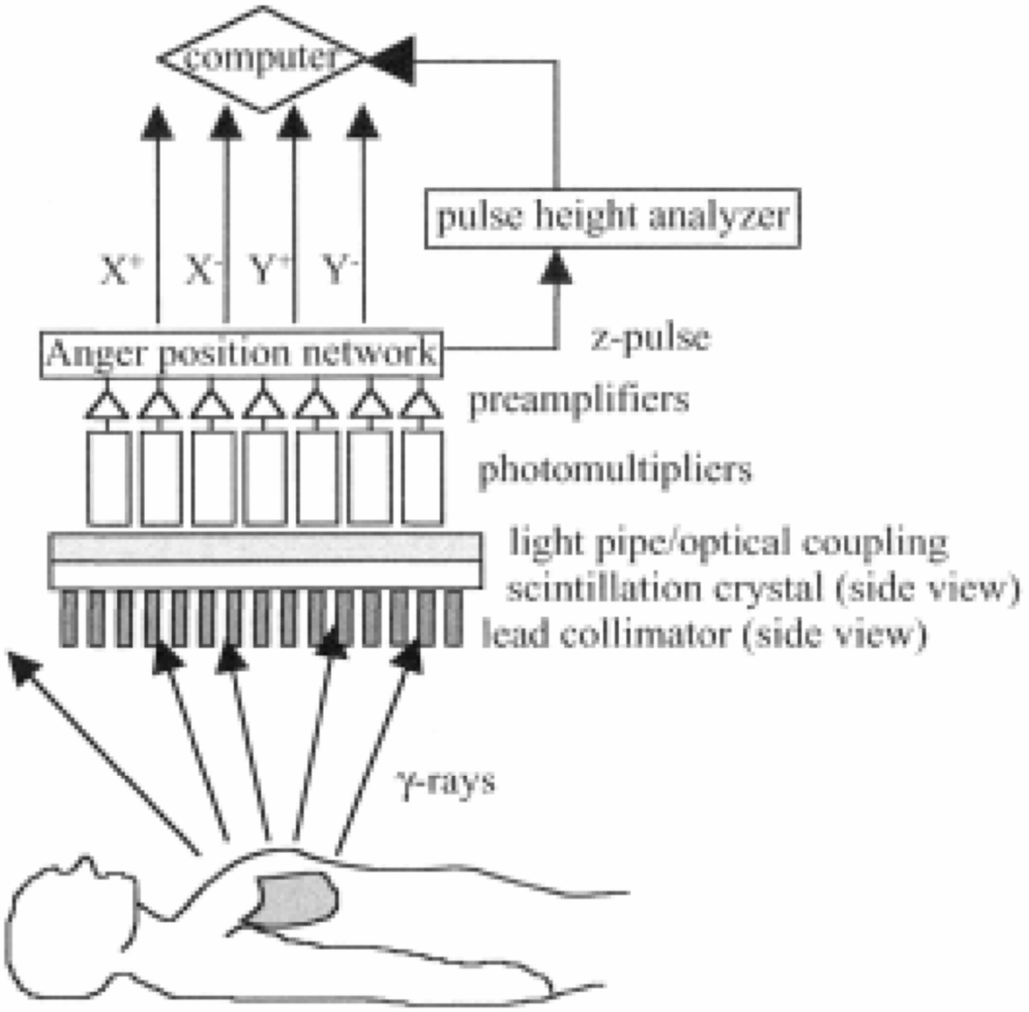

FIGURE 2.4. *Schematic diagram of a gamma camera positioned above the patient. The distribution of the radiopharmaceutical is indicated by the shaded region within the body.*

Conventional Anger Camera

- *PMTs coupled to large, continuous NaI(Tl) crystal*
- *Spatial resolution 3–4 mm FWHM*
- *Energy resolution 8–10% FWHM*
- *Mature technology (DoB ~1957)*
- *Large-area, >40cm x 40cm typical*
- *Simple and cost-effective*

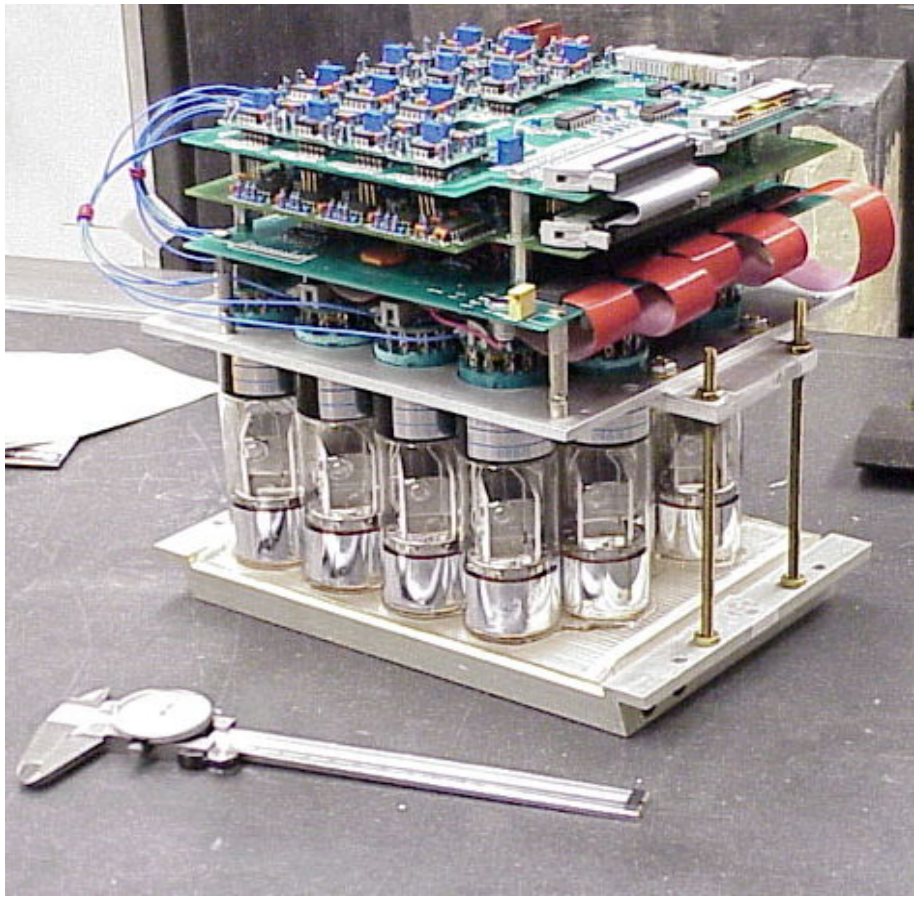

SPRINT II camera module

Scintillation Light

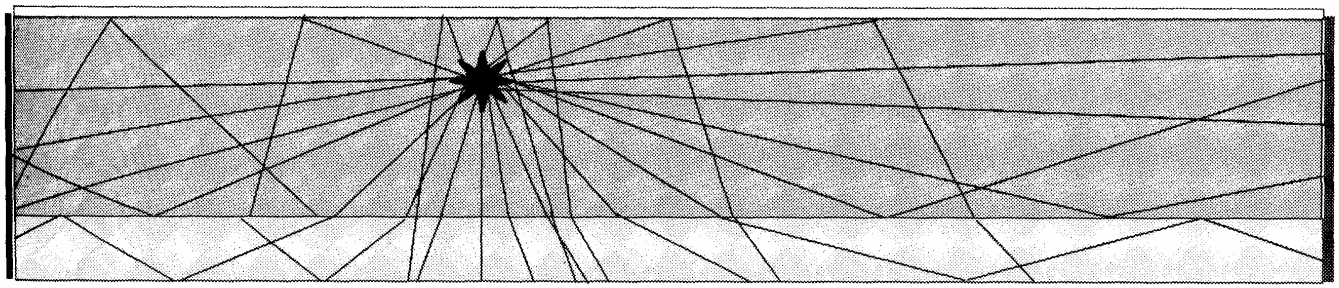

FIGURE 4 Representation of light ray propagation from a point source of light within a scintillation crystal slab with a white diffuse Lambertian reflector on top, absorbing sides, and a light diffuser on the bottom leading into the photodetector.

- *Scintillation light are generated isotropically.*
- *It is difficult to control light propagation inside a continuous bulk scintillator*
- *Light spreading leads to loss in both spatial resolution and energy resolution.*
- *Normally, the best we can do is to provide a better boundary condition for a better light collection efficiency.*

Image Formation in SPECT

Electronic Collimation

Why electronic collimation?

Each detector element is allowed to see greater source volume → high sensitivity

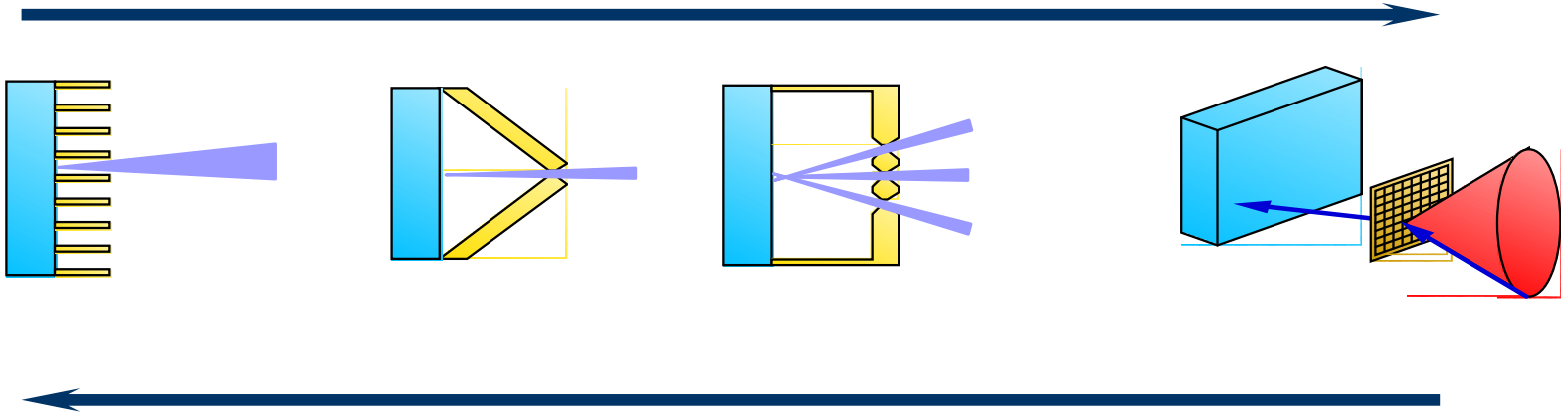

Information content per detected photon is decreasing → the benefit depends on the particular source.

How to Improve the Tradeoff between Spatial Resolution and Sensitivity?

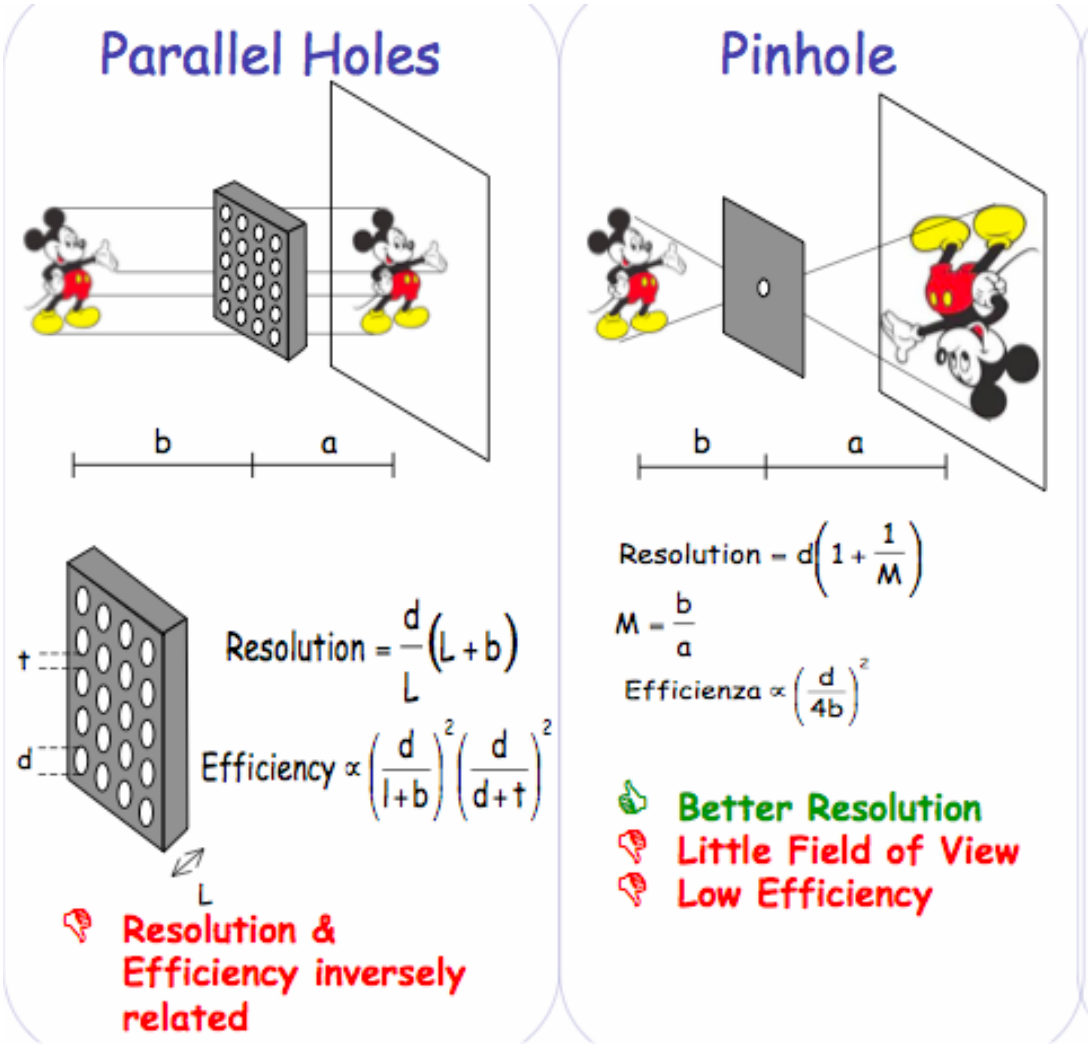

Better resolution →

- *smaller hole diameter,*
- *better detector intrinsic resolution,*
- *smaller source to object distance.*

Better sensitivity → Larger hole diameter

Compton Scattering and Compton Camera

Energy Transfer in Compton Scattering

If we assuming the electron is free and at rest, the scattered gamma ray has an energy

Initial photon energy, v: photon frequency,

h= 6.757704 meter ·kilogram/second, (Planck's constant)

$$h\nu' = \frac{h\nu}{1 + \frac{h\nu}{m_0 c^2}(1 - \cos(\theta))},$$

mass of electron *Scattering angle*

and the photon transfers part of its energy to the electron (assumed to be at rest), which is known as a ***recoil electron****. Its energy is simply*

$$E_{recoil} = h\nu - h\nu' = h\nu - \frac{h\nu}{1 + \frac{h\nu}{m_0 c^2}(1 - \cos(\theta))}$$

The one-to-one relationship between scattering angle and energy loss!!

Reading: Page 51, Radiation Detection and Measurements, Third Edition, G. F. Knoll, John Wiley & Sons, 1999.

Electronic Collimation
Compton Camera

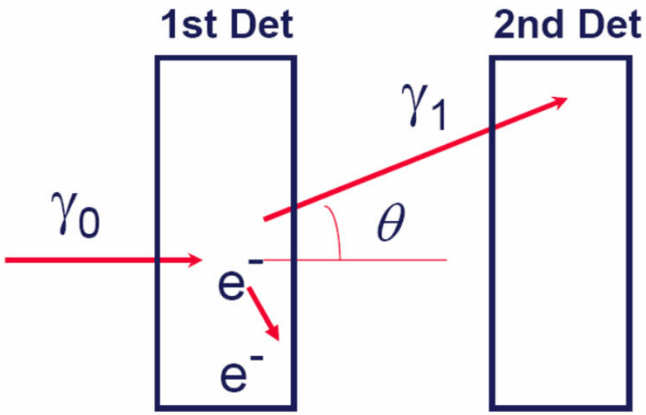

$$\frac{1}{E_1} - \frac{1}{E_0} = \frac{1}{511\text{keV}}(1-\cos\theta)$$

E_0: incident photon energy
E_1: scattered photon energy
θ : scattering angle

1st det: solid state detector
2nd det: scintillation detector

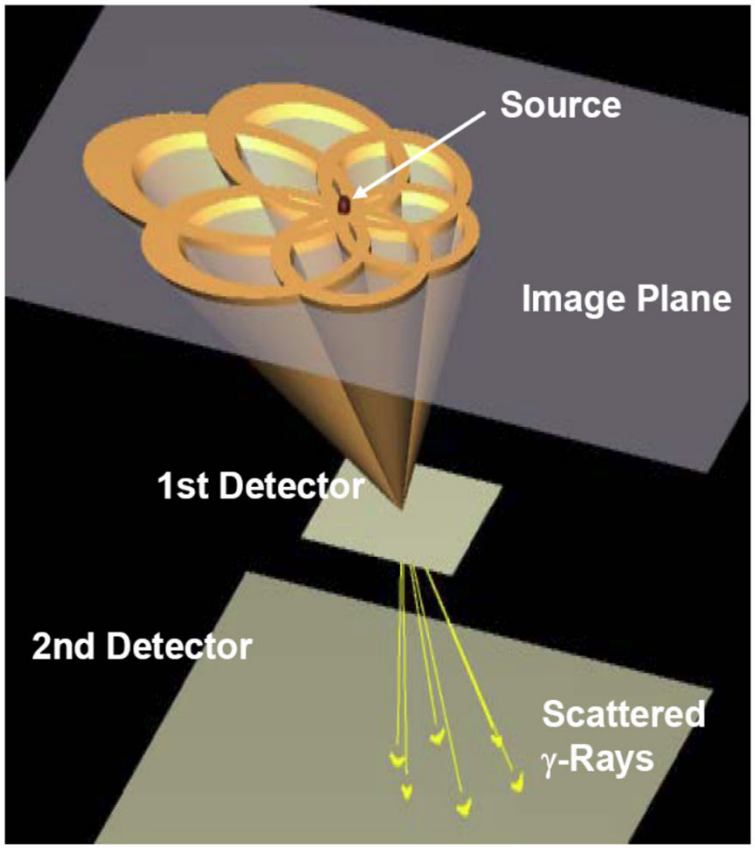

Courtesy of Neal Clinthorne, U. Michigan.

Fundamentals of Positron Emission Tomography (PET)

Basic Image Formation Process

Annihilation Radiation following Positron Emission

Beta - plus decay or positron decay :

$$ {}^{A}_{Z}X \rightarrow {}^{A}_{Z-1}Y + {}^{0}_{1}\beta + \upsilon $$

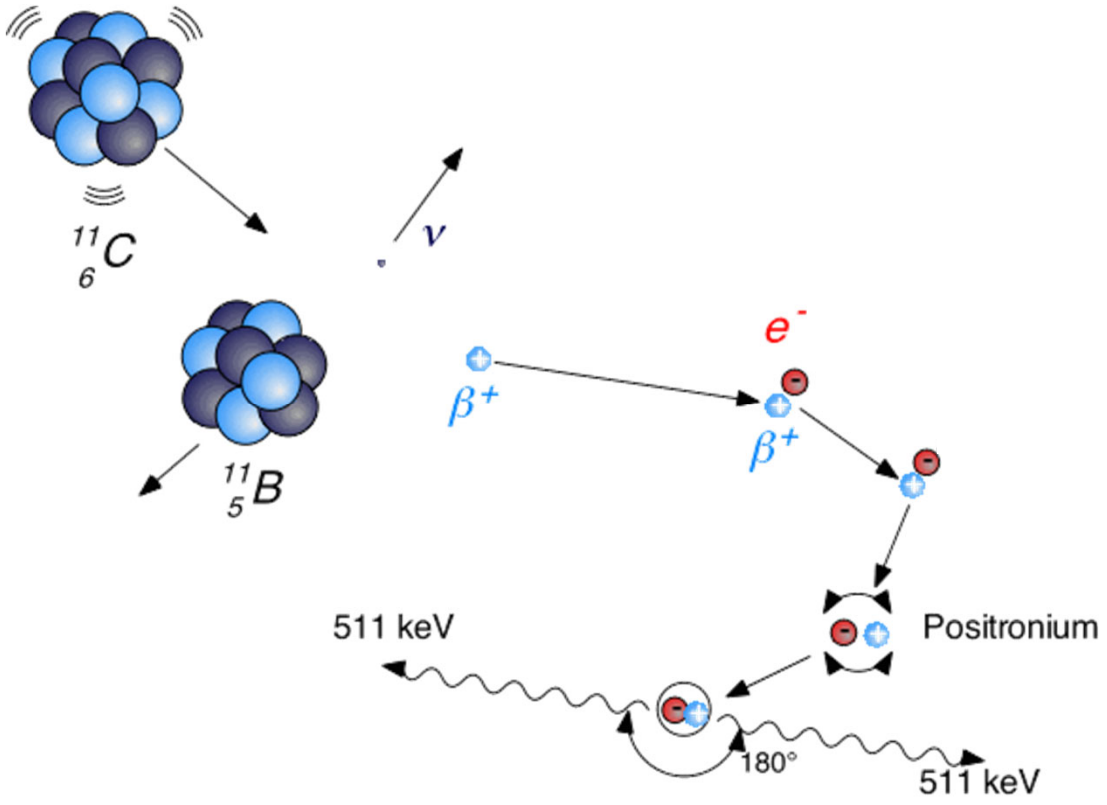

The Tracer Principle Again

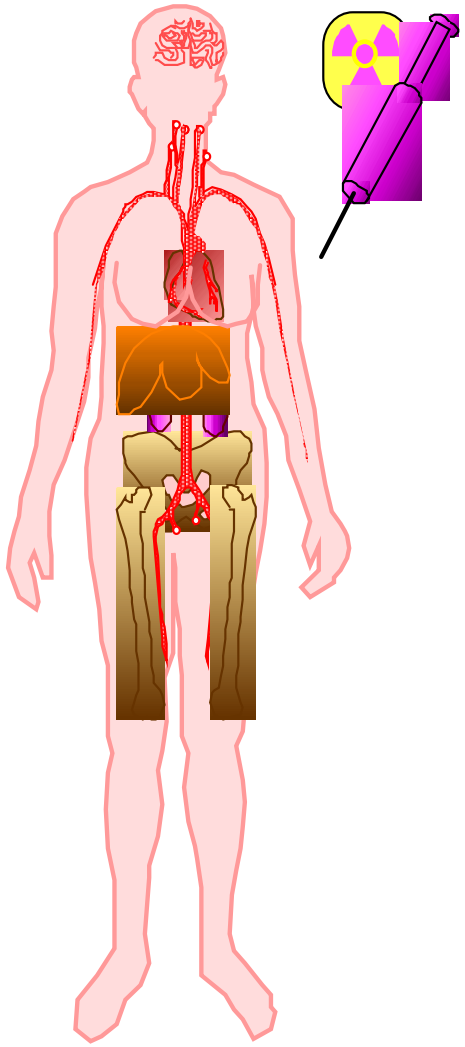

- *Drug is labeled with positron (β^+, anti-particle of an electron) emitting radionuclide.*
- *Drug localizes in patient according to metabolic properties of that drug.*
- *Trace (pico-molar) quantities of drug are sufficient.*
- *Radiation dose fairly small (<1 rem).*

Detect Radioactive Decays

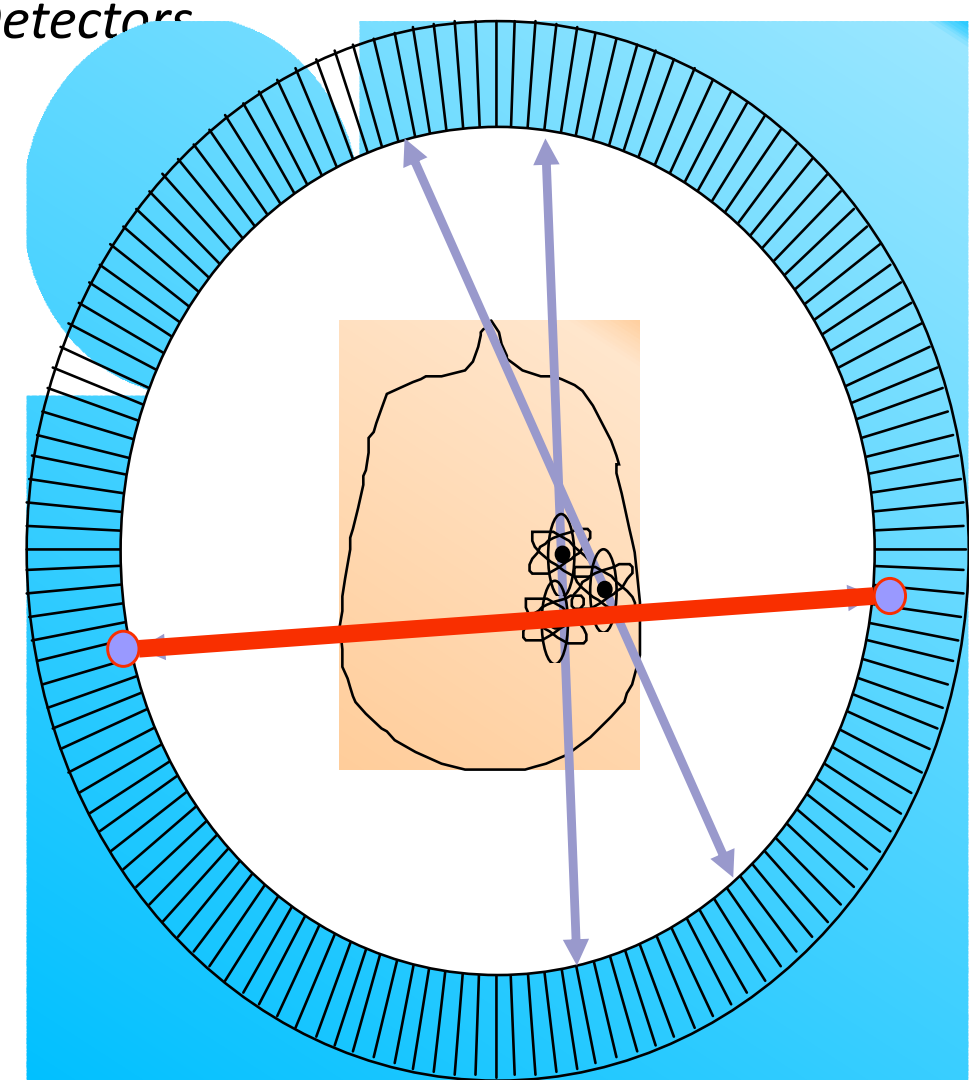

- Radionuclide decays, emitting β^+.
- β^+ annihilates with e^- from tissue, forming back-to-back 511 keV photon pair.
- 511 keV photon pairs detected via time coincidence.
- Positron lies on line defined by detector pair (known as a chord or a line of response or a LOR).

Detect Pair of Back-to Back 511 keV Photons

PET data acquisition

- Organization of data
  - True counts in LORs are accumulated
  - In some cases, groups of nearby LORs are grouped into one average LOR (“mashing”)
  - LORs are organized into projections

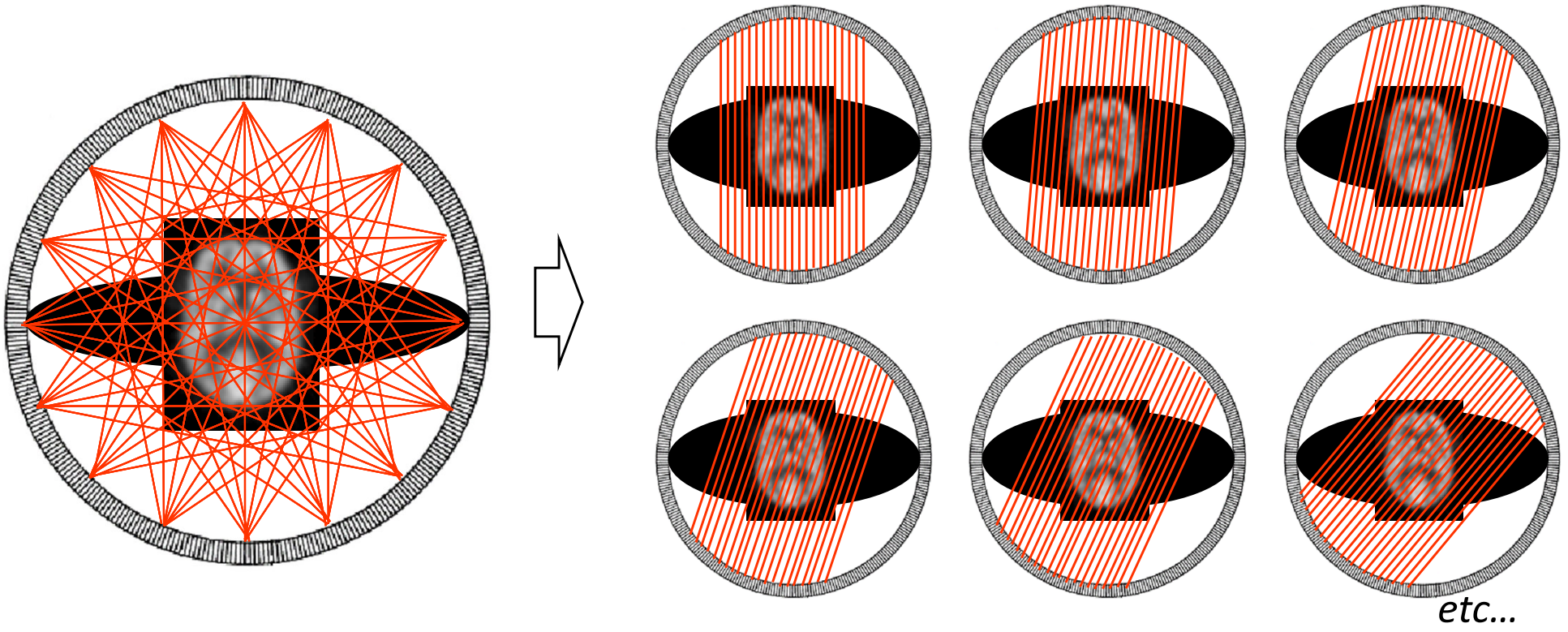

Statistical Description of the Projection Data

The probability of a given projection data $\mathbf{g}=(g_1, g_2, g_3, \ldots, g_M)$ *is*

$$p(\mathbf{g}) = \prod_{m=1}^{M} p(g_m) = \prod_{m=1}^{M} \frac{\bar{g}_m^{\,g_m}}{g_m!} e^{-\bar{g}_m}$$

Measured no. of counts on detector pixel m.

where $\bar{g}_m$ is the expected value for the number of counts on detector pixel #m

$$\bar{g}_m = \sum_{n=1}^{N} f_n p_{nm}$$

In the context of emission tomography, p_{nm} *is the probability of a gamma ray generated at a source pixel n is detected by detector element m.*

Remember that

$$\begin{pmatrix} \bar{g}_1 \\ \bar{g}_2 \\ \bar{g}_3 \\ \vdots \\ \bar{g}_M \end{pmatrix} = \begin{pmatrix} p_{11} & p_{12} & p_{13} & \cdots & p_{1N} \\ p_{21} & p_{22} & p_{23} & \cdots & p_{2N} \\ p_{31} & p_{32} & p_{33} & \cdots & p_{3N} \\ \vdots & \vdots & \vdots & \ddots & \vdots \\ p_{M1} & p_{M2} & p_{M3} & \cdots & p_{MN} \end{pmatrix} \begin{pmatrix} f_1 \\ f_2 \\ f_3 \\ \vdots \\ f_N \end{pmatrix}$$

The Maximum Likelihood Reconstruction

*Recall that the **likelihood function,** L(**f**,**g**), of a possible source function **f** is*

$$L(\boldsymbol{f},\boldsymbol{g}) = p(\boldsymbol{g} \mid \boldsymbol{f})$$

So that the maximum likelihood solution (the image that maximizing the likelihood function) can be found as

$$\hat{\boldsymbol{f}}_{\boldsymbol{ML}} = \underset{\boldsymbol{f}}{\operatorname{argmax}}\, L(\boldsymbol{f},\boldsymbol{g})$$

or equivalently

$$\hat{\boldsymbol{f}}_{\boldsymbol{ML}} = \arg\max_{\boldsymbol{f}} \log\left[L(\boldsymbol{f},\boldsymbol{g})\right] \equiv \underset{\boldsymbol{f}}{\operatorname{argmax}}\, l(\boldsymbol{f},\boldsymbol{g})$$

where $l(\boldsymbol{f},\boldsymbol{g})$ is the log-likelihood function

$$l(\boldsymbol{f},\boldsymbol{g}) = \log\left[L(\boldsymbol{f},\boldsymbol{g})\right]$$

Methods to Estimate the Underlying Image

The Maximum Likelihood Expectation Maximization (MLEM) Algorithm

$$f_n^{(new)} = \frac{f_n^{(old)}}{\sum_{m=1}^{M} p_{nm}} \sum_{m=1}^{M} \frac{g_m}{\sum_{n'=1}^{N} p_{n'm} f_{n'}^{(old)}} p_{nm}, \quad n = 1,2,...,N$$

Why PET?

Element of Life

- Interesting Chemistry

  Easily incorporated into biologically active drugs.

- 1 Hour Half-Life

  Maximum study duration is 2 hours.

  Gives enough time to do the chemistry.

- Easily produced

  Short half life $\Rightarrow$ local production.

^{18}F	*2 hour half-life*
^{15}O, ^{11}C, ^{13}N	*2–20 minute half-life*

glucose, H_2O, NH_3, CO_2, O_2, etc.

PET against SPECT

FIGURE 2. (A) Radionuclides that decay by positron emission result in two annihilation photons emitted 180° apart. If both photons are detected, the detection locations define (to within the distance traveled by the positron prior to annihilation) a line along which the decaying atom was located. (B) Radionuclides that decay by emitting single photons provide no positional information, as a detected event could originate from anywhere in the sample volume. (C) For single photon imaging, physical collimation can be used to absorb all photons except those that are incident on the detector from one particular direction (in this case perpendicular to the detector face), defining a line of origin just like the coincident 511-keV photons do following positron emission. To achieve this localization, however, the radiation from the majority of decays has been absorbed and does not contribute to image formation, leading to the detection of many fewer events for a given amount of radioactivity in the object. Absorptive collimation of this kind is the approach used in planar nuclear medicine imaging and in single photon emission computed tomography (SPECT).

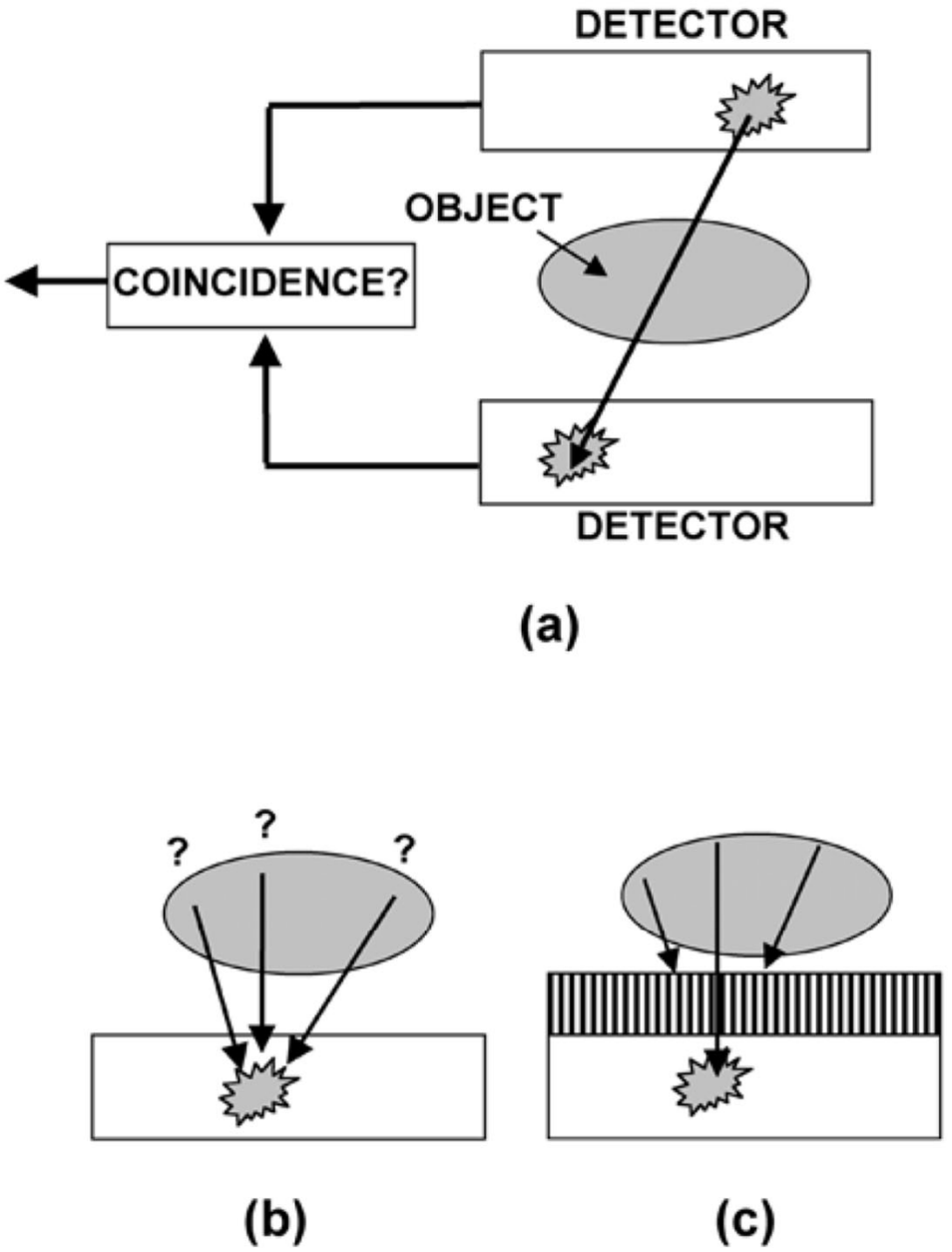

Total-Body PET: Maximizing Sensitivity to Create New Opportunities for Clinical Research and Patient Care

Simon R. Cherry[1,2], Terry Jones[2], Joel S. Karp[3], Jinyi Qi[1], William W. Moses[4], and Ramsey D. Badawi[1,2]

[1]Department of Biomedical Engineering, University of California, Davis, California; [2]Department of Radiology, University of California Davis Medical Center, Sacramento, California; [3]Department of Radiology, University of Pennsylvania, Philadelphia, Pennsylvania; and [4]Lawrence Berkeley National Laboratory, Berkeley, California

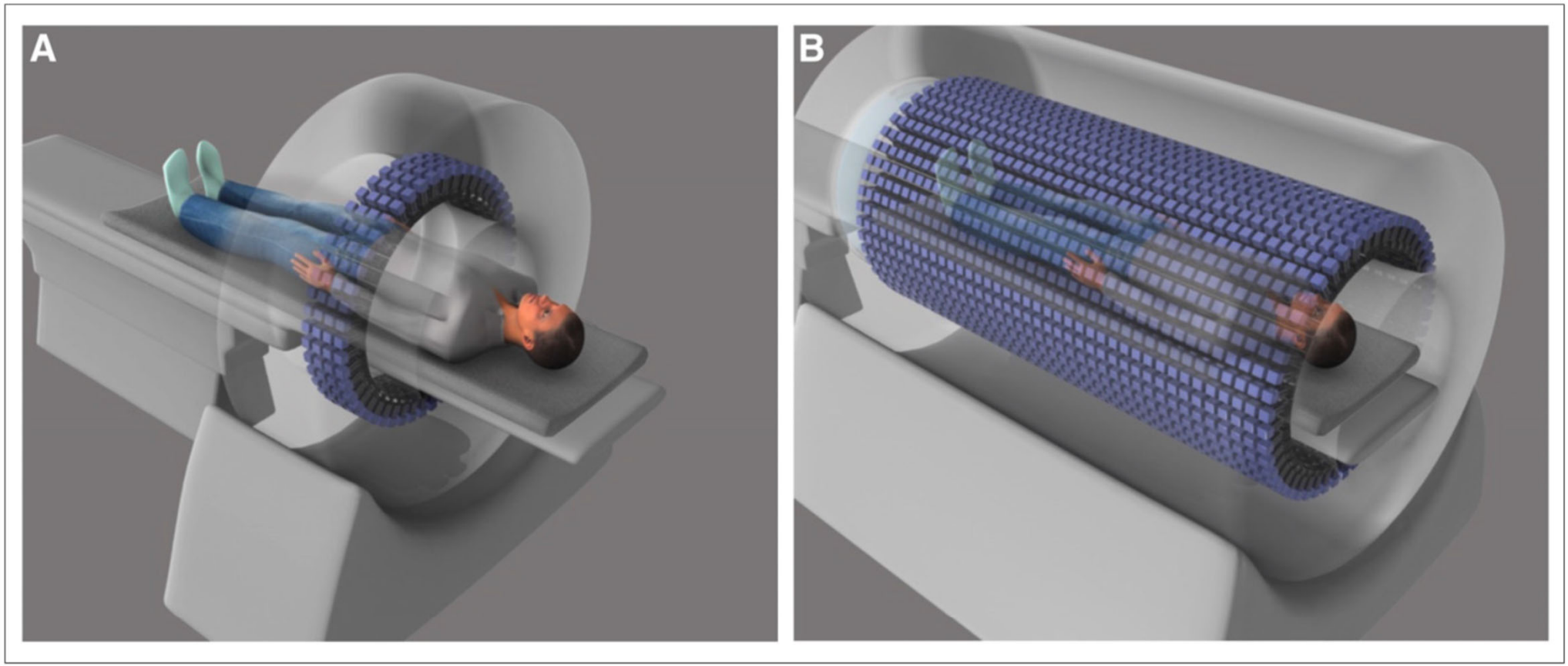

FIGURE 1. Whole-body PET (A) vs. total-body PET (B). (Reprinted with permission of (31).)

$$\mathrm{SNR} \approx k\sqrt{S \times A \times T}, \qquad \text{Eq. 1}$$

where k is a constant and S is the effective sensitivity of the scanner. If S is increased by a factor of 40, several consequences

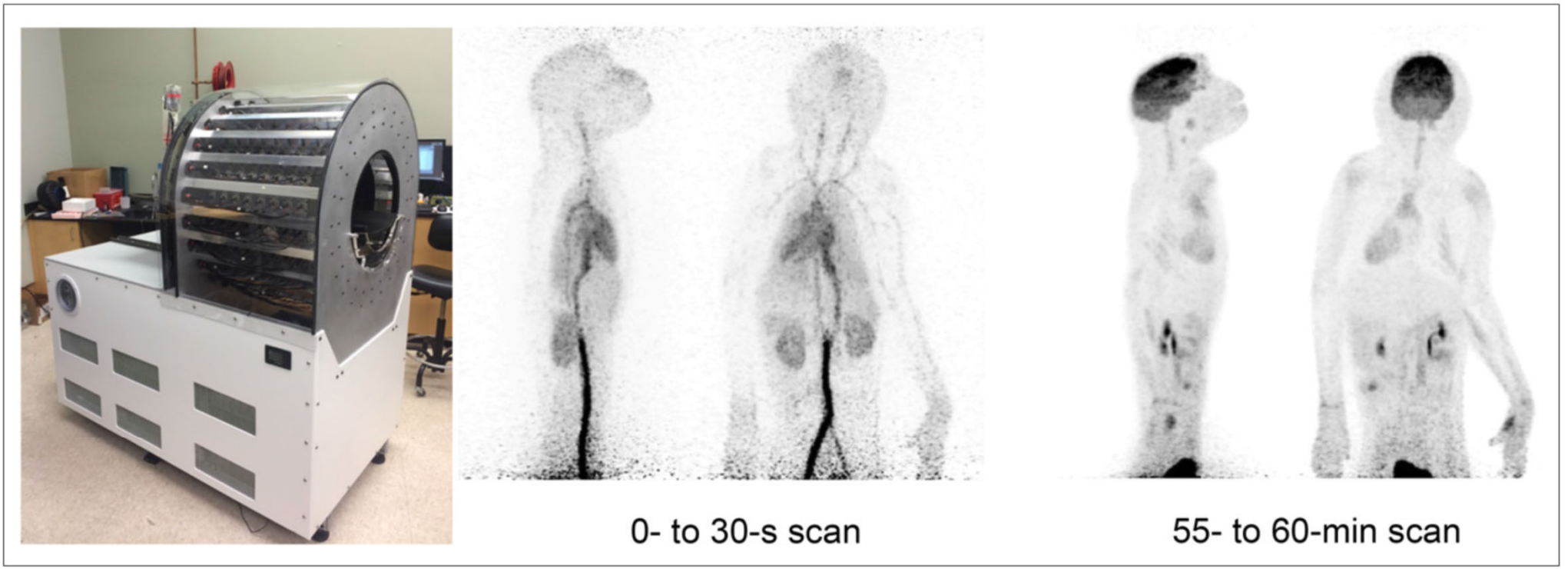

FIGURE 4. Photograph of mini EXPLORER scanner (left) and maximum-intensity-projection images of 2 frames from dynamic total-body imaging study after injection of 8.5 MBq of ^{18}F-FDG ($^{1}/_{10}$ standard activity) in 4.6-kg rhesus macaque (right).

PET: Impaired Image Quality in Larger Patients

Slim Patient

Large Patient

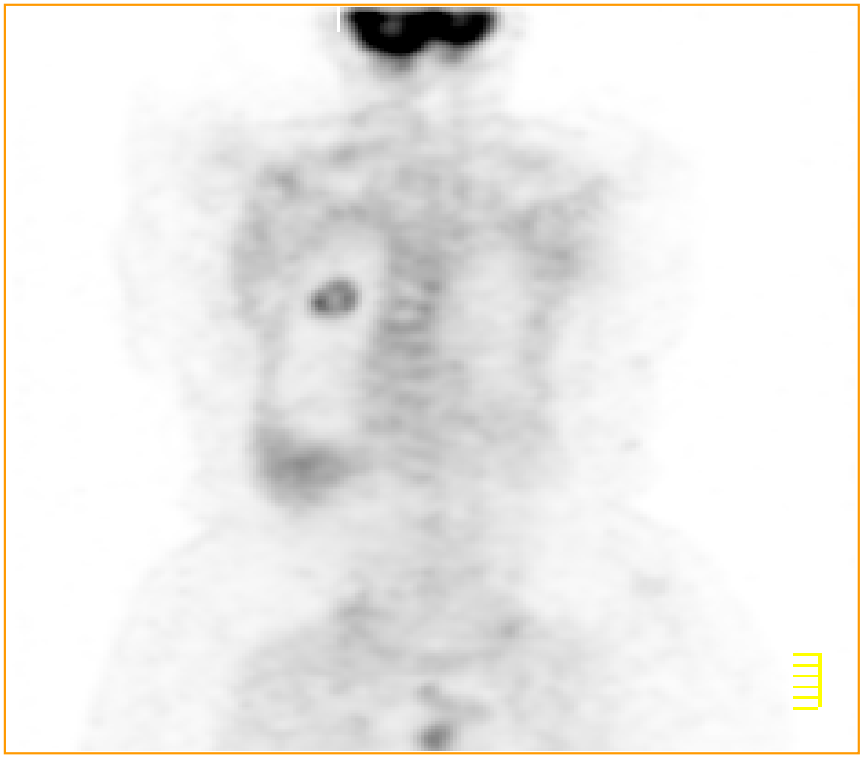

- *For an equivalent data signal to noise ratio, a 120 kg person would have to be scanned 2.3 times longer than a 60 kg person* [1)]

1) Optimizing Injected Dose in Clinical PET by Accurately Modeling the Counting-Rate Response Functions Specific to Individual Patient Scans. Charles C. Watson, PhD et al Siemens Medical Solutions Molecular Imaging, Knoxville, Tennessee, JNM Vol. 46 No. 11, 1825-1834, 2005

Attenuation Correction ⇒ Quantitation

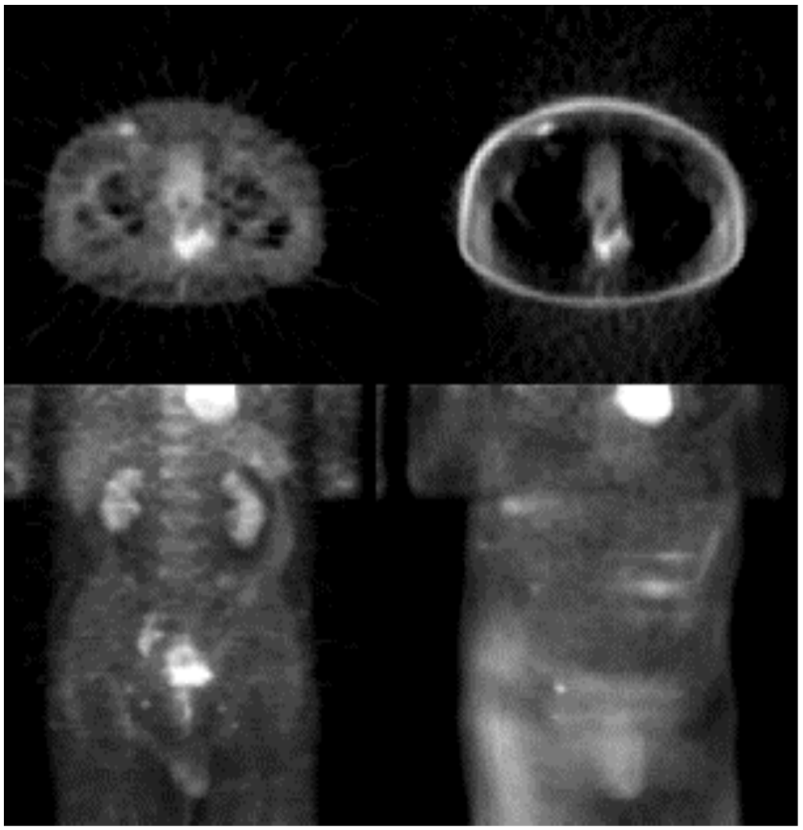

Transverse

Volume Rendered

Corrected *Uncorrected*

**Data courtesy of Duffy Cutler, Washington University*

\+ *Accurate Quantitation (µCi/cc) Possible*
– *Doubles Image Acquisition Time*

Attenuation of Internal Source

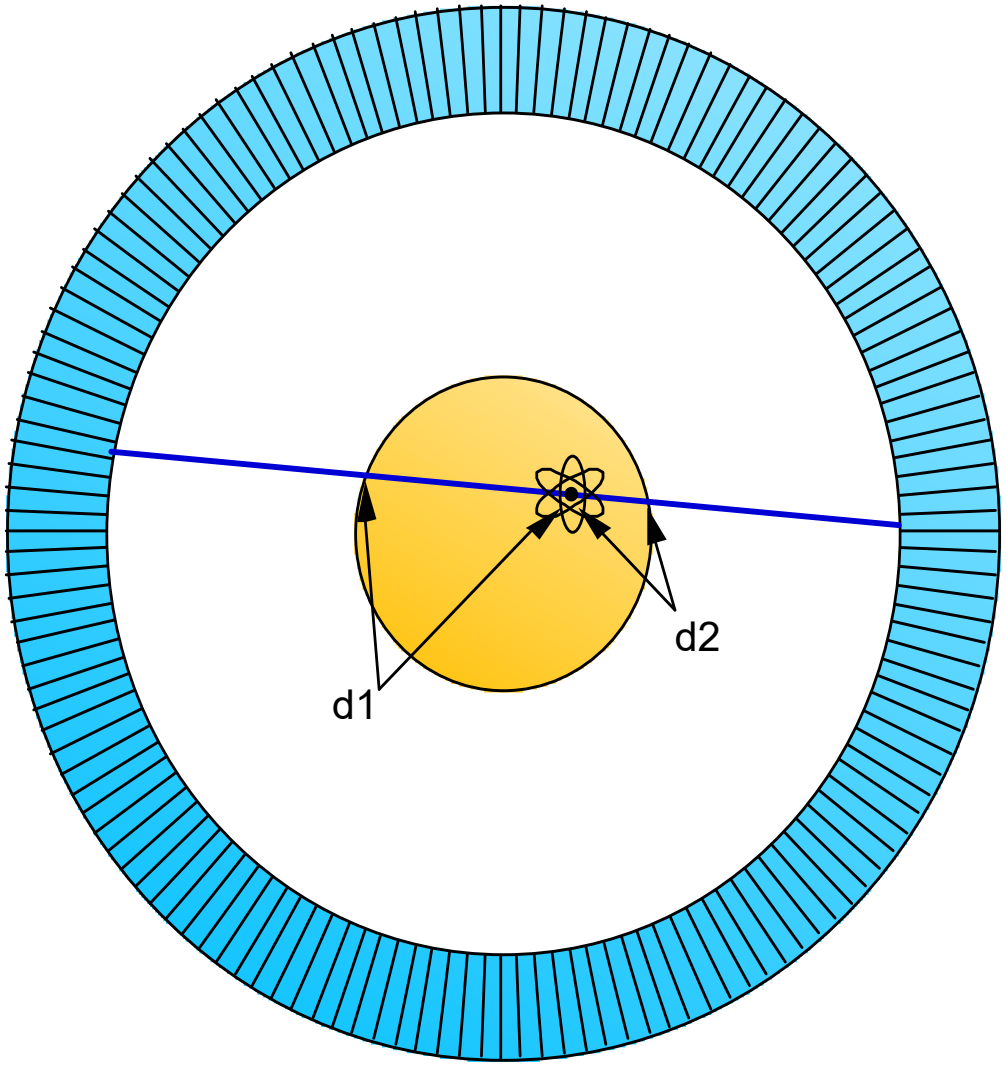

$$P_1 = e^{-\mu \cdot d1} \qquad P_2 = e^{-\mu \cdot d2}$$

$$P = e^{-\mu \cdot (d1+d2)}$$

Event detection probability is product of individual photon detection probabilities.

Fundamental Limitations on PET Imaging Performance

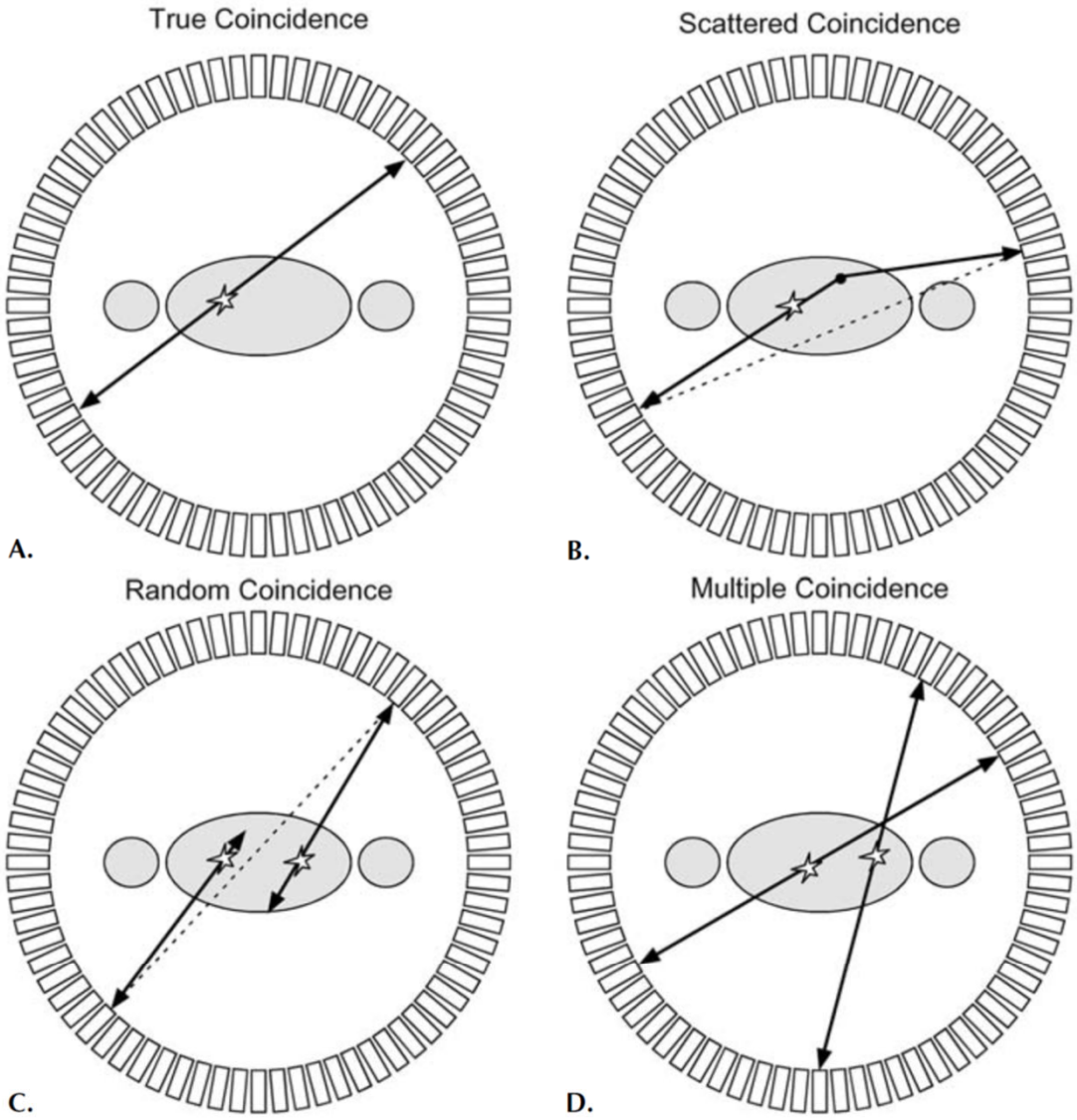

FIGURE 22. Illustration of the four main coincidence event types. A: True coincidence. Both annihilation photons escape the body and are recorded by a pair of detectors. B: Scattered coincidence. One or both of the two annihilation photons interacts in the body prior to detection. This results in a mispositioning of the event. C: Random coincidence: A coincidence is generated by two photons originating from two separate annihilations. These events form a background in the data that needs to be subtracted. D: Multiple coincidence: Three or more photons are detected simultaneously. Due to the ambiguity of where to position the events, these normally are discarded. (Reprinted from *Physics in Nuclear Medicine*, 2nd ed, Cherry SR, Sorenson JA, Phelps ME, W.B. Saunders, New York 1986, with permission from Elsevier.)

PET Data Acquisition

Signal and Noise

PET: Physics, Instrumentation, and Scanners

Simon R. Cherry and Magnus Dahlbom

Positron Range

TABLE 2. Select List of Radionuclides That Decay by Positron Emission and Are Relevant to PET Imaging

Radionuclide	*Half-life*	E_{max}(Mev)	β^+ *Branching Fraction*
^{11}C	20.4 min	0.96	1.00
^{13}N	9.97 min	1.20	1.00
^{15}O	122 s	1.73	1.00
^{18}F	109.8 min	0.63	0.97
^{22}Na	2.60 y	0.55	0.90
^{62}Cu	9.74 min	2.93	0.97
^{64}Cu	12.7 h	0.65	0.29
^{68}Ga	67.6 min	1.89	0.89
^{76}Br	16.2 h	Various	0.56
^{82}Rb	1.27 min	2.60, 3.38	0.96
^{124}I	4.17 d	1.53, 2.14	0.23

Based on data from Table of Nuclides: www2.bnl.gov/ton (accessed October 17th, 2002)

PET: Physics, Instrumentation, and Scanners

Simon R. Cherry and Magnus Dahlbom

Annihilation Radiation following Positron Emission

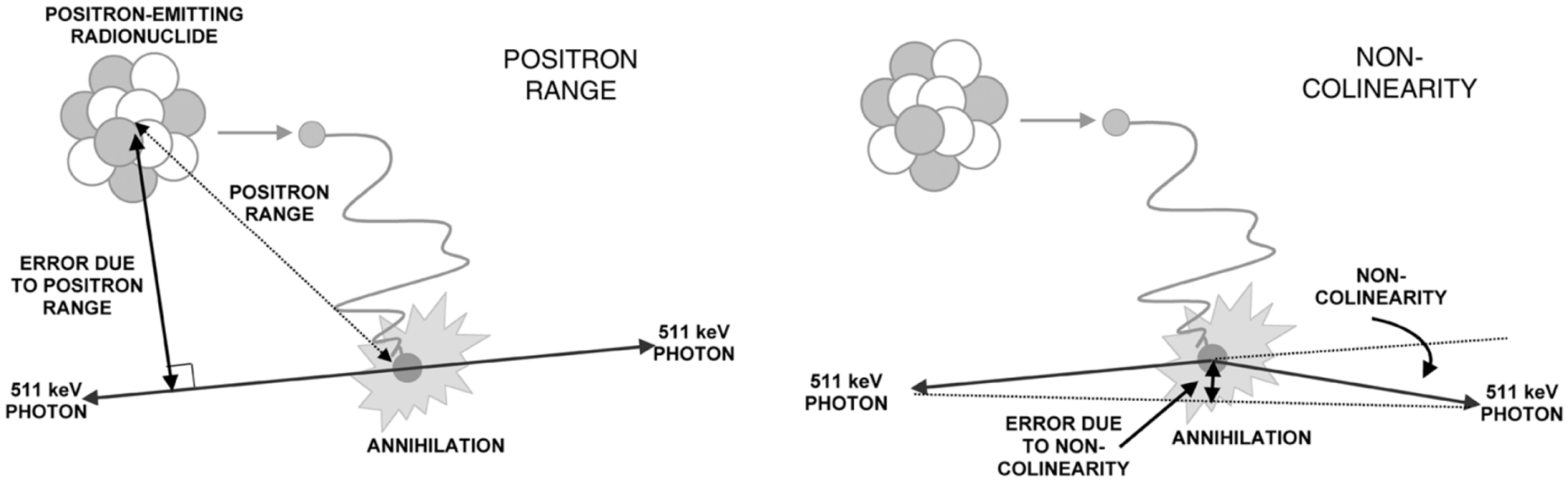

FIGURE 4. Error in determining the location of the emitting nucleus due to positron range (top) and noncolinearity (bottom). The positron range error is dependent on the energy of the emitted positrons. Noncolinearity is independent of radionuclide, and the error is determined by the separation of the detectors. The deviation from noncolinearity is highly exaggerated in the figure; the average angular deviation from 180° is about ± 0.25°. (Reproduced with permission from Cherry SR, Sorenson JA, Phelps ME. *Physics in Nuclear Medicine*, W.B. Saunders, New York, 2003.)

Positron Range

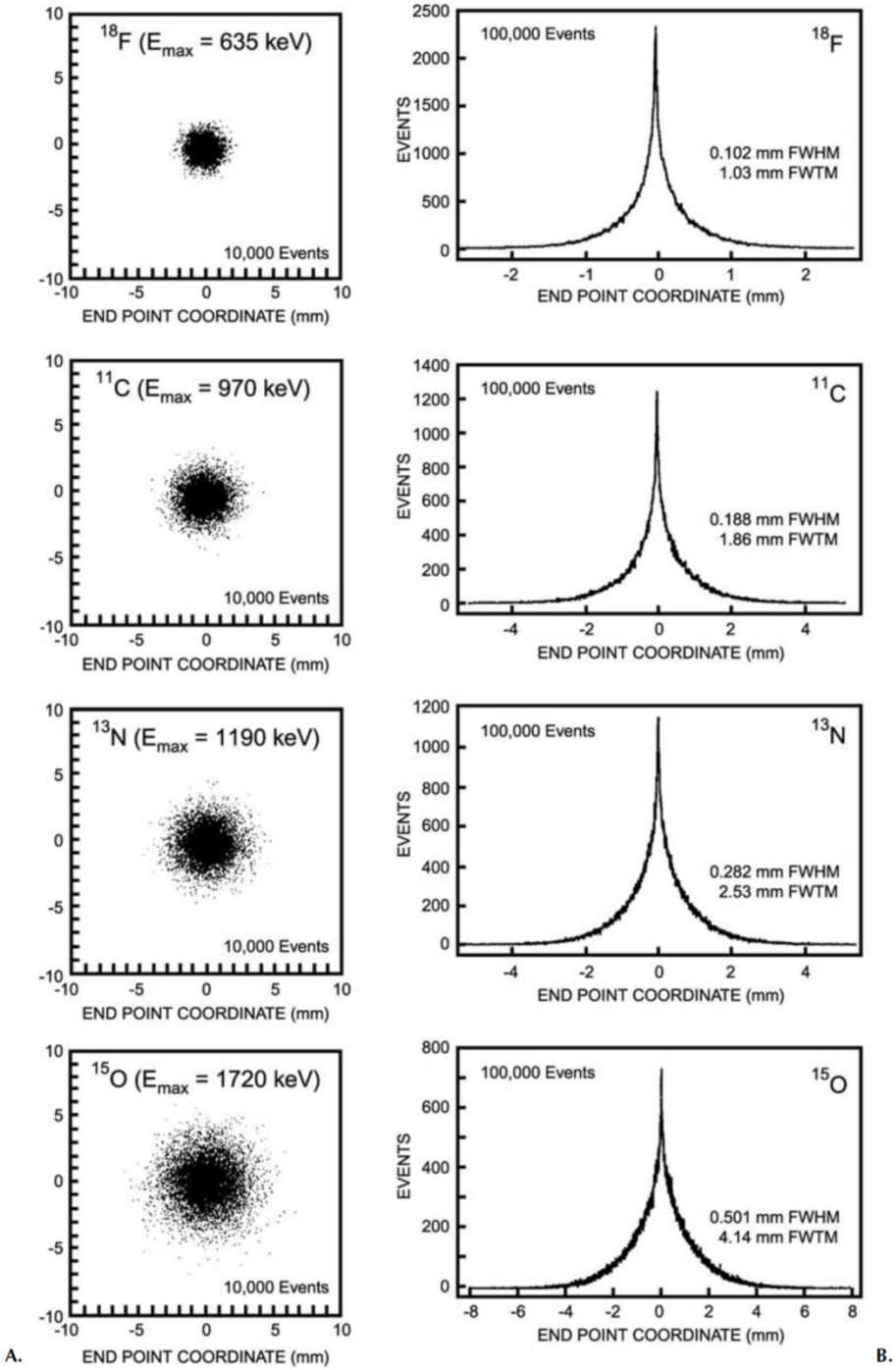

FIGURE 5. A: Simulations for several PET radionuclides showing the distribution of positron annihilation sites in water for positrons emitted at the center of the image (position 0.0 mm). B: Profiles through the simulated distributions showing measured FWHM and FWTM of the distributions. Abbreviations: FWHM, full width at half maximum; FWTM, full width at tenth maximum. (Reproduced with permission from Levin C, Hoffman EJ. *Phys Med Biol* 1999, 44: 781–799.)

PET: Physics, Instrumentation, and Scanners

Simon R. Cherry and Magnus Dahlbom

Noncollinearity

noncolinearity. This effect is independent of radionuclide because the positrons must lose most of their energy before they can annihilate; hence, the initial energy is irrelevant. The distribution of emitted angles is roughly Gaussian in shape, with a full width at half maximum (FWHM)* of ~0.5°. After detecting the annihilation photons, PET assumes that the emission was exactly back to back, resulting in a small error in locating the line of annihilation (Figure 4 bottom). Assuming a Gaussian distribution and using the fact that the angles are small, the blurring effect due to noncolinearity, Δ_{nc}, can be estimated as:

$$\Delta_{nc} = 0.0022 \times D \tag{10}$$

where D is the diameter of the PET scanner. The error increases linearly as the diameter of the PET scanner increases. Once again, the effect is relatively small compared with the detector resolution in most clinical PET scanners. In PET scanners used for animals, D generally is small, and as illustrated in Example 4, noncolinearity is not a major limiting factor at the present time.

EXAMPLE 4

Calculate the blurring due to photon noncolinearity in an 80-cm diameter PET scanner designed for imaging humans and in a 15-cm diameter PET scanner designed for imaging small animals.

ANSWER

From Equation 10, the blurring is calculated as:

80-cm human scanner:

$$\Delta_{nc} = 0.0022 \times D = 0.0022 \times 800 \text{ mm} = 1.76 \text{ mm}$$

15-cm small-animal scanner:

$$\Delta_{nc} = 0.0022 \times D = 0.0022 \times 150 \text{ mm} = 0.33 \text{ mm}$$

Fundamental Challenges on PET Detector Technology

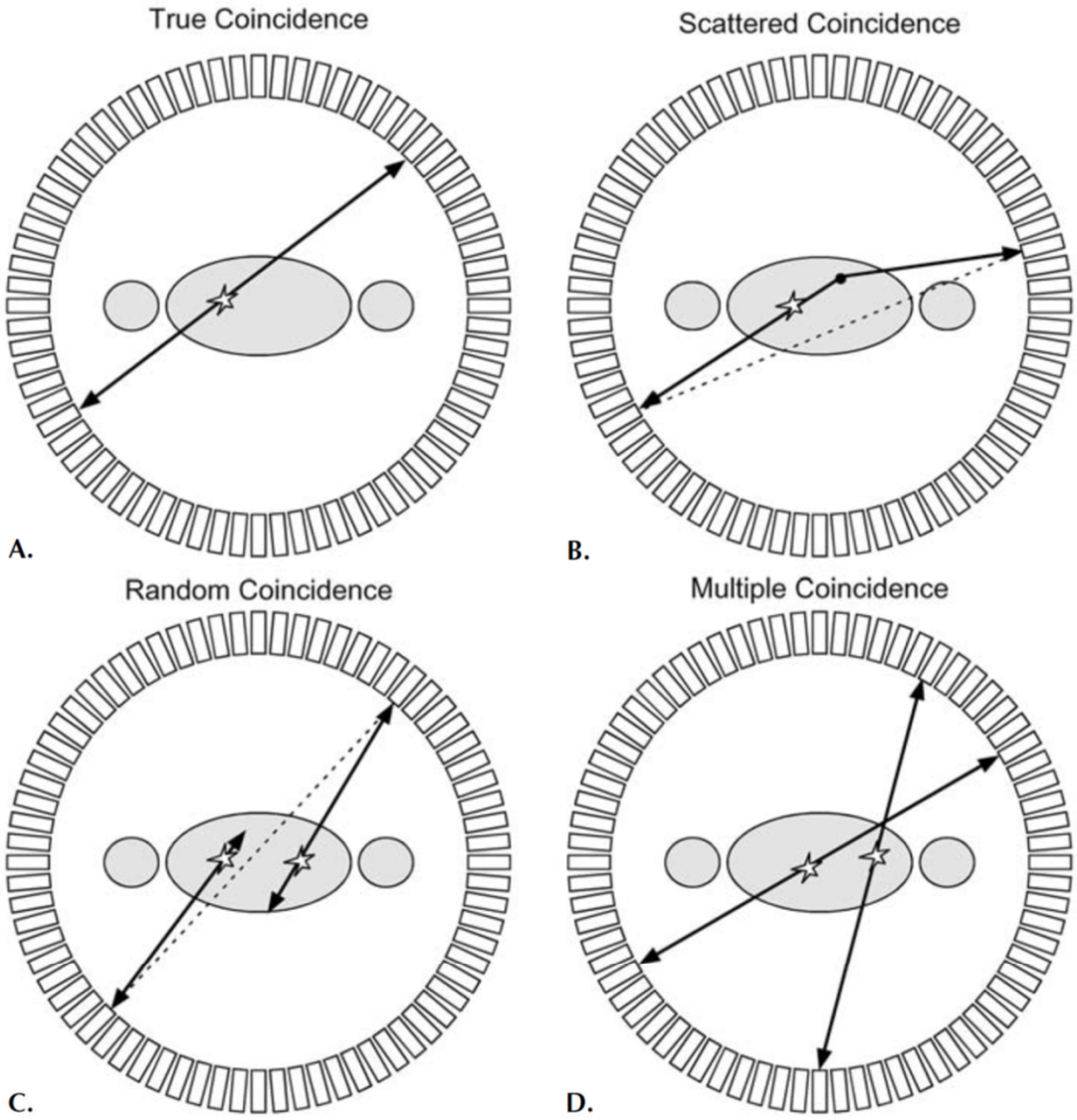

FIGURE 22. Illustration of the four main coincidence event types. A: True coincidence. Both annihilation photons escape the body and are recorded by a pair of detectors. B: Scattered coincidence. One or both of the two annihilation photons interacts in the body prior to detection. This results in a mispositioning of the event. C: Random coincidence: A coincidence is generated by two photons originating from two separate annihilations. These events form a background in the data that needs to be subtracted. D: Multiple coincidence: Three or more photons are detected simultaneously. Due to the ambiguity of where to position the events, these normally are discarded. (Reprinted from *Physics in Nuclear Medicine*, 2nd ed, Cherry SR, Sorenson JA, Phelps ME, W.B. Saunders, New York 1986, with permission from Elsevier.)

PET Data Acquisition

Signal and Noise

PET: Physics, Instrumentation, and Scanners

Simon R. Cherry and Magnus Dahlbom

PET Camera & Detector Design

- *Typical Parameters*
- *Detector Module Design*

What Do We Need for PET Detector?

- *Efficient – 511keV gamma rays are not easily stopped in detector.*
- *Excellent timing accuracy (typically a few ns) – for coincidence measurements.*
- *Capability of a very high counting rate (e.g. 0.5MC/s per cm^2)*
- *High detector spatial resolution – for high imaging resolution. Currently 4 mm x 30mm in commercial clinical PET scanners.*
- *Cost-effective – very large detector volume is needed for practical PET systems.*

Scintillation Crystal Properties

TABLE 1 Properties of Common Scintillation Crystals Used in Small-FOV Imager Designs

Scintillator	Effective Z	Density (g/cc)	Radiation Length (mm)[a]	Relative Light Yield	Refractive Index	Decay Time (ns)	Peak Emission Wavelength (nm)	Hygroscopic?	Rugged?
NaI(Tl)	51	3.67	3.4	100	1.85	230	410	Yes	No
CsI(Tl)	54	4.51	2.2	135	1.79	1000	530	No	Yes
CsI(Na)	54	4.51	2.2	75	1.79	650	420	No	Yes
BGO	74.2	7.13	10.5	15	2.15	300	480	No	Yes
LSO(Ce)	65.5	7.4	11.6	75	1.82	40	420	No	Yes
$CaF_2(Eu)$[b]	16.9	3.17	N/A	50	1.43	940	435	No	Yes

[a]Radiation lengths for NaI(Tl), CsI(Tl) and CsI(Na) are for 140-keV photons; Values for BGO and LSO are at 511 keV.
[b]$CaF_2(Eu)$ is used in beta imaging.

Lutetium Orthosilicate (LSO) Scintillator

Compared to BGO, LSO has:

Same Attenuation Length:

⇒ *Good Spatial Resolution*

Higher Light Output:

⇒ *Decode More Crystals per Block*

⇒ *Better SNR for "Enhanced" Readout (e.g. Depth of Interaction)*

Shorter Decay Time:

⇒ *Less Dead Time (Allows Larger Block Areas)*

⇒ *Better Timing Resolution*

Reduce Cost OR Increase Performance

PET Cameras

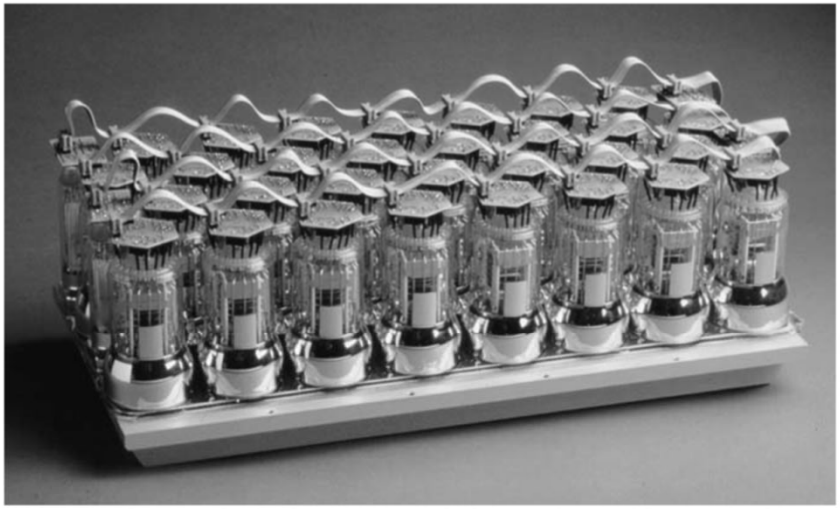

FIGURE 15. Photograph of a large-area NaI(Tl) detector designed for PET applications. The scintillator plate is 50 cm long by 15 cm wide by 2.5 cm thick and is read by thirty, 5-cm diameter PM tubes. Six of these detectors have been used in an hexagonal array to form a PET scanner. (Photograph courtesy of Dr. Joel Karp, University of Pennsylvania.)

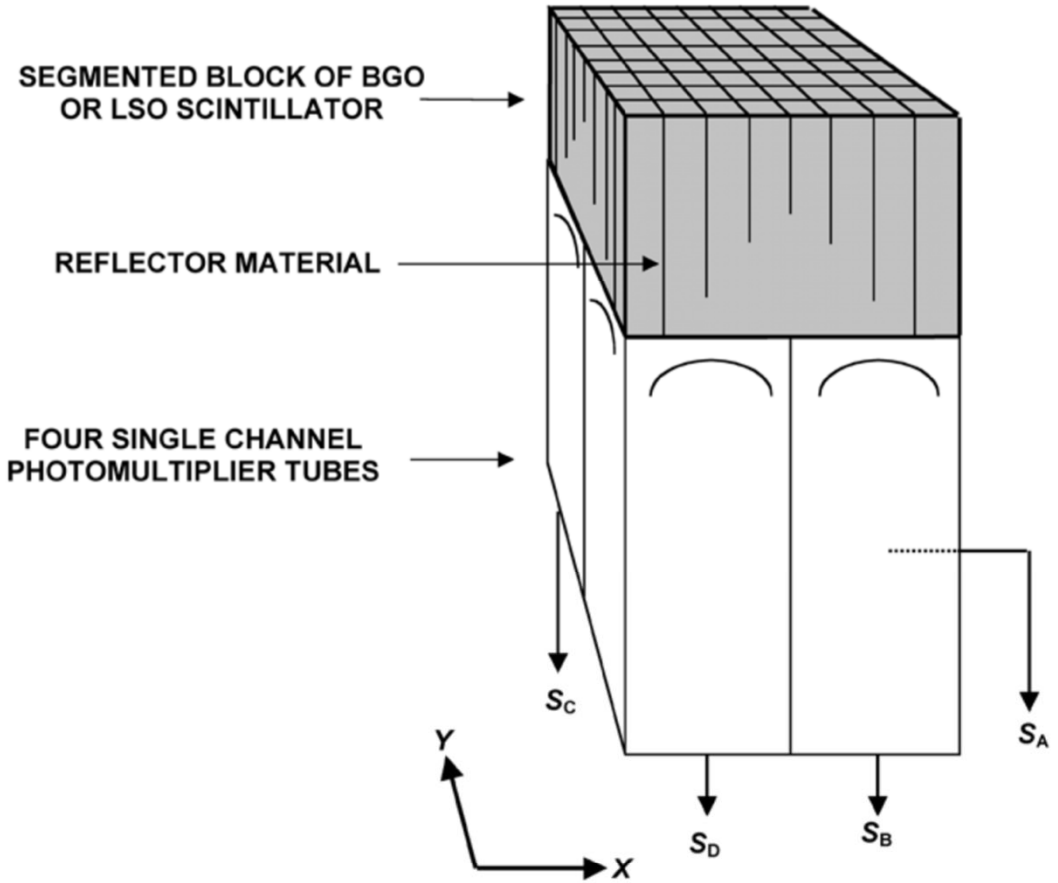

FIGURE 12. Schematic drawing of a typical PET block detector. A block of scintillator is segmented into an 8×8 array using a diamond saw. White reflective material is used in the saw cuts to optically isolate elements. Depth of the saw cuts determines the spread of scintillation light onto four single-channel photomultiplier tubes. By looking at the ratio of signals in the four PMTs, the detector element in which an annihilation photon interacted can be determined. (Reproduced with permission from Cherry SR, Sorenson JA, Phelps ME. *Physics in Nuclear Medicine*, W.B. Saunders, New York, 2003.)

Quadrant Sharing

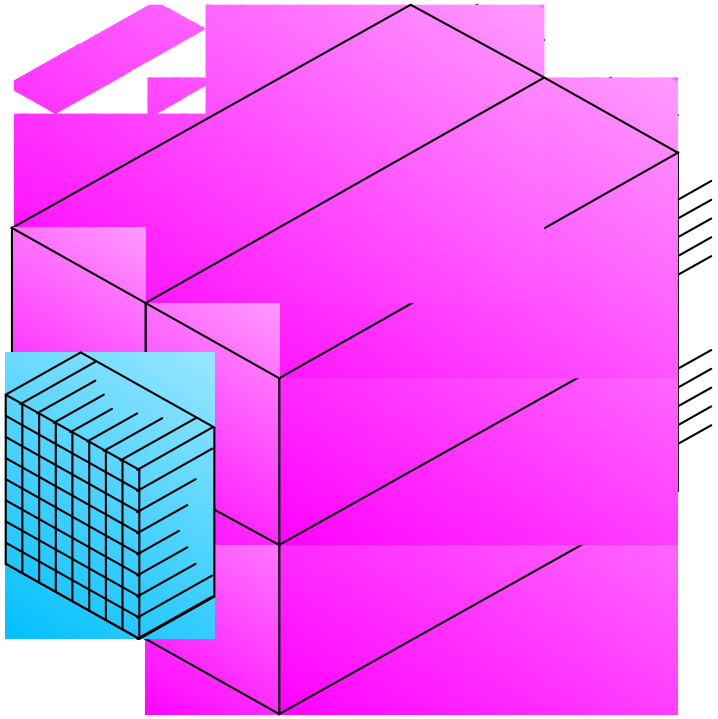

Perspective View

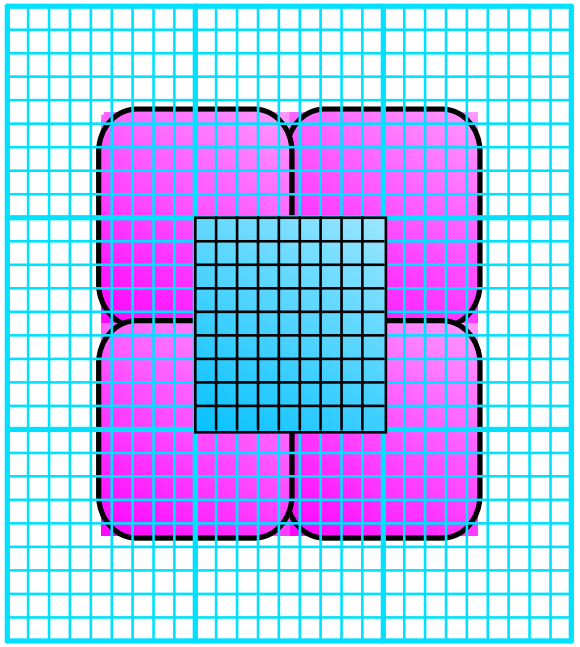

Front View

Each PMT Services 4 Crystal Blocks (Not 1)
(Number of PMTs = Number of Blocks)

+ *Cost of PMTs Reduced 4x*
– *Dead Time Increased 9x*

Photodiode Detectors

Figure 1-1 Photodiode cross section

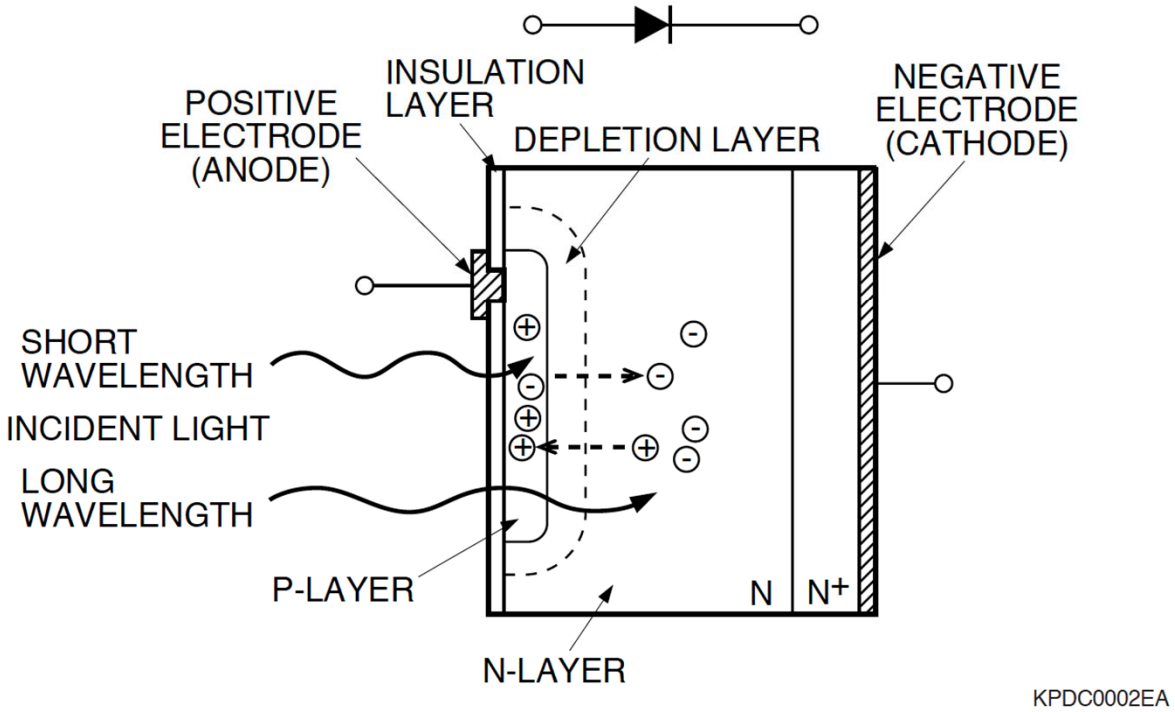

Typical reversed-biased photodiode detectors

- *No internal gain*
- *Very high QE for red light (up to 90%)*
- *Limited timing resolution*

Hamamatsu photodiode technical information

Avalanche Photodiode (APD)

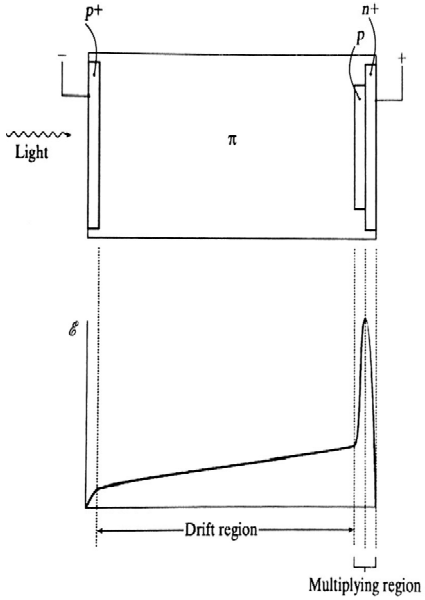

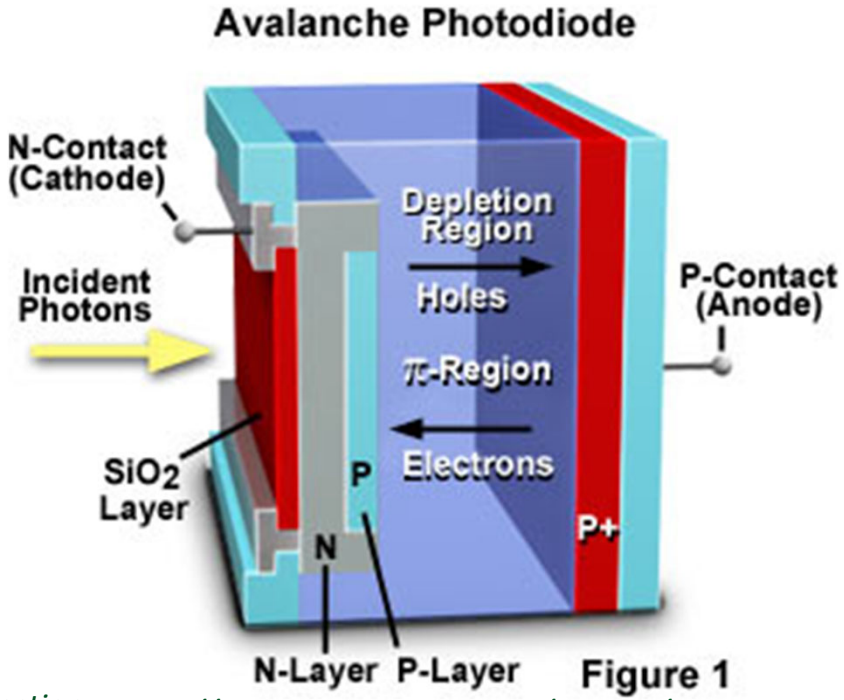

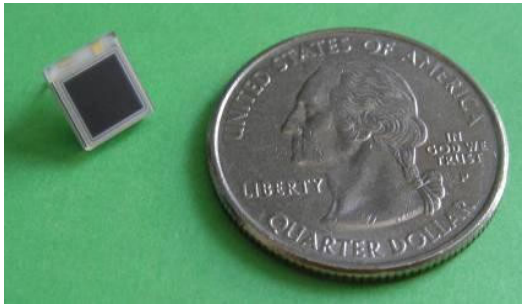

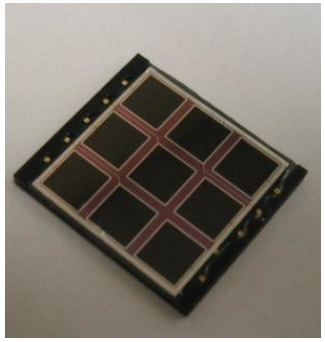

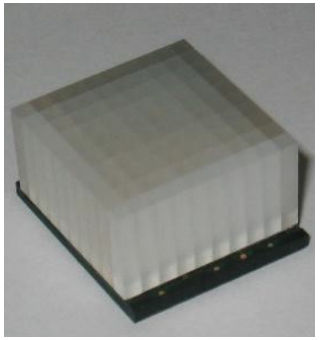

From K F Knoll, Radiation Detection and Measurements, Third Edition, Wiley.

http://learn.hamamatsu.com/articles/avalanche.html

***Avalanche Photo Diodes (APD)**, proof to be suitable detectors for PET/MRI*

- *Could be operated inside strong magnetic field*
- *Added internal gain*
- *Fast timing property*
- *Gain critically depends on bias voltage*
- *Temperature stability could be an issue*

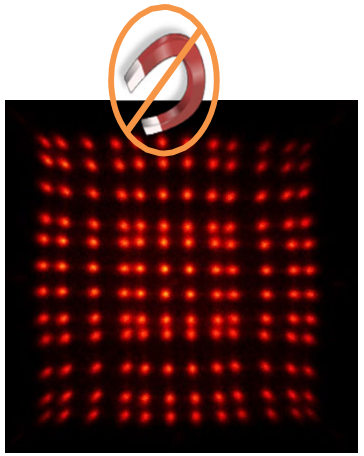

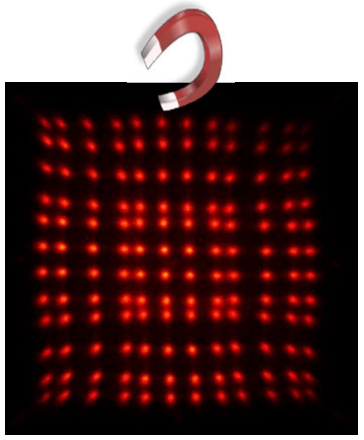

Silicon Photomultipliers

Silicon Photo Multipliers (SiPM, Geigermode-APD)
a novel MR compatible PET detector

G-APD 6.5 x 7 mm² *3 x 3 mm², 60x60 cells* *Each cell 50 x 50 µm²*

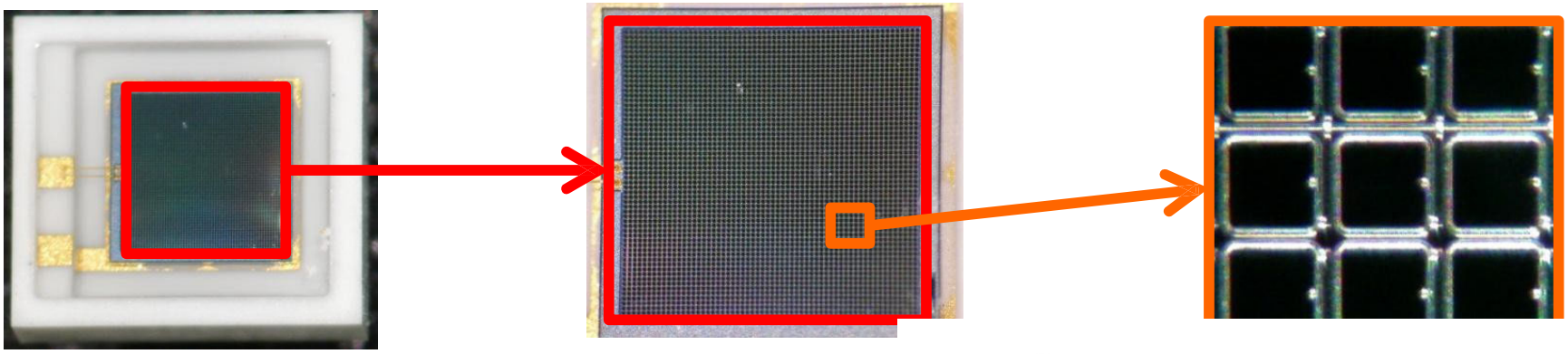

- *Each cell is operated above breakdown*
- *Output signal is sum of all cells*
- *Each cell provides maximum-gain signal on photon interaction*

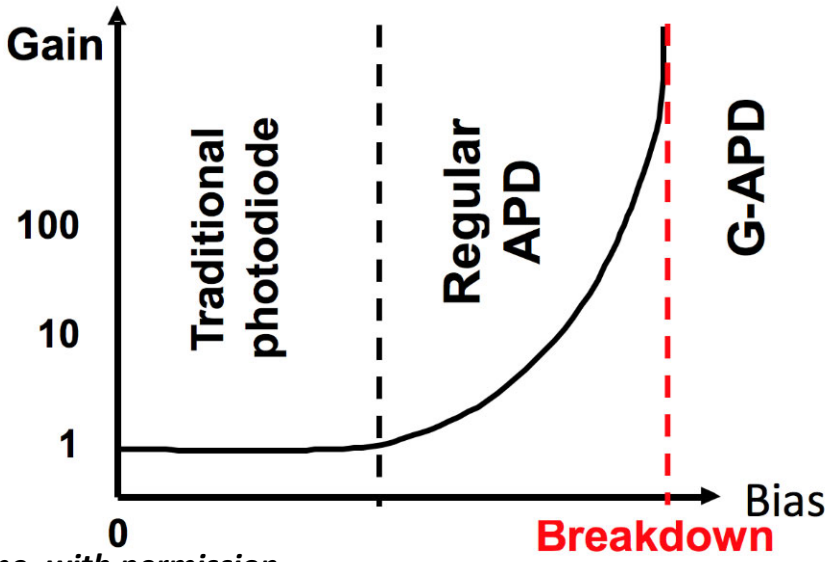

This slide was derived from Martin S. Judenhofer, Seminars in Nuclear Medicine, with permission.

Silicon Multiplier (SiPM) Detectors

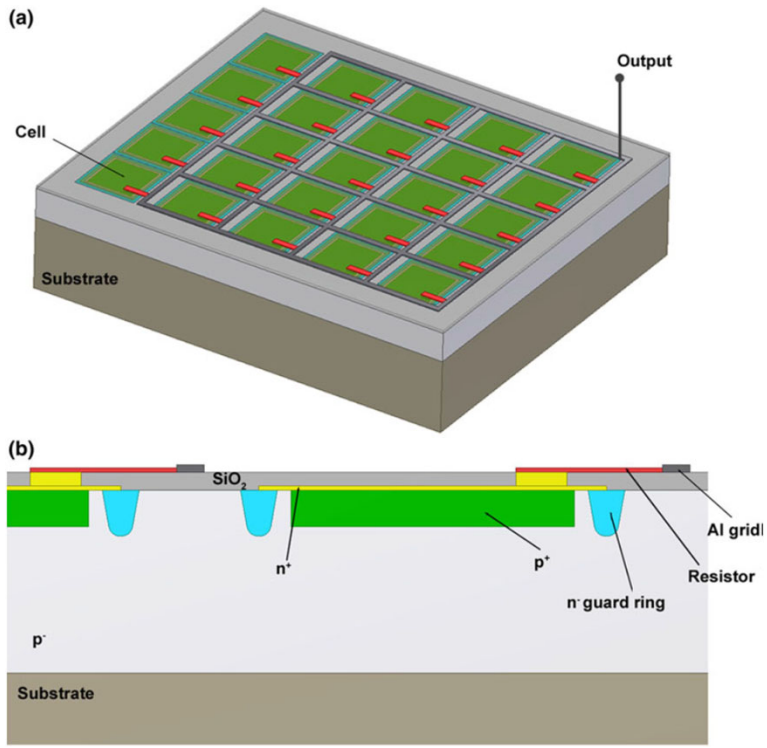

FIGURE 1. (a) Simplified structure of a SiPM composed of G-APD cells. The G-APDs are joined together on a common substrate and are electrically decoupled. The outputs of the cells are connected to an Al grid used for the readout of the output signals. Each cell has a quenching resistor in series. (b) Each cell (G-APD) is a p–n junction with a very thin depletion layer between p+ and n+ layers.15 Drawings courtesy of Julien Bec, UC Davis.

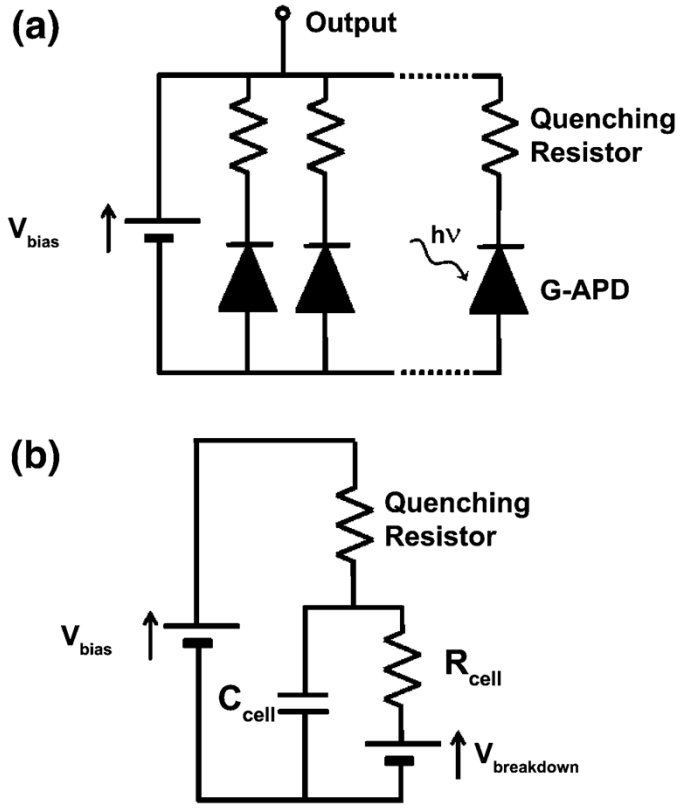

FIGURE 2. (a) Simplified electric structure of a SiPM com- posed of several G-APDs in series with a quenching resistor. (b) Equivalent circuit of a single cell when the device is on (a bias voltage Vbias is applied) and is detecting photons. The capacitor Ccell initially charged at Vbias discharges through Rcell dropping the bias voltage to Vbreakdown. The avalanche process is quenched via the quenching resistor and then the device is recharged.

EMILIE RONCALI and SIMON R. CHERRY, Application of Silicon Photomultipliers to Positron Emission Tomography, *Annals of Biomedical Engineering, Vol. 39, No. 4, April 2011 (2011) pp. 1358–1377*

Silicon Multiplier (SiPM) Detectors

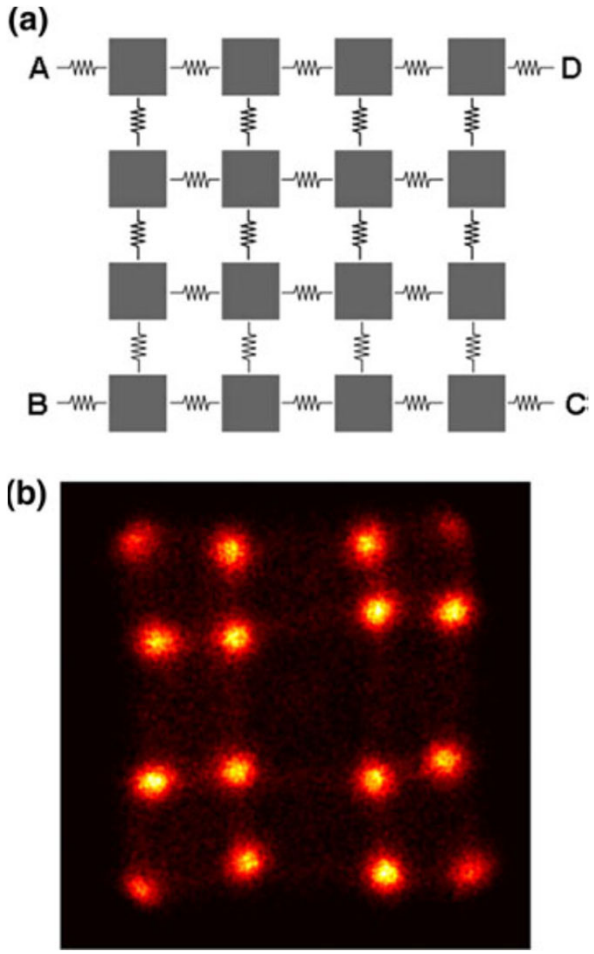

FIGURE. (a) Resistive network for a 4 x 4 SiPM array, (b) Crystal map acquired with a ^{22}Na source irradiating a 4x4 array of 1.5 x 1.5 x 20 mm^3 LSO scintillator crystals coupled to the SiPM array.

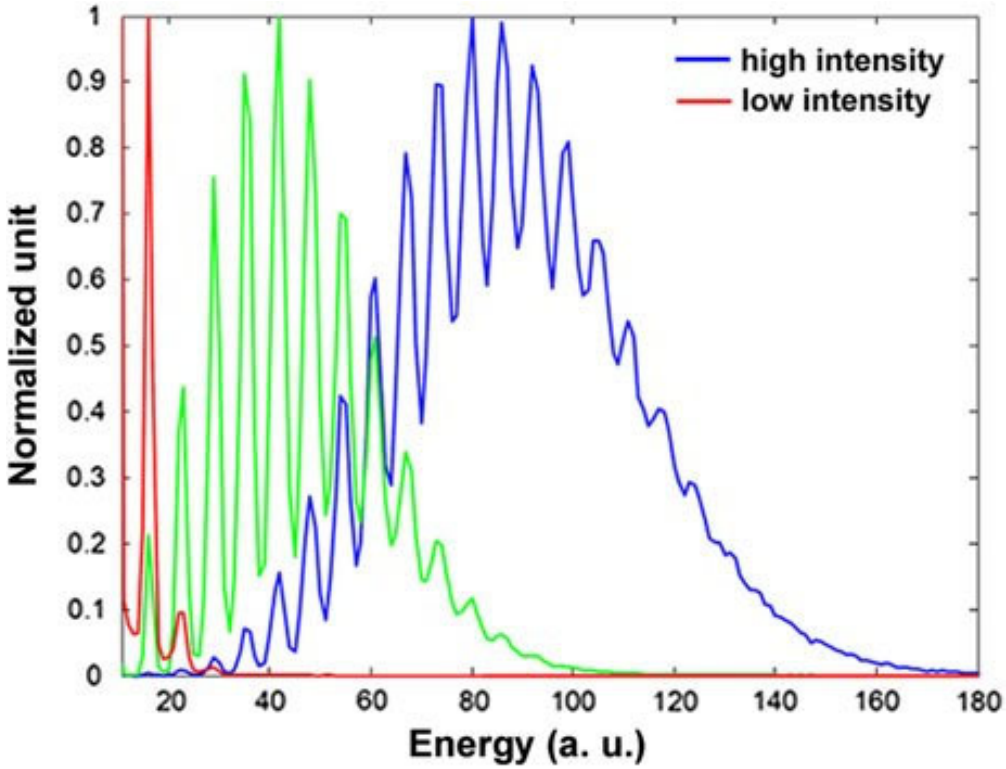

FIGURE 3. Pulse height spectra from a 1 3 1 mm2 Ham- amatsu MPPC S10362-11-025C acquired for three different light intensities (the red and blue curves correspond to the lowest and strongest intensities, respectively) showing peaks corresponding to different numbers of photoelectrons generated.

EMILIE RONCALI and SIMON R. CHERRY, Application of Silicon Photomultipliers to Positron Emission Tomography, *Annals of Biomedical Engineering, Vol. 39, No. 4, April 2011 (2011) pp. 1358–1377*

Silicon Multiplier (SiPM) Detectors

Sogang University, Korea – GAPD based PET insert

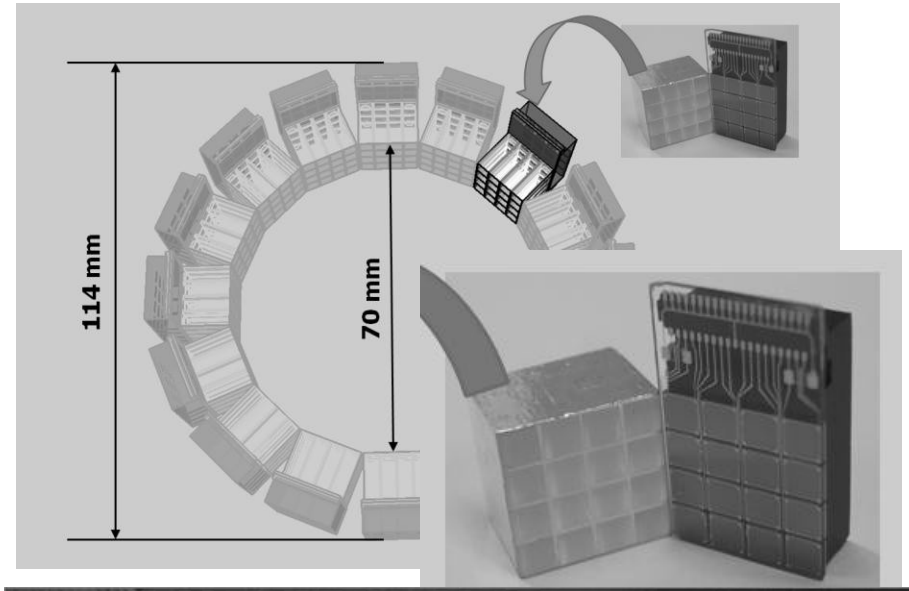

- *based on 4x4 GAPD arrays*
- *3x3x10 mm³LYSO scintillators*
- *16 block detectors*
- *70 mm inner diameter / 13 mm axial*
- *2.8 mm spatial resolution*
- *charge signal transmission readout*

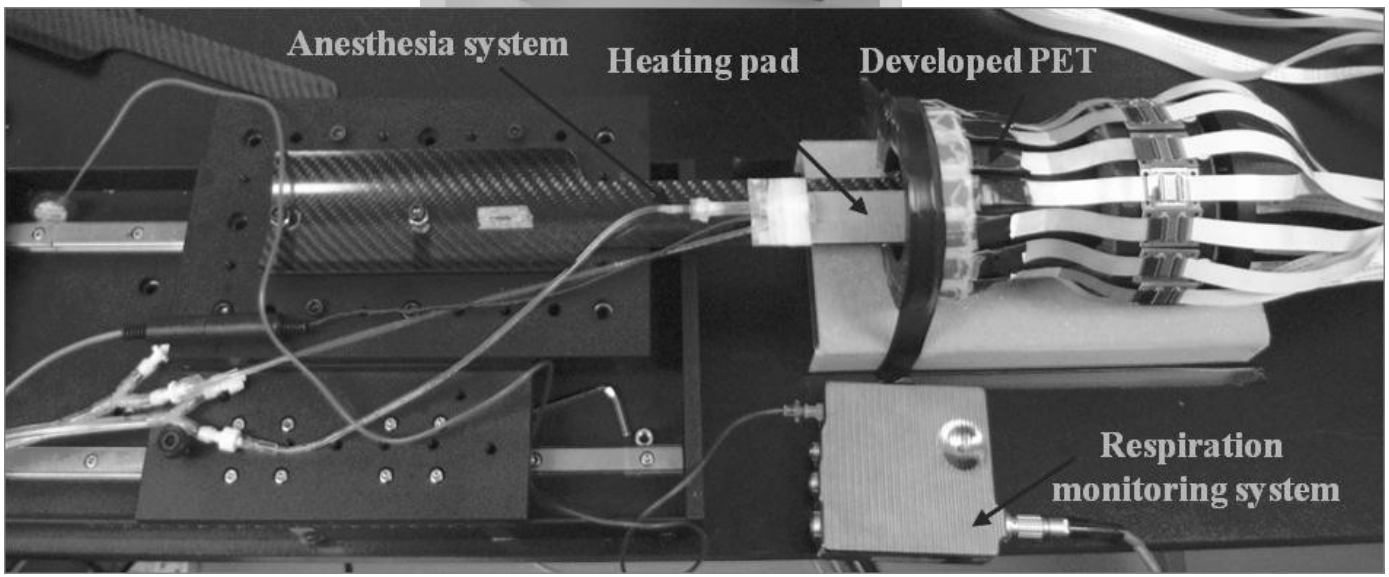

Kang J, et al., ***A small animal PET based on GAPDs and charge signal transmission approach for hybrid PET-MR***
JInst. 6-P08012, Aug 2011

Silicon Multiplier (SiPM) Detectors for PET Applications

HYPER Imaging Project, RWTH-University, Aachen

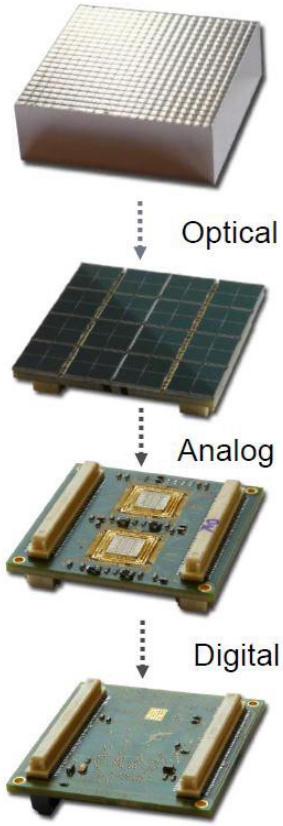

22 x 22 = 484 LYSO crystals, each 1.32 x 10 mm³

SiPM with 42 mm² in monolithic arrays of 2 x 2 SiPMs

2 x ASICs with 40(32) channels with individual EDC/TDC

Parallel FPGA data processing

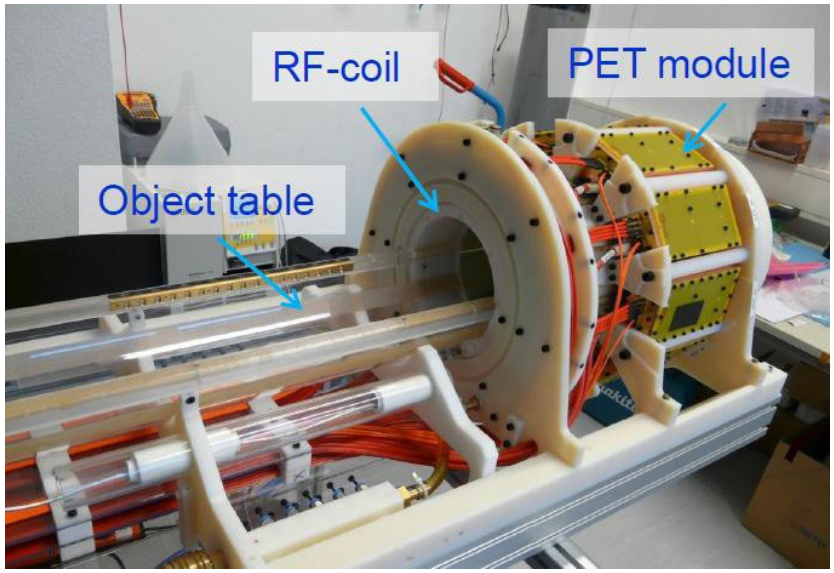

Small animal PET insert build for 3T Human MRI

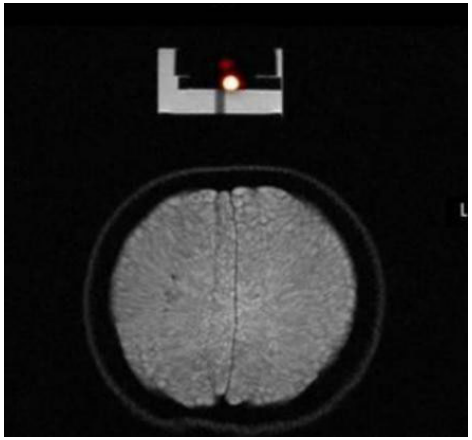

Slide Courtesy: Volkmar Schulz, RWTH

This slide was adopted from Martin S. Judenhofer, Seminars in Nuclear Medicine, with permission.

Timing Resolution and Time-of-Flight PET

Imperfections in PET Image Acquisation

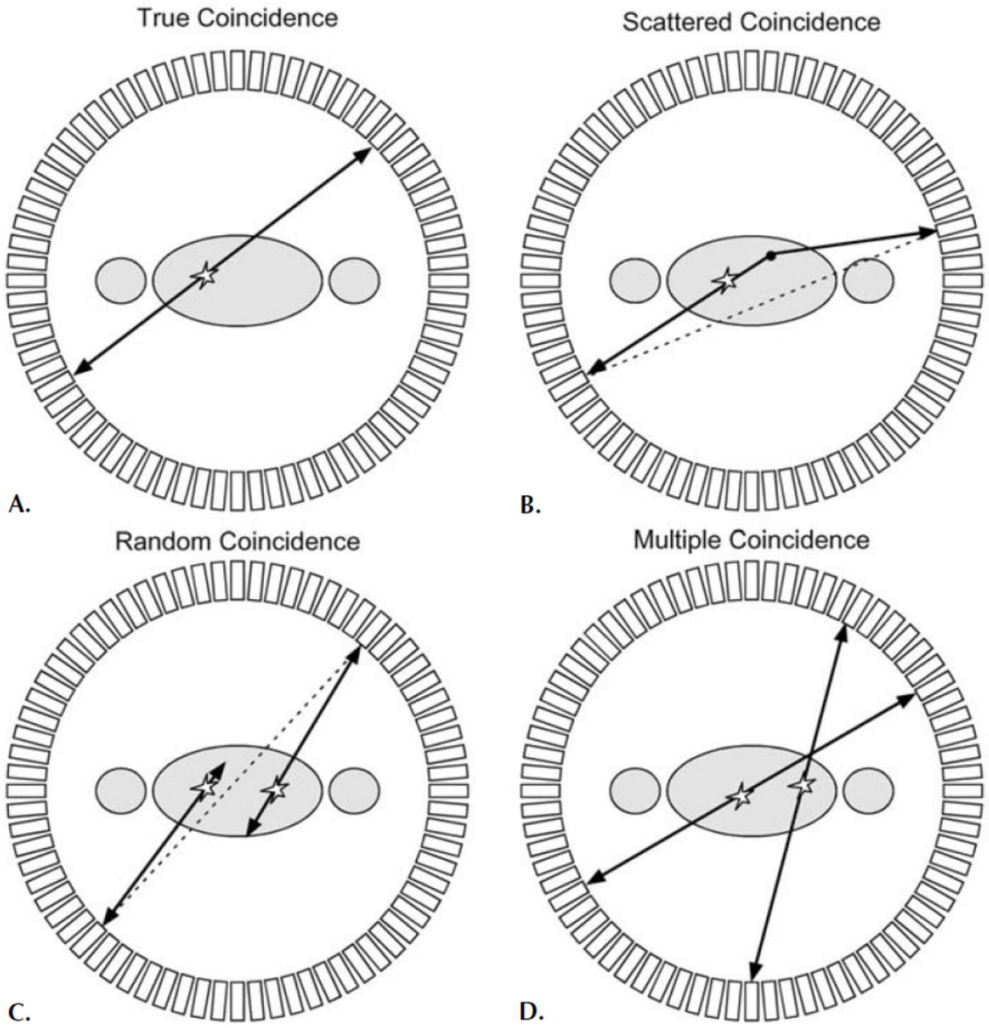

FIGURE 22. Illustration of the four main coincidence event types. A: True coincidence. Both annihilation photons escape the body and are recorded by a pair of detectors. B: Scattered coincidence. One or both of the two annihilation photons interacts in the body prior to detection. This results in a mispositioning of the event. C: Random coincidence: A coincidence is generated by two photons originating from two separate annihilations. These events form a background in the data that needs to be subtracted. D: Multiple coincidence: Three or more photons are detected simultaneously. Due to the ambiguity of where to position the events, these normally are discarded. (Reprinted from *Physics in Nuclear Medicine*, 2nd ed, Cherry SR, Sorenson JA, Phelps ME, W.B. Saunders, New York 1986, with permission from Elsevier.)

Noise Equivalent Count Rate (NECR)

$$NECR = \frac{T^2}{T + S + R}$$

T: true count-rate, S: scattered count-rate, R: random count rate

NECR Properties:

- Like a Signal / Noise Ratio
  (Sensitivity only Includes Signal).
- Includes Noise from Backgrounds.
- Statistical Noise Variance $\propto$ NECR.

Maximize NECR to Minimize Image Noise

NECR Depends On Activity Density

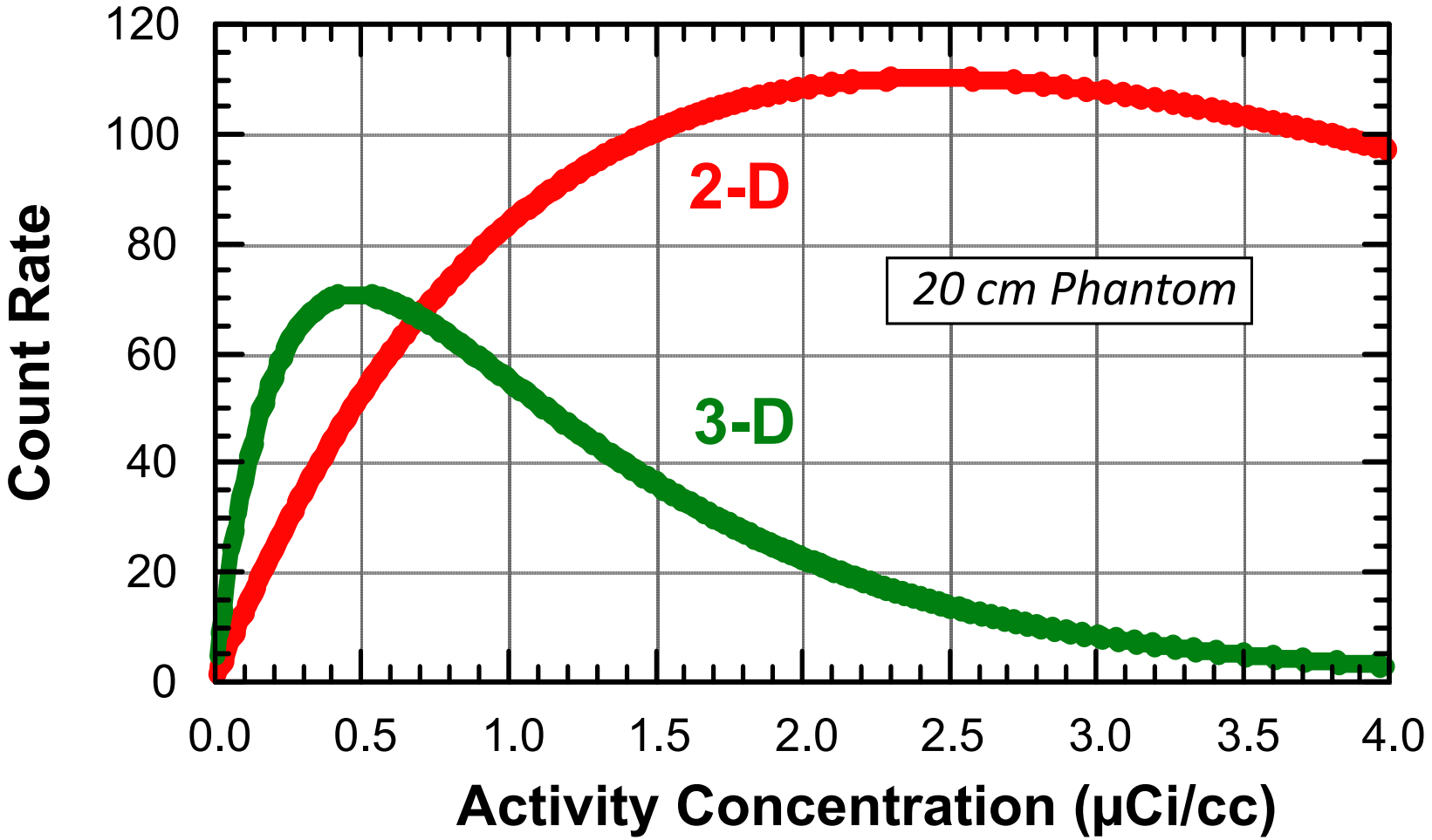

- *At Small Activities, 3-D has Higher NECR*
- *Peak NECR in 2-D > Peak NECR in 3-D*
- *Very Sensitive to Scanner, Definitions, & Phantom Size!*

Coincidene Measurement in PET Image Acquisation

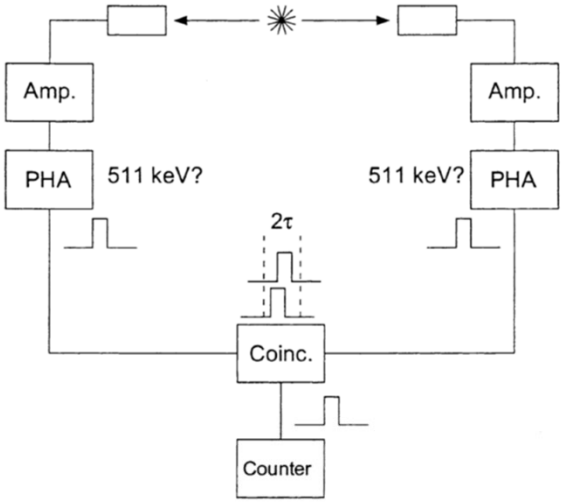

FIGURE 20. Diagram of a basic coincidence circuit. The two scintillation detectors with are connected to individual amplifiers (Amp) and pulse height analyzers (PHA). When a photon interacts in either of the detectors, the signals are amplified and analyzed to determine if the energy is above a certain threshold. If the energy criterion is satisfied, a logic pulse is generated by the PHA. These pulses are fed into a coincidence module (Coinc), which determines if there is an overlap of two pulses from the individual channels. An overlap occurs if both pulses occur within a time period of 2τ (e.g., they differ from each other in time by $\leq \tau$), where τ is the width of the pulse. If this is the case, a coincidence has been detected and the coincidence circuit generates a logic pulse that is fed into a counter for registration of the event. In a PET imaging system, the memory location corresponding to the two detectors in which the interaction occurred is incremented by one.

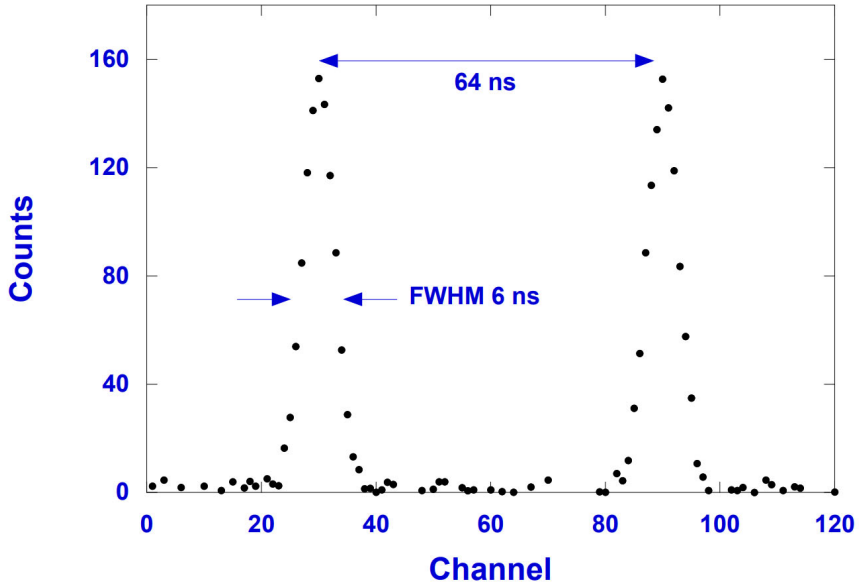

Timing spectrum showing the PHA trigger time variation for a pair of BGO detectors in coincidence. The two peaks corresponds to two separate measurements where an additional delay of 64 ns of the stop pulse for channel-to-time calibration.

Coincidene Measurement in PET Image Acquisation

For a uniform distribution of activity, a formula for the random count rate per ring has been established:

$$C_R = \tau f C_s^2 \qquad \left(\frac{\text{counts}}{\text{sec}} \cdot \frac{\mu\text{Ci}}{\text{cm}^3}\right) \tag{8-2}$$

where C_s is the single count rate for the entire ring, τ is the coincidence resolving time, and f represents the coincidence fraction of a given phantom (which is the ratio of the number of detectors in a fan to the total number of detectors in the ring, each of which is in coincidence with any one of the detectors on the opposite side). The value of f for a ring system is given by

$$f = \left(\frac{2}{\pi}\right)\sin^{-1}\left(\frac{d}{D}\right) \tag{8-3}$$

Fundations of Medical Imaging, Z. H. Cho.

Time-of-Flight PET

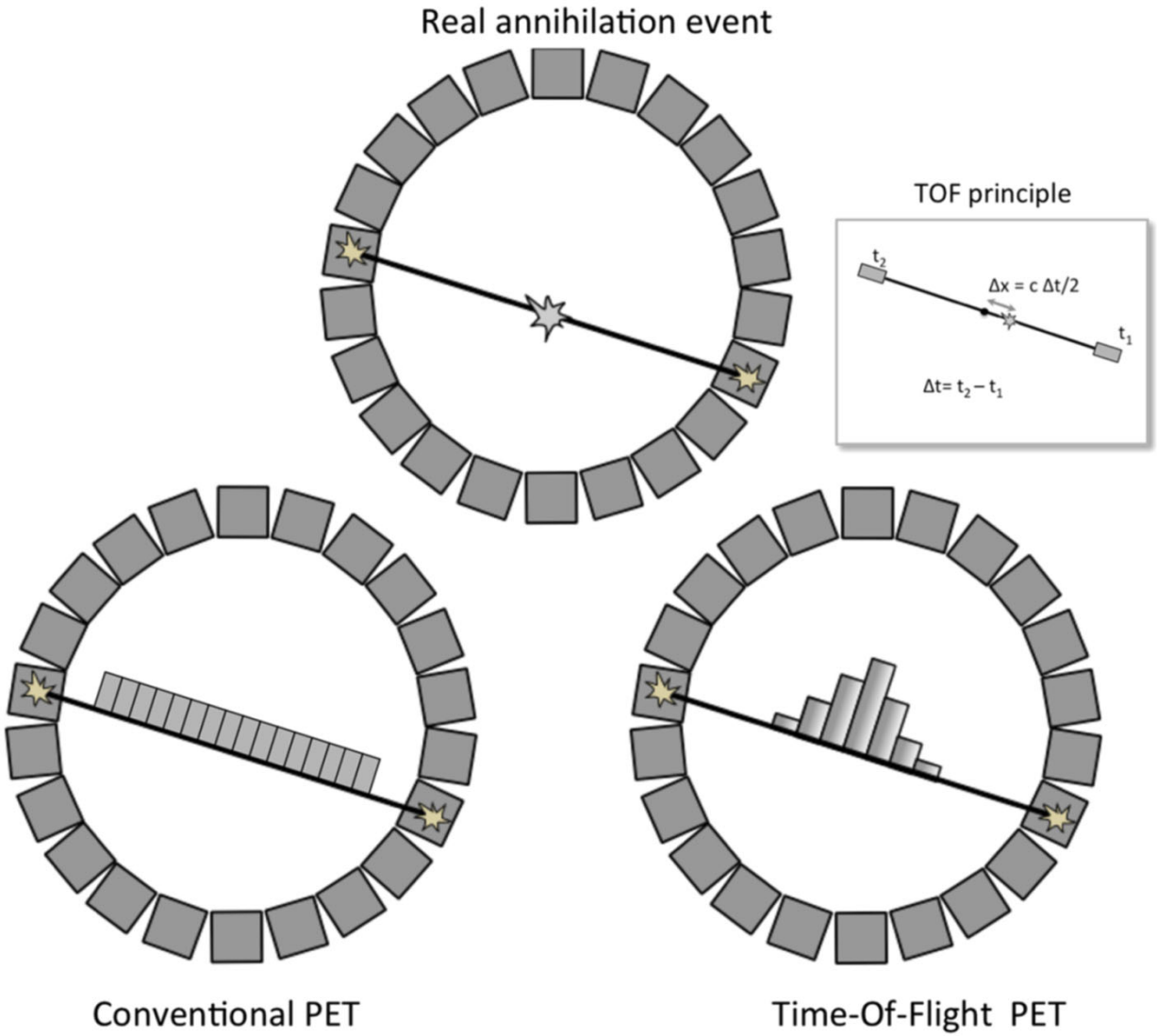

Fig. 1 Compared to conventional PET, the estimated time-of-flight difference (Δt) between the arrival times of photons on both detectors in TOF-PET allows localization (with a certain probability) of the point of annihilation on the line of response. In TOF-PET, the distance to the origin of scanner (Δx) is proportional to the TOF difference via the relation: Δt: $\Delta x = \frac{c\Delta t}{2}$, where c is the speed of light. t_1 is the arrival time on the first detector, and t_2 is the arrival time on the second detector

Eur J Nucl Med Mol Imaging (2011) 38:1147–1157
DOI 10.1007/s00259-010-1711-y

REVIEW ARTICLE

Focus on time-of-flight PET: the benefits of improved time resolution

Maurizio Conti

Table 1 Time resolution, spatial uncertainty and estimated TOF gain for a 40-cm effective diameter patient

Time resolution (ns)	Δx (cm)	TOF NEC gain	TOF SNR gain
0.1	1.5	26.7	5.2
0.3	4.5	8.9	3.0
0.6	9.0	4.4	2.1
1.2	18.0	2.2	1.5
2.7	40.0	1.0	1.0

In particular, the SNR in a TOF image improves with decreasing time resolution Δt (or the corresponding spatial uncertainty Δx) and it is larger for larger patients (being related to the effective diameter D). The TOF SNR is proportional to the non-TOF SNR, through the following relationship [1, 2, 4, 14–20]:

$$SNR_{TOF} = \sqrt{\frac{D}{\Delta x}} \cdot SNR_{non-TOF} \qquad (2)$$

Clinical Benefit of Time-of-Flight PET

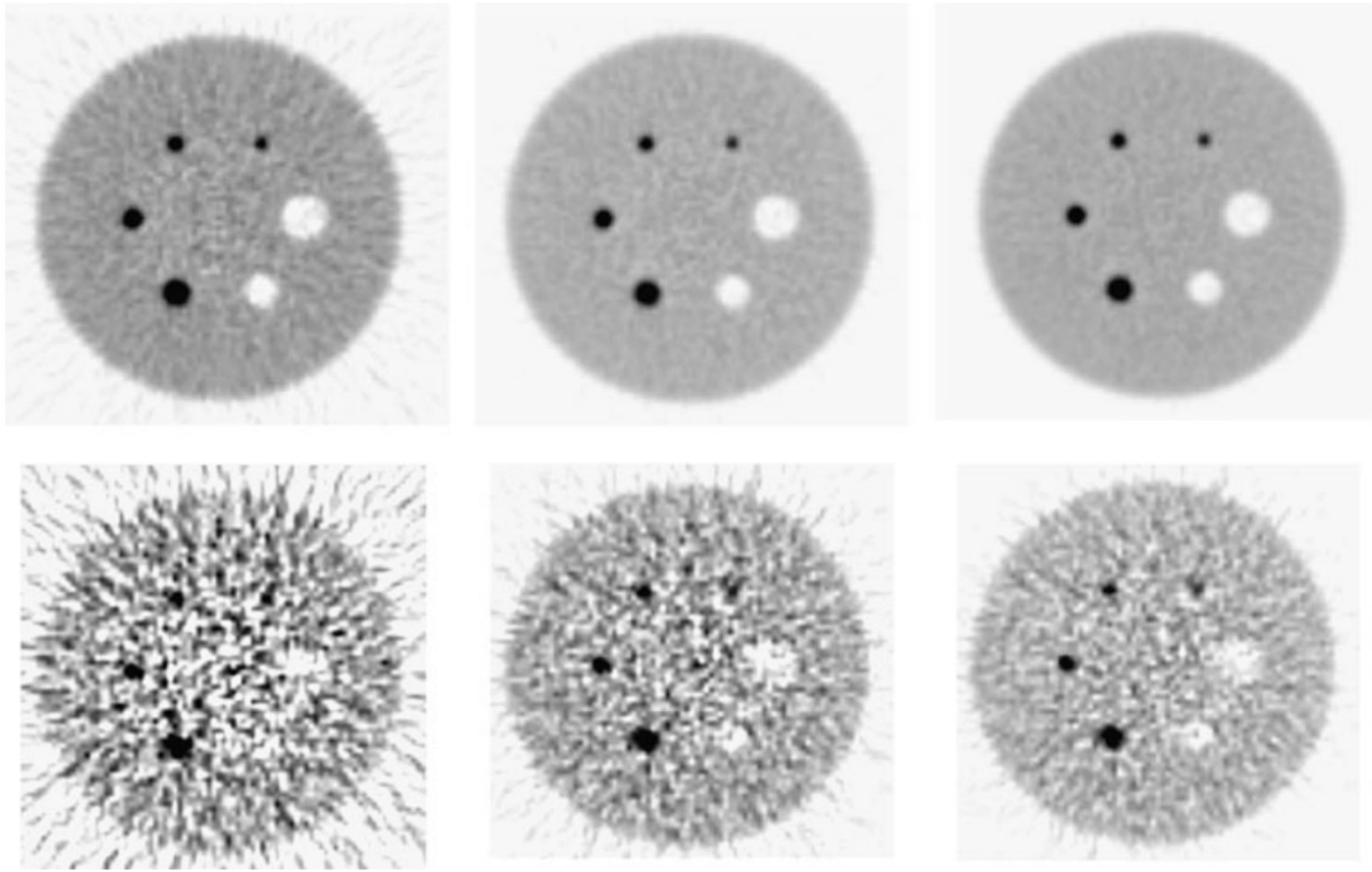

Fig. 7 Monte Carlo simulation of a uniform cylinder with spheres of diameter 10, 13, 17 and 22 mm at a contrast ration of 4:1 and two spheres of diameter 28 and 37 mm filled with water with no activity: high statistics, 356×10^6 counts in the total volume (*top*); low statistics, 10×10^6 counts (*bottom*). Filtered back-projection was used for non-TOF reconstruction (*left*), for TOF reconstruction with 600 ps time resolution (*centre*), and for TOF reconstruction with 300 ps time resolution (*right*)

Clinical Benefit of Time-of-Flight PET

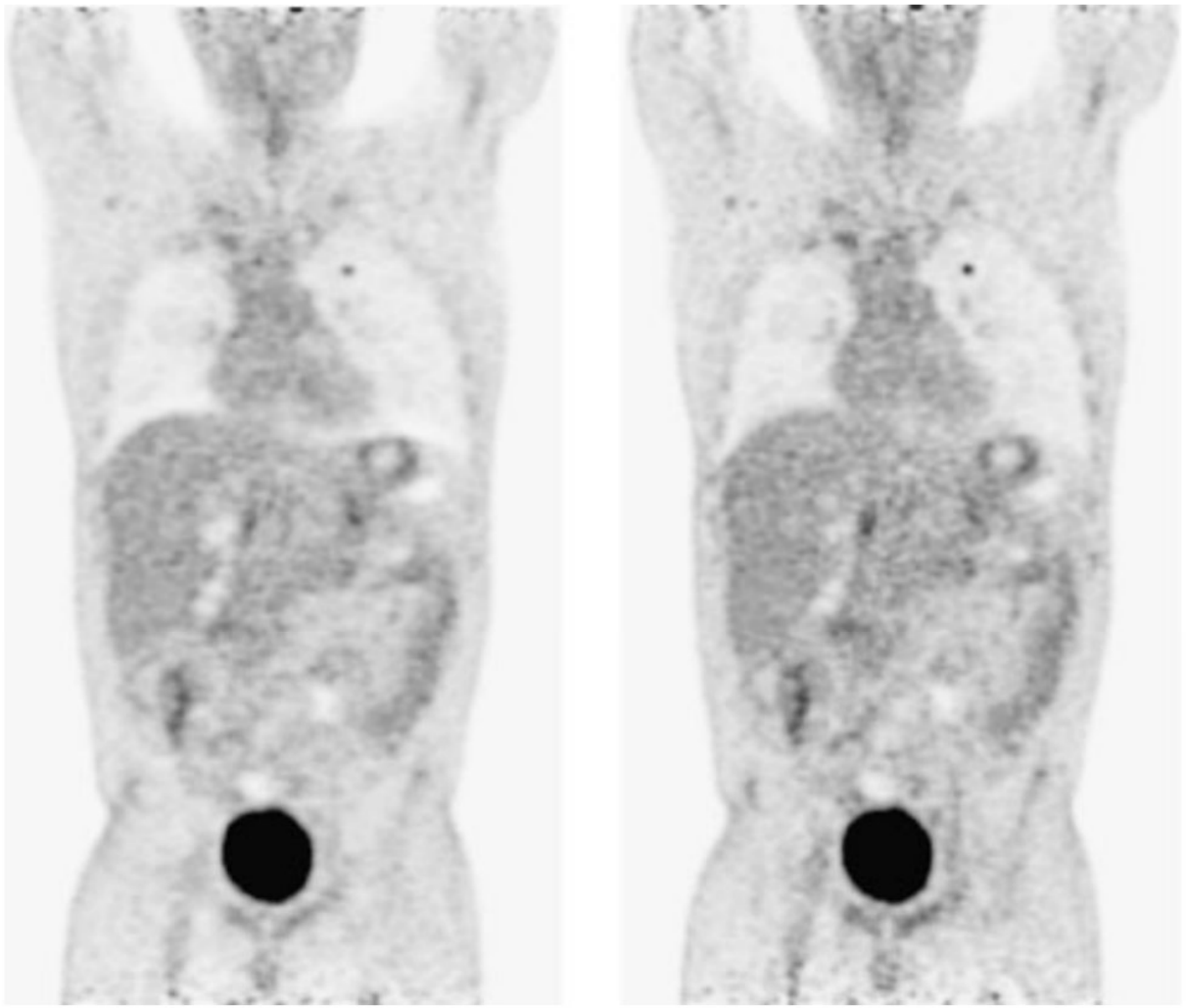

Fig. 1 Coronal images reconstructed from a non-TOF scan (*left*) and a TOF scan (*right*) in a patient with lung cancer. The acquisition time was 3 min per bed position for both images. At the same number of counts, the image quality is better with the TOF reconstruction

Clinical Benefit of Time-of-Flight PET

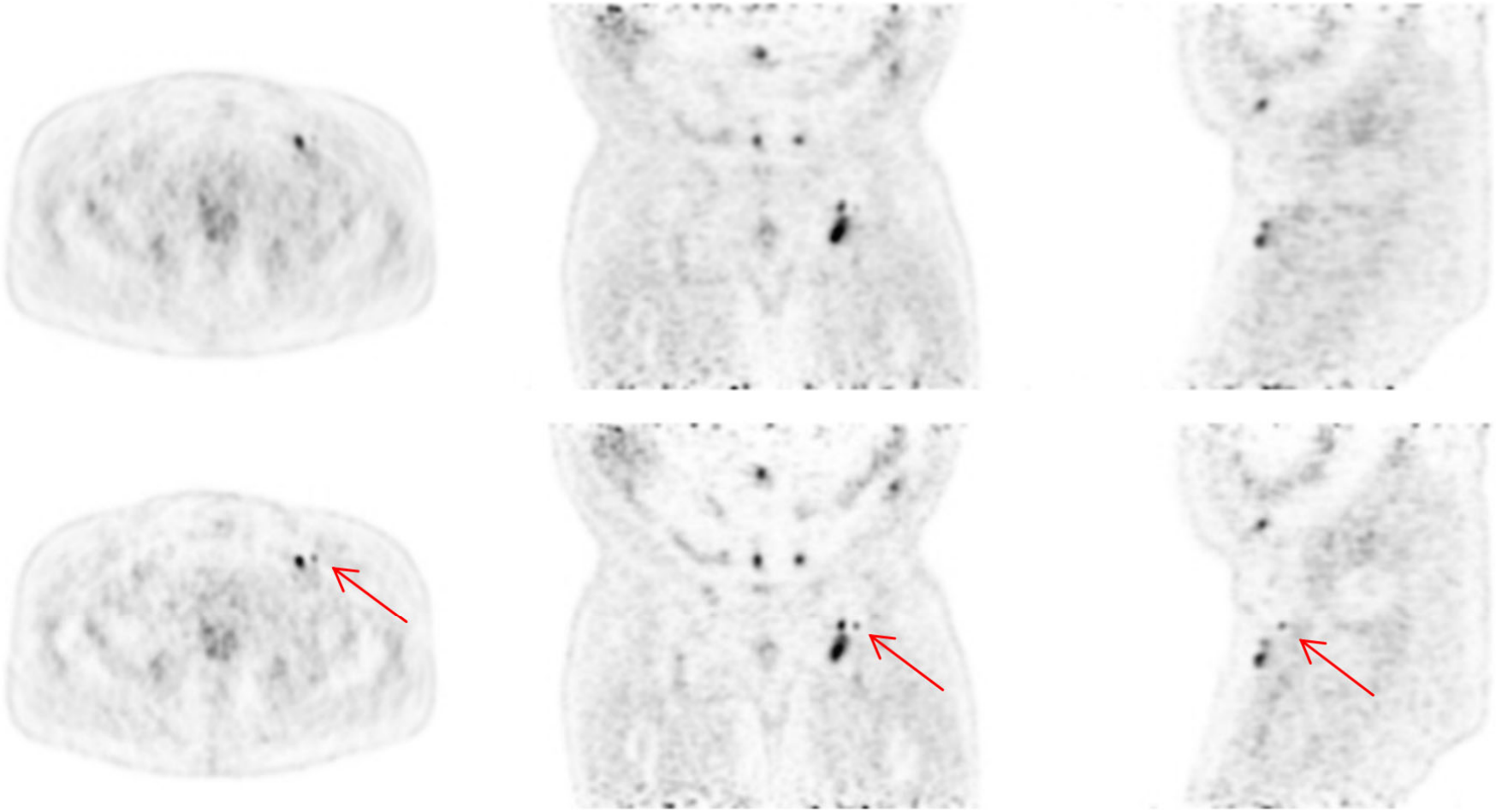

Fig. 3 Transaxial, coronal and sagittal images in a patient with nodules in the pelvic region showing FDG uptake (*top* non-TOF image, *bottom* TOF image). *Arrows* uptake focus not visible in the non-TOF images

How to incorporate time-of-flight (TOF) information in maximum-likelihood (ML) image reconstruction?

Statistical Description of the Projection Data

The probability of a given projection data $\mathbf{g}=(g_1, g_2, g_3, \ldots, g_M)$ *is*

$$p(\mathbf{g}) = \prod_{m=1}^{M} p(g_m) = \prod_{m=1}^{M} \frac{\bar{g}_m^{\,g_m}}{g_m!} e^{-\bar{g}_m}$$

Measured no. of counts on detector pixel m.

where $\bar{g}_m$ is the expected value for the number of counts on detector pixel #m

$$\bar{g}_m = \sum_{n=1}^{N} f_n p_{nm}$$

In the context of emission tomography, p_{nm} *is the probability of a gamma ray generated at a source pixel n is detected by detector element m.*

Remember that

$$\begin{pmatrix} \bar{g}_1 \\ \bar{g}_2 \\ \bar{g}_3 \\ \vdots \\ \bar{g}_M \end{pmatrix} = \begin{pmatrix} p_{11} & p_{12} & p_{13} & \cdots & p_{1N} \\ p_{21} & p_{22} & p_{23} & \cdots & p_{2N} \\ p_{31} & p_{32} & p_{33} & \cdots & p_{3N} \\ \vdots & \vdots & \vdots & \ddots & \vdots \\ p_{M1} & p_{M2} & p_{M3} & \cdots & p_{MN} \end{pmatrix} \begin{pmatrix} f_1 \\ f_2 \\ f_3 \\ \vdots \\ f_N \end{pmatrix}$$

The Maximum Likelihood Reconstruction

*Recall that the **likelihood function,** L(**f**,**g**), of a possible source function **f** is*

$$L(\boldsymbol{f},\boldsymbol{g}) = p(\boldsymbol{g} \mid \boldsymbol{f})$$

So that the maximum likelihood solution (the image that maximizing the likelihood function) can be found as

$$\hat{\boldsymbol{f}}_{\boldsymbol{ML}} = \underset{\boldsymbol{f}}{\operatorname{argmax}}\, L(\boldsymbol{f},\boldsymbol{g})$$

or equivalently

$$\hat{\boldsymbol{f}}_{\boldsymbol{ML}} = \arg\max_{\boldsymbol{f}} \log\left[L(\boldsymbol{f},\boldsymbol{g})\right] \equiv \underset{\boldsymbol{f}}{\operatorname{argmax}}\, l(\boldsymbol{f},\boldsymbol{g})$$

where $l(\boldsymbol{f},\boldsymbol{g})$ is the log-likelihood function

$$l(\boldsymbol{f},\boldsymbol{g}) = \log\left[L(\boldsymbol{f},\boldsymbol{g})\right]$$

Methods to Estimate the Underlying Image

The Maximum Likelihood Expectation Maximization (MLEM) Algorithm

$$f_n^{(new)} = \frac{f_n^{(old)}}{\sum_{m=1}^{M} p_{nm}} \sum_{m=1}^{M} \frac{g_m}{\sum_{n'=1}^{N} p_{n'm} f_{n'}^{(old)}} p_{nm}, \quad n = 1,2,...,N$$